THESIS FOR THE DEGREE OF DOCTOR OF PHILOSOPHY

Spin Transport in Two-Dimensional Material Heterostructures

André Dankert

Department of Microtechnology and Nanoscience
Quantum Device Physics Laboratory
Chalmers University of Technology
Göteborg, Sweden 2015

Spin Transport in Two-Dimensional Material Heterostructures

André Dankert

Göteborg, January 2015

ISBN 978-91-7597-131-5

Doktoravhandlingar vid Chalmers Tekniska Högskola
Ny serie nr 3812
ISSN 0346-718X

ISSN 1652-0769
Technical Report MC2-298

Quantum Device Physics Laboratory
Department of Microtechnology and Nanoscience - MC2
Chalmers University of Technology
SE-412 96 Göteborg, Sweden
Telephone +46 (0)31-772 1000

Cover: Coloured scanning electron micrograph of a heterostructure device made of molybdenum disulphide and graphene, symbolizing the main effects studied in this thesis. Circles from left to right: 1. Spin injection from a ferromagnet through hexagonal boron nitride into graphene; 2. Long distant spin transport in graphene; 3. High spin-orbit coupling in two-dimensional semiconductors; 4. Spin-momentum locking in topological insulators.

Printed by Chalmers Reproservice
Göteborg, Sweden 2015

Spin Transport in Two-Dimensional Material Heterostructures

André Dankert

Quantum Device Physics Laboratory
Department of Microtechnology and Nanoscience
Chalmers University of Technology

Abstract

Spintronics is considered as an alternative for information processing beyond the charge based technology. The spintronic device performance depend on the spin relaxation mechanisms in the channel material. Si and graphene are interesting for their long spin coherence lengths and ideal for spin transport channels. Additionally, the interest in newly discovered *two-dimensional semiconductors* (2D SC), *topological insulators* (TI) and *hexagonal boron nitride* (h-BN) increases due to their strong spin-orbit coupling, existence of spin polarized surface states and insulating band structure, respectively. Despite the recent advances in spintronics, most of these new materials are not explored and the spin physics is not fully understood yet.

In this thesis, we create large spin polarizations up to 34% in the Si bulk using ozone oxidized SiO_2 as an ideal tunnel barrier and study the influence of its *Schottky barrier* (SB) on the spin injection at room temperature. In graphene, we investigate the effect of *ferromagnetic* (FM) tunnel contacts and channel length dependence on the spin signal achieving spin transports over distances of 16 μm and spin lifetimes of 1.2 ns in CVD graphene. Using the 2D insulator h-BN as an alternative barrier material in magnetic tunnel junctions and on Si reveals a good tunnel spin polarization, whereas h-BN on graphene significantly increases the spin lifetimes and results in spin polarizations up to 65%. For the 2D SCs MoS_2 and black phosphorous we demonstrate a significant reduction of their interface SB by using FM tunnel contacts, which circumvent the conductivity mismatch problem required for magnetoresistance measurements. Finally, we measure the spin-momentum locking in the surface states of the topological insulator Bi_2Se_3 using FM tunnel contacts up to room temperature.

These excellent spintronic properties of the individual materials and their heterostructures promise novel devices with custom-designed spin properties.

Keywords: Spintronic, 2D materials, Transistor, Graphene, Silicon, Topological insulator, MoS_2, h-BN, Black phosphorous, Schottky barrier, Spin polarized tunnelling

Publications

This thesis is based on the work obtained for the following papers

I **Efficient Spin Injection into Silicon and the Role of the Schottky Barrier**
André Dankert, Ravi S. Dulal, Saroj P. Dash
Sci. Rep. 3, 3196 (2013)

II **Spin transport and precession in graphene measured by non-local and three-terminal methods**
André Dankert, M. Venkata Kamalakar, Johan Bergsten, Saroj P. Dash
Appl. Phys. Lett. 104, 192403 (2014)

III **Enhanced Tunnel Spin Injection into Graphene using Chemical Vapor Deposited Hexagonal Boron Nitride**
M. Venkata Kamalakar, André Dankert, Johan K. Bergsten, Tommy Ive, Saroj P. Dash
Sci. Rep. 4, 6146 (2014)

IV **Spin Filtering in Ferromagnet/Hexagonal Boron Nitride/Graphene Heterostructures at Room temperature**
M. Venkata Kamalakar, André Dankert, Paul J. Kelly, Saroj P. Dash
Submitted

V **Tunnelling Magnetoresistance with Large Area Atomically Thin Hexagonal Boron Nitride Barriers at Room Temperature**
André Dankert, M. Venkata Kamalakar, A. Wajid, R. S. Patel, Saroj P. Dash
Nano Res. DOI: 10.1007/s12274-014-0627-4 (2014)

VI **Long Distance Spin Communication in CVD Graphene on SiO_2/Si Substrate at Room Temperature**
M. Venkata Kamalakar, Christiaan Groenveld, André Dankert, Saroj P. Dash
Submitted

VII **High Performance Molybdenum Disulphide Field Effect Transistors with Spin Tunnel Contacts**

André Dankert, Lennart Langouche, M. Venkata Kamalakar, Saroj P. Dash
ACS Nano 8, 476 (2014)

VIII Low Schottky Barrier Black Phosphorus Field-Effect Devices with Ferromagnetic Tunnel Contacts
M. Venkata Kamalakar, B. N. Madhushankar, André Dankert, Saroj P. Dash
Small DOI: 10.1002/smll.201402900 (2015)

IX Room Temperature Electrical Detection of Spin Polarized Currents in Topological Insulators
André Dankert, Johannes Geurs, M. Venkata Kamalakar, Saroj P. Dash
Submitted

Other publications that are outside the scope of this thesis

- **Thermal Creation of Electron Spin Polarization in n-Type Silicon**
  André Dankert, Saroj P. Dash
  Appl. Phys. Lett. 103, 242405 (2013)

- **Electric field effects on spin accumulation in Nb-doped SrTiO3 using tunable spin injection contacts at room temperature**
  A. M. Kamerbeek, Erik K. de Vries, André Dankert, Saroj P. Dash, Bart J. van Wees, Tamalika Banerjee
  Appl. Phys. Lett. 212106, 98–102 (2014)

"If you can't explain it simply,

you don't understand it well enough."

——Albert Einstein ‖ Richard Feynman

Contents

List of Figures

Abbreviations and Symbols

Abbreviations

1D	One-dimensional
2D	Two-dimensional
3D	Three-dimensional
3T	Three-terminal
ARPES	Angular resolved photo-emission spectroscopy
BHF	Buffered hydrofluoric acid
BP	Black phosphorous
CNP	Charge neutrality point
CVD	Chemical vapour deposition
DI	Deionized
DOS	Density of states
DP	D'yakonov-Perel
EBL	Electron beam lithography
EY	Elliott-Yafet
FET	Field effect transistor
FM	Ferromagnet
GMR	Giant Magneto Resistance
h-BN	Hexagonal boron nitride
HF	Hyperfine
HLN	Hikami-Larkin-Nagaoka
HR	High resistance
IPA	Isopropyl alcohol
IV	Current-voltage characteristic
LED	Light emitting diode
LR	Low resistance
MBE	Molecular beam epitaxy
MR	Magnetoresistance
MTJ	Magnetic tunnel junction
NL	Non-local
NM	Non-magnetic material
PL	Photolithography
PR	Photoresist
SBH	Schottky barrier height
SB	Schottky barrier
sFET	Spin field effect transistor
SML	Spin-momentum locking
SO	Spin-orbit
TI	Topological insulator
TMDC	Transition metal dichalcogenide
TMR	Tunnel magnetoresistance
TR	Transparent resistance
TSP	Tunnel spin polarization
TSS	Topological surface states
UCF	Universal conductance fluctuation
UV	Ultraviolet
WAL	Weak anti-localization
WL	Weak localization
ZBR	Zero bias resistance

Fundamental constants

c	Speed of light: $c = 2.99792458 \cdot 10^8\ {}^{m}/_{\mathrm{s}}$
e	Electron charge: $e = 1.60217657 \cdot 10^{-19}\ \mathrm{As}$
h	Planck constant: $h = 6.62606957 \cdot 10^{-34}\ \mathrm{m^2kg/s}$
$\hbar$	Reduced Planck constant: ${}^{h}/_{2\pi} = 1.05457 \cdot 10^{-34}\ \mathrm{m^2kg/s}$
k_B	Boltzmann constant: $k_\mathrm{B} = 1.3806488 \cdot 10^{-23}\ {}^{m^2kg}/_{\mathrm{s}^2\mathrm{K}}$
μ_B	Bohr magneton: $\mu_\mathrm{B} = 9.27400968 \cdot 10^{-24}\ {}^{m^2kg}/_{\mathrm{s}^2\mathrm{T}}$

Mathematical Symbols

A	Contact area
A^*	Richardson constant
$\vec{B}$	Magnetic field
$B_\parallel$	In-plane magnetic field
$B_\perp$	Perpendicular magnetic field
B_c	Coercive field

β	Bulk spin assymetrie coefficient
D	Diffusion constant
$D_{\uparrow\downarrow}$	Spin dependent diffusion constant
d_{SiO2}	SiO_2 barrier thickness
$\vec{E}$	Electric field
η	Surface/bulk contribution
f	Ideality factor
g	g-factor
γ	Interface spin polarization
γ_d	Detector spin polarization
γ_{FM}	Ferromagnet tunnel polarization
γ_i	Injector spin polarization
γ_S	Surface spin polarization
G_{ap}	Conductance for antiparallel magnetization orientation
G_p	Conductance for parallel magnetization orientation
I_{on}/I_{off}	Transistor on-off ratio
j	Charge current density
$j_{\uparrow\downarrow}$	Spin dependent current density
L	Channel length
λ_{FM}	Spin diffusion length in ferromagnet
λ_{NM}	Spin diffusion length in nonmagnetic material
λ	Spin diffusion length
$l_{e\uparrow\downarrow}$	Spin dependent mean free path
l_{mf}	Mean free path
l_{mf}	Mean free length
l_φ	Phase coherence length
I	Total tunnel current
MR	Magnetoresistance
MR_{NL}	Non-local magnetoresistance
μ	Equilibrium chemical potential
μ_0	Interfacial spin splitting
$\Delta\mu$	Interface potential splitting
μ_{eff}	Effective field effect mobility
μ_{FM}	Ferromagnet potential
μ_{NM}	Non-magnetic material potential
N	Available states at the Fermi level
n	Excess particle density
η	Surface current contribution
$N_{\uparrow\downarrow}$	Spin-dependent available states
$n_{\uparrow\downarrow}$	Spin densities
ω_{L}	Larmor frequenzy
P	Spin polarization
$\wp_D$	Spin diffusion probability
$\wp_t$	Spin dephasing probability
Φ_{sb}	Schottky barrier height
ψ	Digamma function
R_{ap}	Resistance for antiparallel magnetization orientation
R_p	Resistance for parallel magnetization orientation
R_c	Contact resistance
R_{FM}	Ferromagnet resistance
R_I	Interface resistance
$R^I_{\uparrow\downarrow}$	Spin dependent R_I
R_{NM}	Non-magnetic resistance
$R_\square$	Non-magnetic square resistance
R_{TB}	Tunnel barrier resistance
$R^{TB}_{\uparrow\downarrow}$	Spin dependent barrier resistance
$R^{TB}_{\uparrow\downarrow}$	Spin dependent tunnel resistance
σ	Conductivity
σ_{FM}	Conductivity of FM
σ_{NM}	Conductivity of NM
$\sigma_{\uparrow\downarrow}$	Spin dependent conductivity
T	Temperature
τ	Spin lifetime
$\tau_{\downarrow\uparrow}$	Spin flip time from down to up spin
$\tau_{\uparrow\downarrow}$	Spin flip time from up to down spin
t_{NM}	Thickness of nonmagnetic material layer
t_{ox}	Oxidation time
$\vec{v}$	Relativistic velocity
v_{F}	Fermi velocity
$v_{F\uparrow\downarrow}$	Spin dependent Fermi velocity
V_{NL}	Non-local voltage
W	Channel width

Preface

This thesis collects the results of several projects, which I was working on during my time as a Ph.D. student. The field of spintronics is complex in itself, and so is the world of two-dimensional materials. To join both fields and still provide a good overview for the reader, the thesis is separated in three parts.

The background chapter should give a comprehensive overview of the theory of spintronics and goes even beyond the basic transport measurement with direct-current. Furthermore, it provides an extensive but still compact review of many two-dimensional materials. The main chapters present our experimental results and discusses its motivation and practical relevance. Finally, I added all specifications of the techniques, which I adopted or developed for the device fabrication.

An interested reader will find each part equally enjoyable, yet is the intention of the text to be simple and understandable even for newcomers to the topic. Colleagues and researchers, including myself, can use it as a handy review of the currently most commonly used two-dimensional materials, as well as a collection of the required formulas and a tested process database.

Acknowledgements

My foremost gratitude goes to Professor Saroj P. Dash. Without his knowledge, ideas and insight this thesis would not have been possible. Especially his open, calm and friendly character is inspiring and made every challenge appear as an opportunity to take.

My gratitude also goes to Venkat, who was the third musketeer in our group and a major contribution to my work for the last 2 years.

Over the years, I had the honour to work with many master students, which also contributed significantly to my work. My thanks go to Ravi, Johan, Lennart, Johannes, Madhu and Chris.

I also want to acknowledge the guidance by Sergey Kubatkin, Per Delsing and Per Lundgren, as well as the feedback and useful discussions of all professors at QDP and AQP during my Ph.D. time. Furthermore, I would like to thank the groups of Timur Shegai, Tommy Ive and Tamalika Banerjee for the opportunities for active and interesting collaborations!

I should also not forget the support by the clean room staff, who were always open for new ideas and provided helpful discussions: *Extra stort tack till* Henrik, Johan, Mats and Bengt!

Also the help of Lars and Staffan in the work shop, and the administrative support by Susannah, Deborah, Marie and Ann-Marie will never be forgotten. *Tusen tack!*

Thank you Anton for letting me bug you with all the small questions about everything around the thesis and Ian for our theoretical discussions for my chapters - it was not forgotten!

I should also not forget the people, who make QDP the lively and colourful place, where colleagues are hard to distinct from friends. My thanks go especially to Michaël and Niclas, who were always open for a coffee break or a discussion, in English or Swedish! I would also like to thank Riccardo, Philip, Marco, Pier Paolo, Astghik, Samuel, Sumedh, Tom, Yevgeniy, Ida-Maria, Maria, Luca, Mathieu, Sebastian and all past and present members of QDP and AQP for the joyful and inspiring conversation and the help in and outside the clean room!

A special thanks goes to my lovely fiancée Sophie! I know it is sometimes difficult to be with me, but her seemingly endless patience and support was of tremendous help during the last months of writing! *Merci beaucoup mon amour!*

I also want to thank my friends and family for their support. *Danke für eure Unterstützung und euer Verständnis, ohne euch wäre das nie möglich gewesen!*

Finally, I would like to acknowledge the funding of my research through the AoA Nano Area of Advance program at Chalmers University of Technology, the Marie Curie Career Integration Grant and the Swedish Research Council (VR) Young Researchers Grant.

Introduction

Conventional information technology is charge based; the information storage and processing is performed by controlling the flow of charge carriers, such as electrons and holes. Modern fabrication techniques allow to manufacture such devices with decreasing size and increasing density every year. This reduction in size allows for higher performances, but creates a physical size limitation. Smaller structures exhibit dominating quantum effects, such as quantum mechanical tunnelling, which can yield to gate tunnel leakage currents and therefore performance loss. Additionally, the higher device density yields a higher current density in the chips, which consequently results in a greater heat dissipation, hence energy wastage. These problems and limitations are difficult to solve with traditional technologies.

Spintronics offers a different approach, allowing to reduce the energy consumption and possibly employing quantum effects for storage and processing of information in a single device [1, 2]. A spin is an additional quantum-mechanical degree of freedom carried by elementary particles, such as electrons, holes and nuclei. It is often compared to the classical angular momentum of an object. Spintronics redefines the basic building blocks for logic operations by using the spin of the charge carriers. In conventional devices high and low carrier concentrations define the logical ON (1) and OFF (0) state, respectively. Spintronic logic is based on spin polarization and spin current direction, for example spin-up $\uparrow$ (ON) and spin-down $\downarrow$ (OFF). This is advantageous, since the quantity of energy required to change a spin state is orders of magnitude smaller than the one to rearrange charge carriers [3].

The concept of a spin dependent transport in *ferromagnetic* (FM) metals, suggesting possible applications, was first described by Mott in 1936 [4, 5]. This could be employed in devices based on the *giant magnetoresistance* (GMR) [6] and *tunnel magnetoresistance* (TMR) effect [7], which was awarded with a Nobel price in 2007. The magnetoresistance effects enabled to detect different magnetic states as high or low voltage, depending on the

magnetization direction. This is used to read and write non-volatile information on magnetic discs, which was a foundation for the information storage development. Mott's prediction of a spin dependent transport further lead to the idea to create an non-equilibrium spin distribution in *non-magnetic materials* (NM), first proposed by Aronov in 1976 [8]. A decade later, Johnson and Silsbee demonstrated the first spin injection and transport in aluminium [9]. This was a necessary step on the way to develop spin-based logic devices, since dynamically created spin accumulations are easier to manipulate. Nevertheless, since the spin diffusion length is short and the charge carrier concentration is fixed, metals are mere passive spintronic elements. *Semiconductors* (SC) have a variable carrier concentration by doping and gating, exhibit a long spin coherence, and are technologically well integrated, which makes them more attractive for spintronic studies.

The creation and detection of spin accumulations in SC materials has been shown by electrical and optical techniques. In the latter, the angular momentum transfer can be achieved by irradiating circular polarized light which excites highly spin polarized electrons in the conduction band [10]. By employing the reverse effect, the spin accumulation can be optically detected through an analysis of the degree of polarization of the emission by electro-luminescence. Recombinations of either up- or down spin result in circular polarized light with different helicity, which can be measured [11]. Optical techniques are excellent to create and study spin accumulations, their distribution and spin lifetimes in materials, but they are not convenient for electronic applications. Electrical spin injection and detection is much more suited for implementation not only into current technology, but also for further development towards all-spin logic gates, where computing, information transfer and storage are completely spin based [12].

There are several methods to create spin accumulations electrically. Commonly, FM contacts are used to inject spin polarized currents into NM. Ferromagnets have a large exchange interaction, which yields to an alignment of the outer electrons resulting in different *density of states* (DOS) close to the Fermi level. Applying a charge current translates this spin polarization in the FM into a spin polarized current, which can be used to create a non-equilibrium spin accumulation in NM, which can be transported, detected, and manipulated.

The first proposal for a *spin field effect transistor* (sFET) was made by Datta and Das in 1990 [13]. Since then, spin accumulations and their transport were studied in metals [14, 15] and SC [16–20]. The host material plays a crucial role for the intended application of the spintronic device. On

one hand, materials with a low *spin-orbit* (SO) coupling, such as silicon and graphene, exhibit less spin-scattering events promising a long spin lifetime and diffusion length [21]. This is attractive for spin logic arrays, where spin devices communicate by spin currents over longer distances. On the other hand, a large SO interaction, like it is found in indium arsenide and gallium arsenide, allows to employ the Rashba effect, which enables the dephasing of the spins by an electric gate field [13]. Such manipulation is required in spin logic devices themselves, such as sFETs.

Functional spin circuits require an efficient creation, transport and detection of spin currents, as well as the possibility to manipulate the spins in a transistor-like manner. In recent years, Si and graphene have gained a huge interest in spintronic research due to the expected long spin coherence time [18, 22, 23]. While Si is the most popular and industrial compatible material, graphene is interesting for its high mobility and electronic control of charge carriers and their concentration. In addition to its electrical properties, the *two-dimensional* (2D) nature of graphene allows for implementations in flexible and transparent technologies which can replace currently used rare materials and opens up new fabrication techniques [24]. This possibility sparked the interest in the fast growing family of other 2D materials and their heterostructures opening up new ways for future electronic as well as spintronic devices with a wide range of properties [22]. Graphene has a low SO coupling, which makes it interesting for long distance spin transport and communication for spin logic devices. In contrast, 2D SC, such as *transition metal dichalcogenides* (TMDC) and *black phosphorous* (BP), posses a large SO and nuclear hyperfine interaction and can be used for sFET. Similarly, *topological insulators* (TI) posses a SC bulk and metallic surface states with spin-momentum locking, which can create dissipationless spin polarized currents. An even larger band gap can be found in *hexagonal boron nitride* (h-BN), which can be used as a 2D insulator and as tunnel barrier [25].

So far, most of these materials are largely unexplored for spintronic applications and their spin functionalities are not clearly understood. Injected spins in Si and graphene exhibit a significantly shorter spin lifetime and lower spin polarization than theoretically expected, whereby it is unclear if it is an intrinsic, channel or contact induced effect [26, 27]. Even though the electrical spin injection technique by FMs is robust, the tunnel interfaces have to be optimized for different materials to avoid roughness, leakage and stray fields [28]. These effects could be avoided for example by replacing the traditional metal oxide barriers by atomically thin and inert h-BN,

which was proposed to exhibit a high tunnel spin polarization [29]. Next to a large spin polarization, the ability to manipulate the spins is a crucial requirement for possible logic applications. Such spin manipulation could be performed by 2D SC due to their large intrinsic SO coupling and high carrier mobility, which is still experimentally challenging to achieve [30]. Furthermore, the spin polarized currents in the surface states of TIs could be accessed as an ideal spin generator, but so far their electrical detection was limited to measurements at low temperatures [31], which reduces its potential for applications.

In this thesis we focus on the investigation of the basic spintronic functionalities in heterostructures made with 2D materials. Chapter 1 introduces the theoretical description of spin injection, transport, and detection processes, as well as other techniques employed to analyse the discussed results. The chapter concludes with an overview of the recent achievements and challenges in spintronics for the different materials. In Chapter 2 we demonstrate a large spin polarization at room temperature in both n- and p-type Si using a high quality SiO_2 tunnel barrier. Further investigations revealed interface related effects depending on the Schottky barrier thickness. To overcome barrier related effects we studied h-BN in magnetic tunnel junctions and as barrier in FM tunnel contacts on Si. Similarly, we demonstrate contact induced spin relaxation effects in graphene, but also a channel length dependence on the spin parameters while achieving long distance spin transport in CVD graphene (Chapter 3). Subsequently, using h-BN on exfoliated graphene we produce a 2D tunnel barrier with significantly improved spin lifetimes and spin polarizations. Chapter 4 approaches 2D SCs for sFET applications. We optimize the transistor properties by improving the contact resistance and put the results into perspective with the spin diffusion theory. Subsequently, we create a short transistor channel by combining the 2D SC with the excellent spin transport properties of graphene in a vertical device and study these heterostructures. Finally, we investigate the possibility of creating spin polarized currents by accessing the spin-momentum locking of the surface states of the TI Bi_2Se_3 (Chapter 5). A spin polarization can be reproducibly detected up to room temperature using sensitive FM tunnel contacts. These results represent important advances in the field of spintronics increasing the understanding and possibilities for the creation, transport and manipulation of spins in 2D materials.

1

Background and techniques

The idea behind spintronics, to employ spins in *non-magnetic materials* (NM) for information storage and processing, is ambitious. The spin degree of freedom of an electron possesses only a short lifetime due to interactions with the host material. This results for NM generally in an equilibrium state without a dominant spin orientation. Thus, current research focuses on the exploration of possibilities to create non-equilibrium spin accumulations with long lifetimes, to transport and manipulate them. There are several techniques which employ different effects to create a non-equilibrium spin distribution in a NM. Spin polarizations created by optical excitation or electrically injection from a *ferromagnet* (FM) are the most common techniques, but also the so-called *spin Hall effect* (SHE), using different scattering directions of the spins, can also be employed to create spin accumulations within a material [15, 32, 33].

A non-equilibrium spin polarization can be created optically by illuminating a material with circular polarized light [10]. The angular momentum of the light is transferred into the spin momentum of the electrons, also known as *optical orientation*. This process is highly efficient for direct band gap materials, such as III-V *semiconductors* (SC), but it has also been demonstrated in Si with a spin polarization of a few percent [10]. This is mainly due to the short spin relaxation time compared to the recombination time of the spins. By engineering a *light emitting diode* (LED)

band structure, this effect can be reversed to measure spin accumulations by detecting the circular polarization of the light emitted by this so-called *spin-LED* [11]. Similarly, a spin-laser band structure has been recently engineered to intrinsically pump spin polarized electrons and generate coherent polarized light [34].

A simpler and more viable way for applications is the injection of spins electrically from a spin polarized source. Ferromagnets have been established as such sources, since they exhibit an intrinsic spin polarization in thermal equilibrium. A current from a FM into a NM is consequently spin polarized and creates a non-equilibrium spin accumulation in the NM. The electric potential probed by a FM contact is also spin dependent. This means that FMs can be used in an all-electrical setup to create and detect spin polarizations in NM. That is advantageous, since it is simple to fabricate, to control and better aligned with possible future integration into logic devices.

Initially such contacts were not easy to realize, since the *conductivity mismatch* between the FM and the NM yields a low efficiency of the spin transfer. This motivated the idea of introducing a *tunnel barrier* (TB) [35]. Using FM tunnel contacts lead to several breakthrough achieving large spin accumulations in NM materials, including in graphene [36] and silicon [18] at room temperature, which encourages developments for applications for everyday technology. Since then, a race to optimize fabrication techniques and study new materials started. Not only different substrates are investigated, but also FM and TBs, since they can affect the spin accumulation inside the substrate significantly.

Here we discuss the basic idea of spin injection and detection with a FM. Consequently, its drawbacks and experimental solutions are presented. Finally, we present the recent advances made in different materials, such as Si, graphene, *hexagonal boron nitride* (h-BN), *transition metal dichalcogenides* (TMDC) and *topological insulators* (TI).

1.1 Ferromagnetism and spin polarization

Magnetism in general stems from the unpaired spins of the electrons. In FM transition metals, such as iron, cobalt and nickel, the 3d orbital is not fully occupied, so electrons can arrange freely according to the *Hund's rules* and the *Pauli principle* to achieve the configuration with the lowest energy. The energy difference between parallel (triplet) and anti-parallel (singlet) spin configuration is the so-called exchange energy. If the gain in exchange

energy of a parallel spin alignment is larger than the increase in kinetic energy, the material exhibits a finite magnetization in thermal equilibrium and is called a FM. This results in a splitting of the *density of state*s (DOS) at the Fermi level, which means the available states N for up-spins is larger than for down-spins[1]: $N_\uparrow > N_\downarrow$. This can be used to define the intrinsic spin polarization in the FM as

$$P = \frac{N_\uparrow - N_\downarrow}{N_\uparrow + N_\downarrow}. \tag{1.1}$$

More interesting is the spin polarization of an electron current. In 1936, Mott proposed that a charge current is made of two independent spin currents [4, 5]. He realized that FMs exhibit a spin dependent scattering when magnon scattering is suppressed. Consequently, the conductivity σ can be expressed as the sum of two independent, but spin dependent conductivities $\sigma_\uparrow$ and $\sigma_\downarrow$: $\sigma = \sigma_\uparrow + \sigma_\downarrow$. This is known as the two-current model and has since been further developed [37, 38]. These spin dependent conductivities can be expressed in the Einstein equation as

$$\sigma_{\uparrow\downarrow} = N_{\uparrow\downarrow} e^2 D_{\uparrow\downarrow}, \text{ with } D_{\uparrow\downarrow} = \frac{1}{3} v_{F\uparrow\downarrow} l_{e\uparrow\downarrow}, \tag{1.2}$$

where e is the electron charge and $D_{\uparrow\downarrow}$ is the spin dependent diffusion constant, expressed as a function of the Fermi velocity $v_{F\uparrow\downarrow}$ and the mean free path of the electron $l_{e\uparrow\downarrow}$. Ferromagnets, FM insulators and their interfaces show this spin dependent conductivity, where the polarization of the current can be written as

$$P = \frac{\sigma_\uparrow - \sigma_\downarrow}{\sigma_\uparrow + \sigma_\downarrow} \tag{1.3}$$

and is experimentally obtained for Fe (45%), Co (42%), Ni (27%) [39] as well as some tunnel interfaces [28]. In the literature, P is often referred to as β or γ to distinct between the bulk and the interface polarization, respectively.

For interfaces between a FM and a NM the spin dependent conductance can be defined as $G_{\uparrow\downarrow} = \left(R^I_{\uparrow\downarrow}\right)^{-1}$, where $R^I_{\uparrow\downarrow}$ is the spin dependent resistivity of the barrier.
Equation (1.3) can also be directly used to describe the resistance switching in *magnetic tunnel junctions* (MTJ). In a MTJ two FMs are separated by a thin insulating barrier. Altering the magnetization configuration between

[1] We define the up-spins in general as majority spins.

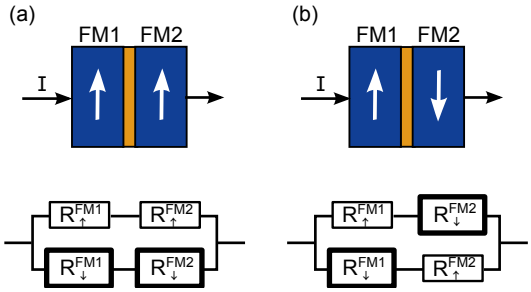

Figure 1.1: Schematic and resistor model of a ferromagnet (FM)/tunnel barrier (TB)/FM structure with (a) parallel magnetization orientation and (b) anti-parallel magnetization orientation. The FM resistance for up-spins is lower than the resistance for down-spins.

the FMs (either parallel or anti-parallel) results in a change in the measured resistance across this heterostructure (Figure 1.1). Assuming the spin is preserved while tunnelling, the *tunnel magnetoresistance* (TMR) can be extracted:

$$TMR = \frac{G_p - G_{ap}}{G_p + G_{ap}} = \frac{2\gamma_1\gamma_2}{1 - \gamma_1\gamma_2}, \tag{1.4}$$

where G_p and G_{ap} is the conductivity through the FM layers for parallel and anti-parallel magnetization orientation, respectively. The right hand side of Equation (1.4) can be derived using Equation (1.3) in the different resistance configurations, whereas γ_1 and γ_2 are the interface polarizations of FM1 and FM2, respectively. These polarizations were historically believed to be the intrinsic FM polarization defined by the DOS [40], but experiments demonstrated that the polarization is very sensitive to the used interface material, its transparency, roughness and contamination, especially within the first few atomic layers of the interface [7]. Also the crystal structure and lattice matching of both FM and insulator seem to have a significant influence. Therefore, MTJ structures are nowadays used to characterize interfaces and barrier materials. This interface dependency is also relevant for transparent and tunnelling junctions on NM, which will be discussed in the next sections.

1.2 Spin scattering mechanisms

Spins in any material exhibits only a finite lifetime due to SO and *hyperfine* (HF) interactions. This spin lifetime τ, together with the spin diffusion constant D, are important parameters in spintronics, since they define the

possible distance a spin can be transported:

$$\lambda = \sqrt{D\tau}. \tag{1.5}$$

Two main mechanism contribute to the spin relaxation due to SO interactions: *Elliott-Yafet* (EY) and *D'yakonov-Perel* (DP) [1].

The EY mechanism describes a coupling between the up- and down-spin state due to lattice symmetry in presence of scattering centres, such as phonons, boundaries or impurities. That means a scattering electron has a finite probability to flip its spin state. The spin flip probability increases with the scattering probability, which scales also with the atomic mass and size of the atoms. This was first discussed for elemental metals, but applies also for most pure crystals to a certain degree and its strength depends mainly on the mass of the constituent atoms. Silicon and graphene have a low atomic mass and hence exhibit a low SO coupling due to EY, which should result in long spin lifetimes. In contrast, TIs, such as Bi_2Se_3, have a strong SO interaction, which gives rise to their atypical band structure (see Section 1.6.5).

D'yakonov-Perel describes a mechanism in systems without inversion symmetry. The presence of two distinct atoms in the Bravais lattice leads to bulk inversion asymmetry (*Rashba-Dresselhaussen*). A built-in or external electric field yields structural inversion asymmetry (*Bychkov-Rashba*). Both types result in an *electrostatic potential gradient* $\vec{E}$. Spins moving with a velocity $\vec{v}$ (relative to the speed of light c) through this electric field are affected by an effective *magnetic field* $\vec{B} = \frac{\vec{v}}{c} \times \vec{E}$. If the coupling is strong enough, this translation can be employed to manipulate the spins within the material by using an external electric field (also called *Rashba effect*). Transition metal dichalcogenides have a large atomic mass and exhibit no inversion symmetry resulting in a strong SO interaction due to EY and DP. Despite the enhanced spin scattering, a valley splitting occurs, which are occupied by different spin states and highly interesting for spintronic applications (see Section 1.6.3).

The HF interaction is a coupling of the magnetic moments of the electrons and the nuclei. This interaction dominates for localized electrons, for example in quantum wells or quantum dots. It is negligible if the magnetic moment of the nuclei is zero, which occurs for systems with a full nuclear shell, for example silicon (^{28}Si) and graphene (^{12}C). Inducing HF interaction in graphene can be achieved by artificially growing it with an isotope with a remaining nuclear spin, for example ^{13}C [41]. Alternatively, the material *black phosphorous* (BP), whereof a 2D layer is called phosphorene,

has similar properties as TMDCs, but a natural nuclear spin resulting in a strong HF coupling.

In practice, crystals are not ideal, intentionally or unintentionally doped, contain impurities, adatoms, lattice errors and ripples for 2D materials, which can induce scattering centres and have to be considered as possible factors reducing the spin lifetime.

1.3 Spin injection and accumulation

In a NM the conductivities for up- and down-spins are identical. That means that an applied current through a FM/NM junction experiences a discontinuity in the spin dependent conductivity. This yields to the creation of a spin accumulation at the interface and hence a splitting of the chemical potential for both kinds of spins, $\mu_\uparrow$ and $\mu_\downarrow$. A general definition for the electrochemical potential is

$$\mu = \frac{n}{N}, \tag{1.6}$$

where N is the available states at the Fermi level and n is the excess particle density. The spin accumulation decays exponentially within the FM and the NM with a respective penetration depth λ_{FM} and λ_{NM} (see Figure 1.2). The spin dependent current density $j_{\uparrow\downarrow}$ can be expressed by[2]

$$j_{\uparrow\downarrow} = \frac{\sigma_{\uparrow\downarrow}}{e}\partial_x \mu_{\uparrow\downarrow}. \tag{1.7}$$

This current can gradually change when spin flip processes are considered. Introducing the spin flip times $\tau_{\uparrow\downarrow}$ for an up to down spin-flip and $\tau_{\downarrow\uparrow}$ for the revered process leads to the expression

$$\frac{1}{e}\partial_x j_{\uparrow\downarrow} = \mp\frac{n_\uparrow}{\tau_{\uparrow\downarrow}} \pm \frac{n_\downarrow}{\tau_{\downarrow\uparrow}}. \tag{1.8}$$

In thermal equilibrium no net spin scattering should take place and

$$\frac{N_\uparrow}{\tau_{\uparrow\downarrow}} = \frac{N_\downarrow}{\tau_{\downarrow\uparrow}}. \tag{1.9}$$

A diffusion equation, describing the complete spin flip process, can be obtained by combining Equations (1.2) and (1.9):

$$\partial_x^2 \left(\mu_\uparrow - \mu_\downarrow\right) = \frac{\left(\mu_\uparrow - \mu_\downarrow\right)}{D \cdot \tau}, \tag{1.10}$$

[2]We assume a simplified one-dimensional (1D) channel along the current direction. Equally, this model can be extended into three dimensions.

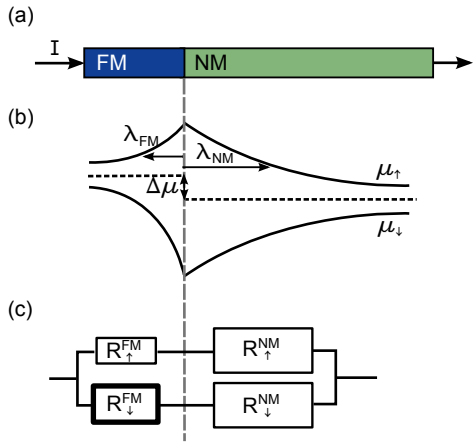

Figure 1.2: Spin current through a FM/NM interface. (a) Schematic of a FM/NM junction. (b) Chemical potentials for up- and down-spins at the barrier-free interface. A splitting $\Delta\mu$ between the equilibrium potentials occurs due to the spin dependent conductivities in the FM. The spin diffusion length is usually much shorter for FM than for NM. The potential drop due to the applied current is neglected in this diagram. (c) Equivalent resistor network for this junction. The spin dependent resistances in the FM are small compared to the NM.

where the spin lifetime is defined as $\tau = \left(\tau_{\uparrow\downarrow}^{-1} + \tau_{\downarrow\uparrow}^{-1}\right)^{-1}$ and the average spin diffusion constant can be written as $D = \frac{D_\uparrow D_\downarrow \left(N_\uparrow + N_\downarrow\right)}{N_\uparrow D_\uparrow + N_\downarrow D_\downarrow}$. Equation (1.10) can generally be solved as

$$\mu_\uparrow - \mu_\downarrow = \tilde{a} \cdot \exp\left(-\frac{x}{\lambda}\right) + \tilde{b} \cdot \exp\left(\frac{x}{\lambda}\right), \tag{1.11}$$

where λ comes from Equation (1.5), and $\tilde{a}$ and $\tilde{b}$ are integration constants. Using the ansatz where the charge current is conserved, that means $\partial_x j = \partial_x \left(j_\uparrow + j_\downarrow\right) = 0$, and Equation (1.7), the chemical potential for both spins can be separately derived as

$$\mu_{\uparrow\downarrow} = a + b \cdot x \pm \frac{c}{\sigma_{\uparrow\downarrow}} \exp\left(-\frac{x}{\lambda}\right) \pm \frac{d}{\sigma_{\uparrow\downarrow}} \exp\left(\frac{x}{\lambda}\right). \tag{1.12}$$

For a FM/NM contact the constants a, b, c and d can be determined assuming that at the interface the spin dependent electrochemical potentials are continuous, the spin currents are conserved, and interface scattering and resistances are neglected [42]. Defining the equilibrium chemical potential

$\mu = P\mu_\uparrow + (1-P)\,\mu_\downarrow$, a potential difference can be derived as

$$\Delta\mu = \mu_{FM} - \mu_{NM} = \frac{\beta^2 \left(\frac{\lambda_{NM}}{\sigma_{NM}}\right)\left(\frac{\lambda_{FM}}{\sigma_{NM}}\right)\cdot eI}{\left(\frac{\lambda_{FM}}{\sigma_{NM}}\right) + (1-\beta^2)\left(\frac{\lambda_{NM}}{\sigma_{NM}}\right)}, \tag{1.13}$$

where β is the intrinsic spin polarization of the FM defined in (1.1), and λ and σ describe the spin diffusion length and total conductivity, respectively, in either the FM or NM. Dividing Equation (1.13) by eI a spin coupled interface resistance R_I arises (see Figure 1.2b). That is remarkable, since we neglected any other interface resistances and stems simply from the discontinuity of the conductivities across the barrier. Furthermore, Equations (1.12) and (1.13) define the spin splitting $2\mu_0$, which is at its maximum at the interface:

$$2\mu_0 = \mu_\uparrow - \mu_\downarrow = \frac{2\Delta\mu}{\beta}, \tag{1.14}$$

whereas $\pm\mu_0$ describes directly the chemical potential for up and down spins in the NM, respectively. Equation (1.3) and (1.13) can be used to derive the spin polarization of the current through the interface

$$\gamma = \frac{I_\uparrow - I_\downarrow}{I_\uparrow + I_\downarrow} = \frac{\beta\frac{\lambda_{FM}}{\sigma_{FM}}}{\frac{\lambda_{FM}}{\sigma_{FM}} + (1+\beta^2)\frac{\lambda_{NM}}{\sigma_{NM}}}. \tag{1.15}$$

This shows that the spin coupled interface resistance, the potential splitting and the spin polarization mainly depend on the ratios $\frac{\lambda_{FM}}{\sigma_{NM}}$ and $\frac{\lambda_{NM}}{\sigma_{NM}}$. As discussed earlier, most FM have a small spin diffusion length, $\lambda_{FM} \ll \lambda_{NM}$. Therefore, the denominator in Equation (1.15) becomes much larger than the numerator, hence the current polarization P is reduced. This becomes even more pronounced when injecting into SCs, since they usually exhibit a much lower conductivity than metals. This problem is therefore known as *conductivity mismatch*. Spins injected in the NM have a high tendency to diffuse back into the FM, where they decay faster, due to the high SO coupling and short spin diffusion length. This mismatch can be solved by introducing a TB.

1.4 Spin injection and detection with tunnel contacts

Tunnel barriers play a crucial role for spin injection. Coupled to a FM they provide a high spin dependent resistance and therefore enhance the

magnitude of the spin signal (Figure 1.3). Their high spin dependent resistance circumvents the conductivity mismatch problem and prevents spins, once injected in the NM, to diffuse back into the FM and losing their spin information faster. Therefore, spin injection and detection through a TB shows a much higher efficiency than a direct contact and is well established as reliable source for spin currents [18, 28, 36, 43].

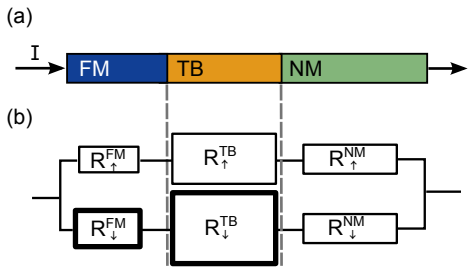

Figure 1.3: Spin current through a FM/TB/NM interface. (a) Schematic of a FM/TB/NM junction with a TB. (b) Equivalent resistor network for this junction. The spin dependent resistances in the TB are large compare to the NM and the FM.

Even though the idea seems simple, there are various configurations in which spin accumulations and transport can be created and measured in different materials. This section describes three common techniques, which were used for the studies discussed in the following chapters.

1.4.1 Local magnetoresistance measurement

Applying a current through two FM tunnel contacts connected by a NM is a simple way to create a non-equilibrium spin accumulation. On one hand, this often called two-terminal configuration can be easily fabricated, either in a vertical stacked structure, similar to MTJs, or in a lateral transistor-like configuration. The latter is particularly interesting, since such a setup is easy to implement on new materials and allows to use either a top or a back-gate to manipulate spin currents using the Rashba effect (see Section 1.2). On the other hand, the simple structure leaves many boundary conditions, which have to be evaluated.

The two FM contacts create localized spin accumulations at their interface when applying an electric current, which move mainly through the electromagnetic potential of the applied electric field. An in-plane magnetic field can switch the FMs at their intrinsic coercive fields. This results in a difference of the resistance between the parallel and the anti-parallel

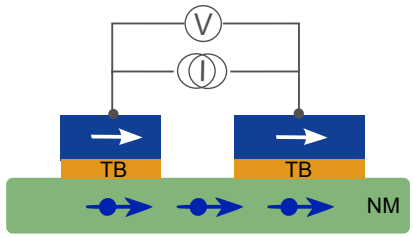

Figure 1.4: Local magnetoresistance measurement configuration. Spins are injected from a FM through a TB and can be detected by a second FM contact within the spin diffusion length of the material. The spin and charge transport are both driven by the applied electric field.

magnetization configuration of the FMs, which is detected as a step in a so called *spin valve* measurement (see Figure 1.5). Depending on the geometry additional boundary effects have to be considered: 1) For a lateral structure with an open or even infinite channel on either side of the electrodes (such as in Figure 1.4), the spins can diffuse away from the contacts against the electric field. 2) For a lateral structure confined between the two contacts (identical to a vertical structure), diffusion loses can be neglected. For the following discussion we assume the latter case, whereas the former can be derived similarly and just differs by a correction factor [35, 38].

The combined spin and charge current in the NM results in a solution for Equation (1.12) with non-zero values for the linear prefactors and both exponential terms due to the spin potential contribution by both FM contacts [38]. Taking the conservation of current into account, the magnetization alignment dependent resistances can be derived (see Equations (41) and (42) in [38]). Defining the resistance change between parallel (R_p) and anti-parallel (R_{ap}) magnetization orientation as $\Delta R = R_{ap} - R_p$, it can be fully expressed by

$$\Delta R = \frac{2\left(\beta R_{FM} + \gamma R_B\right)^2}{\left(R_B + R_{FM}\right)\cosh\left(\frac{t_{NM}}{\lambda_{NM}}\right) + \frac{R_{NM}}{2}\left[1 + \left(\frac{R_B}{R_{NM}}\right)^2\right]\sinh\left(\frac{t_{NM}}{\lambda_{NM}}\right)}. \tag{1.16}$$

Equation (1.16) requires the bulk polarization β and resistance R_{FM} of the FM, the interface polarization γ and resistance R_B of the insulating barrier, as well as the thickness t_{NM} and spin diffusion length λ_{NM} of the NM. The resistance for a parallel magnetization orientation is

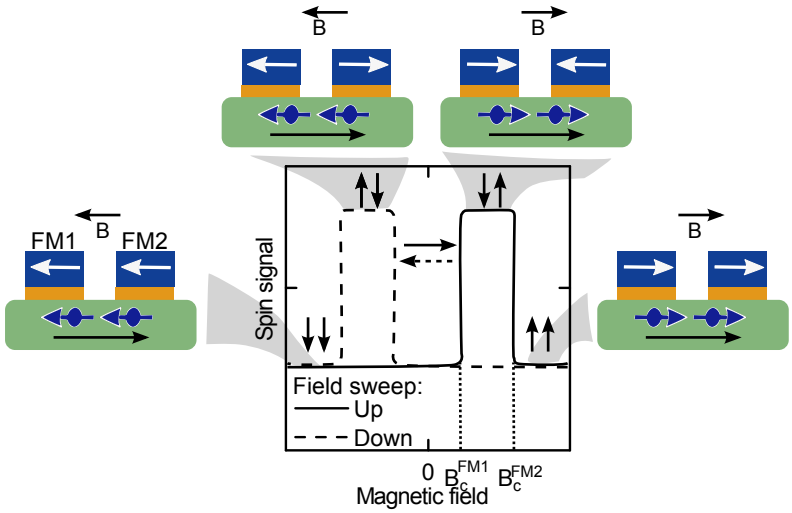

Figure 1.5: Spin signal line shape for a spin valve measurement. An applied in-plane magnetic field is swept from a negative to positive field (up sweep) and back to a negative field (down sweep). Meanwhile, it switches the magnetization directions of FM1 and FM2 at their coercive fields B_c^{FM1} and B_c^{FM2}, respectively. The spin signal reflects the detected magnetoresistance between a parallel and anti-parallel magnetization alignment.

$$R_{\uparrow\uparrow} = 2\left(1-\beta^2\right)R_{FM} + R_{NM}\frac{t_{NM}}{\lambda_{NM}} + 2\left(1-\gamma^2\right)R_B + 2\frac{\left(\beta-\gamma\right)^2 R_{FM}R_B + R_{NM}\left(\beta^2 R_{FM} + \gamma^2 R_B\right)\tanh\left(\frac{t_{NM}}{2\lambda_{NM}}\right)}{R_{FM} + R_B + R_{NM}\tanh\left(\frac{t_{NM}}{2\lambda_{NM}}\right)}. \tag{1.17}$$

The *magnetoresistance* (MR) is then defined as

$$MR = \frac{\Delta R}{R_{\uparrow\uparrow}}. \tag{1.18}$$

This result is very general and discussed for several structures in [35]. In the case of a FM/NM/FM structure without barrier resistance, thin and low resistive NM, Equation (1.18) becomes similar to Equation (1.4). Since MTJs usually have NM with varying resistances, it illustrates immediately

why it strongly depends on the interface layer and not only on the employed FM (as mentioned in Section 1.1).

A more realistic case is the FM/I/NM/I/FM structure with a barrier *interface* (I) between the FM and the NM. If we assume a SC NM, its resistance is usually much larger than the FM ($R_{NM} \gg R_{FM}$). That results in a confined range for the barrier resistance R_B to observe a significant MR:

$$R_{NM}\frac{t_{NM}}{\lambda_{NM}} \ll R_B \ll R_{NM}\frac{\lambda_{NM}}{t_{NM}}. \tag{1.19}$$

Physically this is easy to be understood: On one hand, if the barrier resistance is too small, the discontinuity in the chemical spin potential (see Section 1.3) introduced by the barrier is too small to create a significant spin accumulation. On the other hand, the finite spin lifetime limits the spin potential splitting, whereas the absolute potential increases with barrier resistance. This results in a drop of the MR if the barrier resistance becomes too large. Therefore, the barrier resistance needs to be optimized to achieve a high and detectable spin accumulation. Equation (1.18) is an excellent tool to predict this required resistance for contacts on novel materials.

It has to be mentioned that the combined spin and charge currents in the two-terminal structure can cause several effects which distort or affect the spin signal. Stray fields on the edges of the FM and external magnetic fields affect the current causing Hall effects, anisotropic MR [14], interference effects [44], and magneto-coulomb effects [45]. Even though this setup is highly interesting for applications, basic research tries to avoid these effects by using a *non-local* (NL) configuration.

1.4.2 Non-local spin transport measurement

In a NL measurement a spin accumulation is created in one circuit and detected in a separate pair of contacts (Figure 1.6). Spin and charge current are separated and the spins are transported from the injection contact to the detection contact by diffusion. Defining the position of the injector as $x = 0$, Equation (1.12) can be solved as

$$\mu_{\uparrow\downarrow} = \pm\mu_0 \cdot \exp\left(-\frac{x}{\lambda_{NM}}\right) \text{ for } x \geqq 0. \tag{1.20}$$

The individual spin currents through the interface can be written as

$$I_{\uparrow\downarrow} = \frac{I}{2} \pm \frac{\mu_0 \sigma_{NM} A}{e\lambda_{NM}}, \tag{1.21}$$

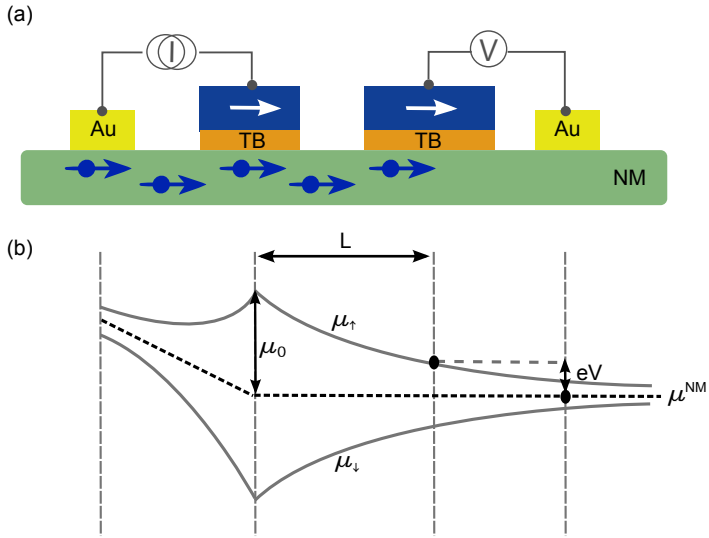

Figure 1.6: Non-local spin transport measurement configuration. (a) Schematic setup: spins are injected from a FM through a TB in the left circuit and can be detected in a similar circuit on the right. The spin transport in the non-magnetic material (NM) is diffusive. (b) The electrochemical potentials for up- and down-spins in the NM. The diffusing spins create a finite potential difference between either kind of spin potential, probed by the FM, and the equilibrium potential, probed by the Au contact.

where A is the cross section of the contact and I is the total tunnel current. The potential splitting at the interface ($x = 0$) can now be written as

$$2\mu_0 = e\left(V_\uparrow - V_\downarrow\right) = e\left(I_\uparrow R_\uparrow^{TB} - I_\downarrow R_\downarrow^{TB}\right) = \frac{eIR_{NM}\gamma_i}{1 + 2\frac{R_{NM}}{\left(R_\uparrow^{TB}+R_\downarrow^{TB}\right)}}, \tag{1.22}$$

where γ_i is the injecting FM/I/NM interface spin polarization and the NM resistance is defined as

$$R_{NM} = \frac{\lambda_{NM}}{\sigma_{NM}A} = R_\square \frac{\lambda_{NM}}{W}, \tag{1.23}$$

with the square resistance $R_\square$ and width W of the NM channel. If the ratio $\frac{R_{NM}}{\left(R_\uparrow^{TB}+R_\downarrow^{TB}\right)} = \frac{R_{NM}}{R_{TB}}$ in Equation (1.22) is large, then the spin potential splitting is reduced, identical as in the two-terminal model (Section 1.4.1). If the tunnel resistance is much larger than the NM resistance, the Equation (1.22) is simplified to

$$2\mu_0 = \mu_\uparrow - \mu_\downarrow = eIR_{NM}\gamma_i \tag{1.24}$$

at the injector electrode.

The electrochemical potential is detected by a FM contact at a position $x = L$ defined by the sample geometry. Assuming that no net charge current flows through the detector, the detected potential is

$$\mu_{FM}(L) = \frac{\gamma_d \left[\mu_\uparrow(L) - \mu_\downarrow(L)\right]}{2} + \frac{\mu_\uparrow + \mu_\downarrow}{2}. \tag{1.25}$$

In contrast, a NM reference contact detects $\mu_{NM} = \frac{1}{2}\left[\mu_\uparrow + \mu_\downarrow\right]$ independent of its placement, since it exhibits no spin polarization. With Equation (1.20), (1.23), (1.24) and (1.25) one can calculate the NL voltage as:

$$V_{NL} = \frac{\mu_{FM} - \mu_{NM}}{e} = \pm\frac{\gamma_i \gamma_d R_\square \lambda_{NM}}{2W} \exp\left(-\frac{L}{\lambda_{NM}}\right). \tag{1.26}$$

This voltage can be measured by the detector in reference to a NM contact, or in reference to a FM contact at an infinite distance (see detector circuit in Figure 1.6). The signal is positive if the magnetization of the detector and injector are parallel, and vice versa. This is similar to the *spin valve signal* presented in Figure 1.5 of Section 1.4.1, except that the spin current is driven diffusively between injector and detector electrode. It is measured by sweeping a magnetic field $B_\parallel$ in-plane and magnetization direction. By fabricating the injector and detector accordingly, different switching fields are achieved (Section A.3.3.3). This allows to distinct between both magnetization orientations in one magnetic sweep where a step of $2V_{NL}$ can be observed (see Figure 1.5). This step equals the voltage difference between the parallel and anti-parallel configuration during the field sweep.

Non-local Hanle measurement

The Hanle effect can be used to control the dephasing of the spins by an external magnetic field. This is detected as a reduction of the voltage signal in Equation (1.26). In contrast to the NL spin valve signal, a magnetic field $B_\perp$ is applied perpendicular to the magnetization, hence also to the spin polarization direction. This causes the spins to precess with the Larmor frequency

$$\omega_\mathrm{L} = \frac{g\mu_B B_\perp}{\hbar}. \tag{1.27}$$

The precession yields to a dephasing of the spins and consequently the polarization is lost. This effect was first observed by Wood and Ellett in 1923, and described by Hanle in 1924 [46]. For ballistic transport the spin

potential would just vary with the Larmor frequency, which adds a factor of $\cos(\omega_L t)$ to Equation (1.26). That means the spin dependent potentials decay with increasing distance L of the detector, while the part of the spin orientation parallel to the detectors magnetization alters cosinusoidally (Figure 1.7). In a more realistic case, the spins diffuse randomly. The distribution

$$\wp_D(t) = \sqrt{\frac{1}{4\pi D t}} \exp\left(-\frac{L^2}{4Dt}\right) \tag{1.28}$$

describes the probability that a electron injected at $x = 0$ arrives at the detector at $x = L$ after time t. This is in principle identical to the solution of Equation (1.20). Taking additional scattering and possible spin flips into account adds a factor $\wp_t(t) = \exp\left(-\frac{t}{\tau}\right)$ to Equation (1.28), describing the probability for a charge carrier to preserve its spin state after a spin dephasing time t. Since diffusion is random, the potential is a sum of all spins injected over all diffusion times $\mu(L,B) = \int_0^\infty \mathrm{d}t \mu(L,B,t)$.With the boundary condition $\mu(L=0, B=0) = \mu_0$ we derive

$$\mu(L,B) = 2\sqrt{\frac{D}{\tau}} \int_0^\infty \mathrm{d}t \wp_D(t) \exp\left(-\frac{t}{\tau}\right) \cos(\omega_L t)\,. \tag{1.29}$$

This can be used with Equation (1.24) and (1.26) to express the obtained voltage at a detector contact at $x = L$:

$$V_{NL}(B_\perp) = \pm \frac{\gamma_i \gamma_d R_\square I}{W} \int_0^\infty \underbrace{\sqrt{\frac{D}{4\pi t}} \exp\left[-\frac{L^2}{4Dt}\right]}_{1} \underbrace{\cos[\omega_L t]}_{2} \underbrace{\exp\left[-\frac{t}{\tau_{sf}}\right]}_{3} \mathrm{d}t, \tag{1.30}$$

where the positive and negative sign considers the parallel and anti-parallel contact magnetization orientation, respectively. The main factors introduced above, which are contributing to the signal are spin diffusion (1), spin precession (2) and spin dephasing (3). A characteristic Hanle curve for the diffusive transport is shown in Figure 1.7 in comparison to a ballistic transport measurement. Equation (1.30) can be further solved with *Mathematica* to

$$V_{NL}(B_\perp) = \pm \frac{\gamma_i \gamma_d R_\square I}{W} \cdot \mathrm{Re}\left(\frac{\exp\left(-L\sqrt{\frac{\omega}{D}}\right)}{2\sqrt{D\omega}}\right), \tag{1.31}$$

where $\omega = \frac{1}{\tau} - i\omega_L$ is a combination of the frequency of spin flips due to interaction and additional Larmor precession. Equation (1.31) is essential

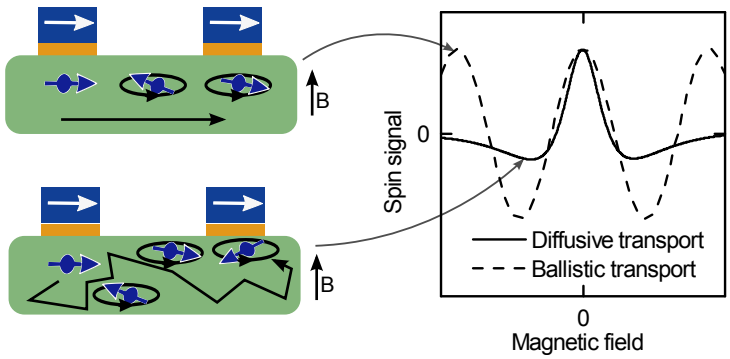

Figure 1.7: Spin signal line shape for non-local geometry. With an applied perpendicular magnetic field the ballistic spin transport yields to an in-phase oscillation of the spins and therefore a cosinusoidal spin signal. The spin signal for diffusive transport is the sum of all spins, that means all diffusion times, under the detector.

in the discussion of the measurements, since it allows to extract the spin polarization at the interfaces γ_i and γ_d, as well as the spin lifetime τ.

The distance L between injector and detector contacts should be approximately the spin diffusion length λ of the material, which is usually of the order of nanometres up to a few micrometer, depending on the intrinsic charge and spin properties. This demonstrates a disadvantage of the NL technique for smaller channel length, since it requires a fabrication technique with a high precision. By reducing L to zero and therefore combining the two contacts, a *three-terminal* (3T) configuration emerges.

1.4.3 Three-terminal Hanle measurement

The 3T configuration is an extreme of the NL setup, where the distance L between injector and detector becomes zero (Figure 1.8). Therefore,

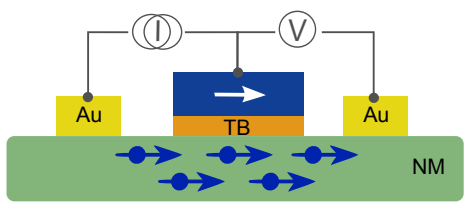

Figure 1.8: Schematic of a three-terminal measurement setup. Spins are injected and detected through the same FM TB.

Equation (1.31) can be simplified to

$$V_{3T}\left(B_{\perp}\right) = \frac{\gamma^2 R_{\square} I}{W} \cdot \frac{\cos\left(\frac{1}{2}\arctan\left(-\omega_{\mathrm{L}}\tau\right)\right)}{2\tau\sqrt{D}\sqrt[4]{\frac{1}{\tau^2}+\omega_{\mathrm{L}}^2}}. \tag{1.32}$$

Since injector and detector are identical, the magnetization direction is always parallel, the alternating sign becomes unnecessary and the injector and detector polarization is identical ($\gamma^2 = \gamma_i\gamma_d$). Even though this equation gives a good theoretical representation of the observed data, it is common to use the original approach by Hanle [18, 47, 48], which describes the effect empirically and provides comparable spin parameters.

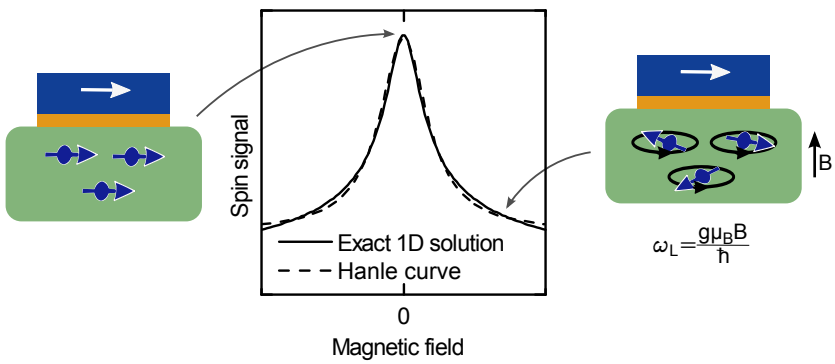

Figure 1.9: Spin signal line shape for three-terminal geometry. The spins dephasing with increasing field yields to a reduction in the obtained signal. Comparing the exact 1D approximation and the Hanle fitting shows that the latter underestimates the spin lifetime.

The 3T technique probes the spin potential directly under the contact. That means spins diffuse in all directions from a quasi-static spin accumulation, which is only affected by the external magnetic field. With such an approach, Hanle derived that the potential drops with a Lorentzian with increasing magnetic field:

$$\mu_0 = \frac{\mu_0\left(0\right)}{1+\left(\omega_{\mathrm{L}}\tau\right)^2}. \tag{1.33}$$

Together with Equation (1.24) and (1.25) a magnetic field dependence of the voltage signal can be derived:

$$V_{3T} = R_B I + \gamma\mu_0. \tag{1.34}$$

Comparing the experimental parameters derived by Equations (1.32) and (1.34), the latter usually underestimates the spin lifetime (Figure 1.9). In practice, the 1D simplification is considered as a possible weak point and the underestimation of the spin lifetime by Equation (1.34) is accepted [28, 49]. Besides the simplicity of the theory, the 3T configuration is in general simpler to fabricate than the NL one, since the methods to place the injector and detector in a close distance are not required.

1.5 Other techniques

The techniques presented in the previous chapters are universally applicable for measuring spin transport. Introducing for example SO scattering not only affects the intrinsic spin properties, but also requires the consideration of other effects. These effects can be employed to study additional properties to further characterize the material for spintronic applications.

This section gives a short introduction into the Edelstein, spin-galvanic and localization effects, which were used to extract material-dependend properties discussed in this thesis.

1.5.1 Detection of current-induced spin polarizations

Some materials exhibit a momentum dependent spin orientation (*spin-momentum locking*) due to a strong SO coupling (see Section 1.6.5). In TIs a confinement in the *topological surface states* (TSS) gives the possibility to generate spin polarized currents by applying an electric field (Edelstein effect). The inverse effect (spin-galvanic effect) can generate a charge current from a local spin accumulation created by spin-pumping or electrical injection. Considering the Edelstein effect, we can estimate the detected voltage signal of a FM tunnel contact on such a spin-polarized charge transport channel.

The spin density n in the TSS induced by the charge current density j is defined as $n = j/(ev_{\mathrm{F}})$, where v_{F} is the Fermi velocity and e is the electron charge [50]. These non-equilibrium spins relax with a characteristic time τ which yields a spin current j_s [51]. The current conservation gives

$$j_s = \frac{\hbar}{2e}\eta\gamma_{FM}\gamma_S j_i = \frac{\hbar}{2}\frac{n}{\tau},$$

where j_i is the injected current density, and γ_{FM} and γ_S are the spin polarizations of the FM tunnel contact and the surface state, respectively.

The correction factor η takes the current contribution of the TSS into account. This is in particular necessary for highly doped TIs, where the bulk can dominate, allowing a contribution from the surface of only a few percent [52, 53], whereas an ideal TI should exhibit a pure surface current: $\eta = 1$. Introducing the geometries of the measurement devices we derive

$$\Delta V = \eta \gamma_S \gamma_{FM} R I \frac{l_{mf}}{L}, \tag{1.35}$$

where R and L are the resistance and the length of the TI channel, respectively. Due to the strong SO interaction the spin relaxation time can be assumed equal to the momentum relaxation time, which implies that the mean free length is $l_{mf} \approx v_{\mathrm{F}} \tau$ [54]. Strikingly, Equation (1.35) is similar to Equation (1.26), but considers the contribution η of the TSS, which carry the actual spin accumulation.

1.5.2 Localization measurements

Without an external magnetic field and in absence of SO interaction, a coherent pair of electron waves scattered by impurities interferes constructively, which is called *weak localization* (WL). This quantum interference occurs at the scale of the *coherence length* l_φ and yields a reduction of the conductance around zero magnetic field. In contrast, a strong SO interaction causes the scattering electron waves to gain opposite phases. This causes a destructive scattering and enhances the conductance, which is known as the *weak anti-localization* (WAL) effect. Increasing an out-of-plane magnetic field $B_\perp$ adds a phase shift, which reduces gradually the interference. That yields to a sharp peak in the conductance, which increases with magnetic field strength for WL, and decreases for WAL. This reduction can be explained by the *Hikami-Larkin-Nagaoka* (HLN) model [55]. In this model, the conductivity correction $\Delta\sigma\left(B_\perp\right)$ is given by

$$\Delta\sigma\left(B_\perp\right) = \alpha \frac{e^2}{\pi h} \left[\ln \frac{\hbar}{4 e l_\varphi B_\perp} - \psi\left(\frac{1}{2} + \frac{\hbar}{4 e l_\varphi B_\perp}\right)\right], \tag{1.36}$$

where ψ represents the digamma function and the prefactor α describes the scattering system [55]. The latter scales the signal depending if it belongs to the orthogonal ($\alpha = 1$), unitary ($\alpha = 0$) or symplectic case (α=-$\frac{1}{2}$). An orthogonal system exhibits a weak SO and magnetic interactions (WL). The unitary case exists in systems with weak SO and large magnetic interactions. For the symplectic case a strong SO and magnetic interactions occurs simultaneously. The coherence in the system is strongly material

and temperature dependent, so that graphene exhibits WL up to 100 K [56], whereas TIs demonstrate WAL up to a few tens of Kelvin [57].

1.5.3 Schottky barrier height

The *Schottky barrier height* (SBH) can be measured by performing detailed temperature dependent drain-source current-voltage ($I_{ds} - V_{ds}$) characteristics. A weak temperature dependence is a manifestation of a reduced SBH. The three-dimensional thermionic emission equation describes the electrical transport through a Schottky barrier into a bulk channel at a temperature T [58–60]:

$$I_{ds} = AA^*T^2 \exp\left[-\frac{e}{k_\mathrm{B}T}\left(\Phi_{sb} - \frac{V_{ds}}{f}\right)\right], \tag{1.37}$$

where A is the contact area, A^* is the Richardson constant, e is the electron charge and k_B the Boltzmann constant. Next to the SBH Φ_{sb} Equation (1.37) also requires the ideality factor f of the diode. In practice both parameters can be extracted using several measurements in a narrow temperature range: From an Arrhenius plot ($\ln\left(I_{ds}T^{-2}\right)$ versus T^{-1}) for different bias voltages V_{ds} the slopes $S\left(V_{ds}\right)$ can be extracted and are linear dependent on V_{ds} ($S(V_{ds}) = -\frac{e}{k_\mathrm{B}}\left(\Phi_{sb} - \frac{V_{ds}}{f}\right)$) (for example see Paper VII). The Schottky barrier can be evaluated from the extrapolated value of the slope at zero drain-source voltage ($S_0 = -e\Phi_{sb}k_\mathrm{B}^{-1}$).

1.6 Materials for spintronics

Since the proposal of the spin dependent transport by Mott in 1936 [4, 5], many applications and studies towards possible utilizations, employing this phenomena, have been realized. One of the most well know technologies is the hard disk drive, which uses spin-based elements employing the *giant magnetoresistance* (GMR) [6] and TMR effect [7].

Spin injection, transport and detection in NM has been intensely studied to combine non-volatile memory with logic devices and possibly integrate these circuits into currently existing technology. Since the first proposal for a spin field effect transistor by Datta and Das in 1990 [13], spin transport in metals and SCs, such as InAs [17], Ge [61] and GaAs [16], has been studied. The technologically important Si and several recently isolated *two-dimensional* (2D) crystals enable the development of devices based purely on spin currents, so-called all-spin logic [12].

This section presents different materials and the recent advancements within the fields of spintronics.

1.6.1 Silicon

The interest in *silicon* (Si) for spintronics arises from its proposed excellent spin transport properties compared to metals and other SCs. It has a negligible HF interaction, since its most common isotope (^{28}Si) has no nuclear magnetic moment. Additionally, the spin relaxation is only expected to be induced by the Elliott-Yafet mechanism, which is low due to the lattice inversion symmetry, which results in a weak SO coupling (see section 1.2). Even though 1D and 2D allotropes of Si exist in the form of nanowires [62, 63] and recent discovered silicene [64], they are far behind the developments, whereas bulk Si is currently the primary used SC in applied electronics.

Silicon exhibits an indirect band gap, which makes the optically creation and detection of spin accumulations in the Si conduction band significantly less efficient [10]. Nevertheless, Jonker *et al.* demonstrated the first electrical injection of spins through a Fe/Al_2O_3 tunnel contact in Si and detected it by optical means [11]. The spins diffused within the Si channel and recombined with unpolarized holes in a spin-LED structure fabricated underneath the Si channel. Detecting the polarization of the emitted light reveals a spin polarization in the Si of 30% at a temperature of 85 K.

Even though this result is promising, optical measurements are less suitable for technological integration and all-electrical measurements needed to reproduce similar values. Appelbaum et al. first showed in 2007 the hot-electron spin transport into a Si spin valve structure [43]. They reported spin transport and coherent spin precession over a long distance of 350 μm in undoped Si at 85 K. Unfortunately, a major drawback of the hot-electron approach is that the current levels are too small. Due to the fast energy relaxation of the hot electrons in the FM metals the current in the detection circuit of the device is four orders of magnitude smaller than the injected current. The first all-electrical NL measurement of tunnel spin injection into a lateral structure was realized by van 't Erve et al. in 2007 using a Fe/Al_2O_3 tunnel contact [65]. They demonstrated spin valve measurements at 10 K and Hanle curves at 5 K, whereas the calculated spin polarization is less than 1%. To be able to observe a spin signal in a NL geometry, it requires small contact areas in a distance smaller than the spin diffusion length. Since the diffusion length in Si is in the micrometer range, the contacts are required to be of the same order of magnitude. This yields

to extremely high junction resistances due to the Schottky barrier formed at the interface, which significantly reduces the obtained signal. Larger contacts and therefore lower junction resistances can be used in the 3T measurement geometry [47, 48]. This was successfully employed and lead to the first observation of a spin accumulation in Si at room temperature in 2009 by Dash et al. [18]. They used a NiFe/Al_2O_3 tunnel contact and obtained a spin polarization of about 5%. More recent, Li *et al.* reported plasma oxidized SiO_2 based devices measuring spin signals up to 500 K, but could not report more than 5% spin polarization at room temperature [66]. The generally observed low spin polarization is explained with the low quality of the TBs, as discussed earlier. Nevertheless, novel fabrication techniques, such as *molecular beam epitaxy* (MBE), promise uniform, high quality TBs. Devices with such a barrier were first realized in 2011 by Jeon et al., but the room temperature spin signal only reveals a spin polarization of 3% [67]. Finally, a recent approach to use graphene as a spin polarizing TB has been presented by van 't Erve et al. in 2013 [68]. They studied a NiFe/graphene/Si junction showing a quasilinear *current-voltage characteristic* (IV) and a low spin polarization of much less than 1% at room temperature.

It has to be mentioned that even though all studies report spin signals in the same order of magnitude, they are about 1000 times higher than calculated by the standard theory for spin transport, which could not yet been completely explained [28]. This discrepancy raised concerns about the contribution of the interface state assisted transport [69, 70], but was ruled out by several control experiments as an origin for the enhancement of the spin signal [71]. Additionally, many studies, comparing 3T and NL measurements, validated the equality of the results of both techniques [72–74].

Despite the efforts of several years of silicon spintronic research, the understanding of the spin injection and transport mechanisms are still limited. Possible pinholes, scattering centres or interface states induced by the TB can be avoided by using a uniform barrier, which has still yet to be found. One alternative could be intrinsically grown silicon oxide, since it has been demonstrated to grow pinhole free[75]. Furthermore, 2D materials, such as graphene[68], functionalized graphene [76] and h-BN [77], were successfully used as spin polarizing and insulating TB on other materials. For a near-future integration into existing Si technology, a highly efficient spin performance and CMOS-compatible processes are desirable. New TB materials and heterostructures with 2D crystals could improve the

spin injection and also allow for novel functionalities.

1.6.2 Graphene

Graphene is made of carbon atoms in a honeycomb lattice structure [78] (see Figure 1.10). It is a 2D half metal with high mobility charge carriers and low light absorption. This makes it interesting for a multitude of applications, such as flexible electronics and to replace rare elements used as transparent conductors, for example in displays [24]. Furthermore, graphene is a band gap free, true 2D system exhibiting a linear dispersion relation around the Dirac point; in contrast, conventional 2D systems have a hyperbolic dispersion relation [79]. This allows to control the charge carrier concentration seamlessly from hole to electron transport by a gate voltage. Moreover, the SO and HF interaction should be negligible and theoretically allows spin lifetimes of nano- or even microseconds [21]. Additionally, the 2D nature provides a confined spin diffusion in lateral dimensions. The metallic character of graphene prevents the creation of a Schottky barrier when contacting with a FM, which avoids additional contact resistances. This electrical tunability of the charge carriers and the theoretical long spin lifetime make it very attractive for spintronics.

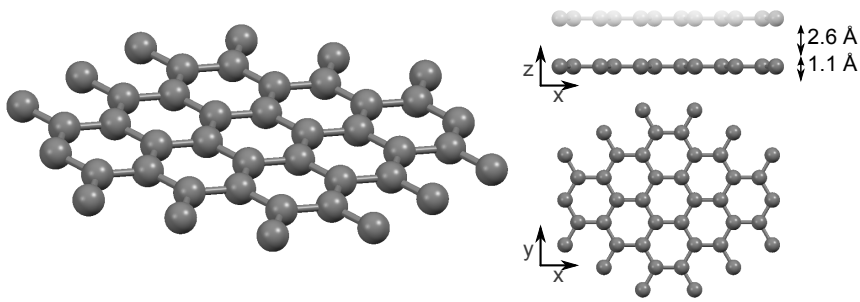

Figure 1.10: Single layer of graphene. The carbon atoms form a flat and homogeneous hexagonal crystal structure. The carbon layers are separated by 3.7 Å and attached by the van der Waals force.

Even though graphene is a rather new material [80], its extraordinary properties allowed rapid advances in spintronic studies. The first demonstration of NL spin transport in graphene at room temperature has been reported in 2007 by Tombros *et al.* using Co/Al_2O_3 tunnel contacts [36]. The obtained spin lifetime was about 130 ps and the injected spin polarization was calculated to be 10%. The discrepancy in spin lifetime compared

to theory has been explained by scattering centres introduced in the graphene due to: 1. dangling bonds and roughness of the used SiO_2 substrate; 2. diffusion of the FM through pinholes in the non-uniform TB [81]; 3. magnetic impurities in the graphene channel [82].

Two different approaches were examined to circumvent the roughness and other substrate induced effect. On the one hand, the graphene can be suspended, which completely removes any substrate effects and increases the mobility significantly [83]. Such devices have been prepared in suspension on polymers [84, 85], but also demonstrated only a spin lifetime of about 150 ps. On the other hand, similar high mobility graphene measurements were reported on atomically flat h-BN [23, 86]. Even though the obtained spin lifetime is 390 ps, the spin diffusion length is only 4.5 μm at room temperature. Nevertheless, Zomer et al. could still obtain a measurable spin signal for electrodes placed $16 - 20\,\mu$m apart [23]. The difference between the low extracted and the larger observed spin diffusion length indicated that the FM contacts affects the spin diffusion significantly. Recent attempts to normalize these contact related effects seemed promising, but had to assume an unaffected intrinsic lifetime, which remains experimentally challenging [87, 88].

Recent experiments using pristine graphene on SiO_2 measuring *universal conductance fluctuation* (UCF) and WL discovered a significant contribution of spin-flip scattering by magnetic moments [82]. A more recent theoretical discussion assumes magnetic moments, created by vacancies or adatoms, acting as resonant scatterers [89]. This theory describes the experimental data well and predicts a spin lifetime of 100 ps for a density of magnetic moments of only 1 ppm. Yet, the origin of the magnetic moments is not completely determined, since all kinds of graphene, substrates and contacts seem to exhibit similar effects limiting the achievable spin lifetime to a few nanoseconds.

This requires a greater insight on the origin of the spin relaxation by separating contact and channel induced effects. A 3T configuration detects the spin accumulation directly under the contact, which can be compared to NL measurements. Additionally, an increasing channel length allows to decrease the contact contribution. These measurements could allow to identify the predominant scattering mechanisms in the graphene channel or the FM contacts. Furthermore, improving the tunnel barrier to reduce pinholes and contact induced scattering centres could also decrease the contact induced effects. An ideal candidate for such a barrier is atomically thin and topologically flat h-BN [77]. Understanding the origin of the spin

scattering mechanisms in graphene is important to develop new techniques to increase the spin lifetime towards the theoretical limit.

1.6.3 Transition metal dichalcogenides

Graphene sparked an enormous interest in the idea of 2D electronics, but previous research also points out its shortcomings. It exhibits a metallic character with high mobility and low scattering rate, which makes it ideal for charge and spin transport. However, pristine graphene has neither a band gap nor SO coupling, which are indispensable requirements for a switching action in charge or spin based transistor applications. External doping to engineer a band gap or to induce a SO coupling in graphene has so far proved detrimental to its intrinsic properties [90].

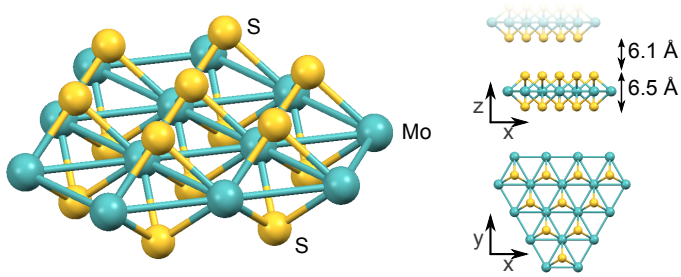

Figure 1.11: Single layer of MoS_2. The triangular sulphur/molybdenum/sulphur layers form a hexagonal structure with alternating corners in the x-y-plane. Such monolayer is about 6.5 Å thick with a distance of 6.1 Å between two layers [91].

Transition metal dichalcogenides are a group of materials, which consist of a transition metal (elements of group III to XII) and two chalcogenide atoms, such as *sulphur* (S), *selenium* (Se) or *tellurium* (Te). Over 40 different compounds can be formed, but only a few of them were demonstrated to be layered. A monolayer of such dichalcogenide is about $6 - 7$ Å thick and formed of a metal layer sandwiched between two chalcogenide layers exhibiting a weak out-of-plane van der Waals force (see Figure 1.11). They exhibit a variety of properties, from metallic and half-metallic [92] to SC [93] and even superconducting [94] transport. Dichalcogenides with *chromium* (Cr), *molybdenum* (Mo), *tungsten* (W), *titanium* (Ti), *tin* (Sn) and *zirconium* (Zr) were predicted to be SC, but so far only Mo and W compounds were successfully isolated in monolayer form and heavily studied [93]. The properties of these SC TMDCs depend also on the number of

layers. For example MoS_2 exhibits a transition from an insulating band gap of 1.2 eV in the bulk material to a direct band gap of 1.9 eV in monolayer MoS_2 [95]. Similar studies demonstrated a direct band gap transition also in $MoSe_2$, WS_2 and WSe_2. The metal and chalcogenide atoms in the unit cell remove the level degeneracy in the k-space. Additionally, the time reversal symmetry enforces split valleys to have opposite spins. This results in a coupling of the spin and valley degree of freedom in the non-degenerate valleys, which can consequently only be switched simultaneously [96, 97]. This coupling has been successfully demonstrated and accessed optically by selectively exciting the valley populations with circular polarized light in monolayer MoS_2 and WSe_2 [97]. The obtained valley spin lifetime was in the range of several nanoseconds, which has also been theoretically verified [98]. This is particularly interesting for spintronic applications, since the coupled spin and valley degree would allow long spin lifetimes in spite of the strong SO interaction. Even more, the strong coupling would allow to manipulate the spins inside the TMDC electrically employing the Rashba effect.

Probing the electrical and spin degrees of freedom of SC TMDCs is possible, since they possess band gaps above 1 eV, which makes them ideal for the development of *field effect transistors* (FET) with small OFF-currents and large switching ratios. So far, single layer MoS_2 FETs with mobilities between $60 - 70\,\mathrm{cm}^2/\mathrm{Vs}$ and ON-OFF ratios spanning $6 - 8$ orders of magnitude have been demonstrated [93, 99, 100]. Recent studies also suggested that a top dielectric or h-BN enhance the carrier mobility up to $250\,\mathrm{cm}^2/\mathrm{Vs}$ [30, 101]. Naturally, SC TMDCs are highly electron doped due to impurities and sulphur vacancies. Unlike graphene, the charge carriers cannot be continuously tuned from electrons to holes with a top or a back gate. Nevertheless, such ambipolar behaviour has been demonstrated with ionic liquid top gates, which create an ultra-high capacitance in the electrical double layer [102]. Furthermore, a mobility increase has also been observed due to enhanced screening. Similar to top dielectrics, different bottom dielectrics and even TMDC layers improve the screening against charged impurities [59, 101, 103]. Especially the latter led to the preferred application of multilayer TMDCs, since they intrinsically exhibit a higher mobility due to the screening by the lower layers and the dominating top layer charge transport caused by the high inter-layer resistance [103, 104]. Nevertheless, the achieved mobilities are about five times lower than theoretically expected [105].

The contact resistance plays a crucial role in the accuracy of the ex-

tracted electric parameters [59]. Commonly used metal contacts to TMDCs exhibit a high Schottky barrier of $100 - 180\,\text{meV}$ depending on the contact material [59]. This is associated with the charge depletion region at the interfaces where only electrons that are thermally emitted over the Schottky barrier can flow across the contact [59, 60]. Even though this region is small in a 2D structure and a quasi-ohmic contact resistance is achieved, few-layer device performance suffers significantly due to the high Schottky barrier. This is in particular relevant for electrical spintronic experiments, where high work function FM are usually used to create spin accumulations within the NM. The resulting conductivity mismatch between the FM and the TMDC could yield a negligible MR [35, 106]. It was successfully demonstrated that the conductivity mismatch issues for spin injection into SCs [18, 107] and graphene [108] can be overcome by employing narrow Schottky barriers or insulating TBs. Recently, a reduction of the Schottky barrier resistance in single-layer MoS_2 was demonstrated by introducing a MgO TB under the FM [60]. Nevertheless, future studies for spintronic applications should focus on achieving a suitable interface resistance and better transistor properties with FM tunnel contacts in single-layer and multi-layer TMDC FETs.

1.6.4 Black phosphorus

The 2D monolayer of BP, called *phosphorene*, is a rather new member of the layered 2D materials and gains increasing interest as a p-doped counterpart of TMDCs. It is the most stable allotrope of phosphorous and the only other known elementary layered material, next to graphene, which exists as a bulk crystal. Its weak inter-layer van der Waals forces can be overcome simply by exfoliation producing monolayers of BP of about 5 Å thickness (see Figure 1.12). The structure of a single layer is buckled with two in-plane, mutually perpendicular directions possessing armchair and zigzag edges [109]. This gives BP a unique structural and electrical anisotropy.

Black phosphorous is synthesized under large pressure of white phosphorous and its bulk properties have been extensively studied for over 100 years [112, 113]. Similar to SC TMDCs it exhibits a significant band gap. In contrast to TMDCs this band gap remains direct and increases with decreasing number of layers, 0.3 eV for bulk BP up to 2 eV in monolayer BP [109, 110]. A variable band gap is not only interesting for applications in electronic logic devices, but also for optoelectronics, since the gap can be tuned within the infrared and near-infrared spectrum. This has been demonstrated in FETs and photo detectors [110, 114–116]. Interestingly,

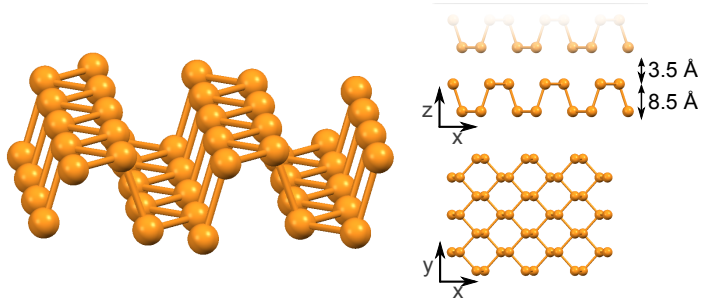

Figure 1.12: Single layer of black phosphorus (phosphorene). The buckled structure has an anisotropy in the electrical and physical properties. Such layer can be exfoliated from bulk crystals and has a thickness of about 8.5 Å and an interlayer distance of 3.5 Å [110, 111].

unlike TMDCs the vacancies of P result in a natural hole doping, but low doping rates allow for a gate-tuned carrier concentration and hence an ambipolar behaviour [117]. Furthermore, BP has a significantly higher mobility than TMDCs with $286\,\mathrm{cm}^2\,(\mathrm{Vs})^{-1}$ in single layer [110] up to about $1000\,\mathrm{cm}^2\,(\mathrm{Vs})^{-1}$ in 10 nm thick films [114]. Nevertheless, BP exhibits a high Schottky barrier of about 200 meV for the hole carriers [110], which can significantly affect the charge and spin transport properties. This Schottky barrier creates similar contact problems as in TMDCs, which so far has not been systematically addressed.

The spin-related attributes of BP are also unique compared to other 2D crystals. The low atomic mass of P yields a lower SO coupling compared to TMDCs. Combined with the high mobility this is promising for a long spin transport length, despite the missing preservation of the spin due to a valley splitting, as in TMDCs. Additionally, the nuclear spin of $+\frac{1}{2}$ of the phosphorous atom makes BP an excellent platform to intrinsically investigate nuclear HF interactions [118] and dynamical nuclear spin polarization effects [119].

Even though the research of BP as a layered material is only in its very beginning, previous studies provide a promising outlook by demonstrating its unique anisotropic structural, electrical and spintronical properties. Combined with the experimental experience of studying 2D materials in the last decade, the ongoing research tries to access these properties. An optimization of the contacts properties is a primary requirement, especially for electrical measurements. This has not yet been investigated, in particular for the FM tunnel contacts of spintronic devices.

1.6.5 Topological insulators

Topological insulators form an entirely new class of 2D materials. The term "topological" originates from the fact that the wave functions describing their electronic states span a Hilbert space with a non-trivial topology. In such a material the momentum vector k becomes a good quantum number mapping the $k-$space into the Hilbert space linking the topology and the electronic states of the system [120]. The physically consequence for such an insulator is the appearance of a gapless interface state on the boundary to a normal insulator (including the vacuum). Practically this was first observed in high mobility SCs in large magnetic fields yielding the quantum Hall effect [121]. In such quantum Hall systems the localized electrons and their Landau quantization result in a vanishing conductance along the current direction whilst the Hall conductance is a quantized multiple of $\frac{e^2}{h}$ when the potential is in between two Landau levels. It has been shown that an gapless state remains at the interface, even though the chemical potential lies in a "bulk" band gap [122]. Since such a system would have great advantages for spintronics [123] many proposals were made to create a material which exhibits these properties intrinsically without an external magnetic field [124–126]. The model presented by Kane and Mele [126] is based on graphene with a strong SO coupling and illustrates the principle of a 2D TI. They demonstrated that a finite SO coupling opens a gap in the Dirac point having a time-reversed pair of spin-polarized 1D states at the edges. The strong SO coupling aligns the spins in relation to their momentum direction creating a spin polarization of the edge states. This non-degenerate spin state is often referred to as *helical spin polarization* or *spin-momentum locking* (SML). Additionally, the electrons in the edge states behave as 1D massless Dirac fermions within the gap of the 2D Dirac cone. Even though an experimental realization is difficult, due to the low SO coupling of graphene, similar systems were subsequently proposed [127] in HgTe/CdTe quantum wells and also experimentally confirmed [128]. Meanwhile, theorist already extended the initial idea of 2D TIs and predicted similar properties in the new class of 3D TIs [129].

Three-dimensional TIs exhibit similar properties to their 2D counterparts. So far, several materials have been successfully predicted by theory and experimentally verified. The main requirements are, identical to 2D TIs, a bulk band gap and a band inversion at the interface, usually caused by a strong SO interaction, yielding 2D surface states. Therefore, it is not surprising that the majority of studied 3D TIs are compounds consisting of heavy transition metals like *bismuth* (Bi) or *antimony* (Sb) layers with chal-

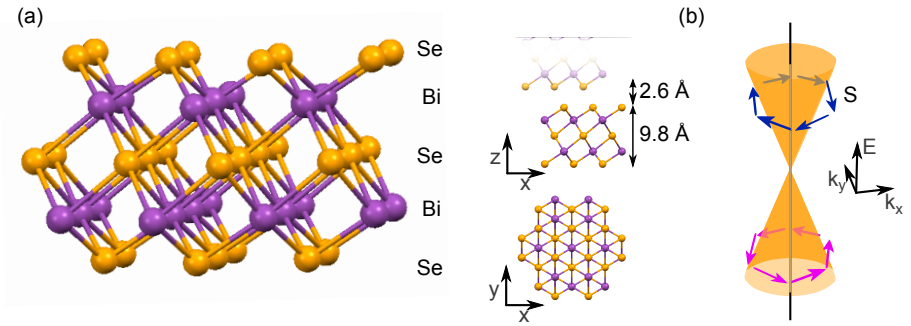

Figure 1.13: Three-dimensional topological insulator (3D TI) crystal structure and helical spin states. (a) Bi_2Se_3 crystal exhibiting the for 3D TIs typical quintuple structure. Such single layer is about 1 nm thick and the interlayer distance is about 2.6 Å. (b) A Dirac cone is formed at the surface, which exhibits a locking of the spin $\vec{S}$ to its momentum vector $\vec{k}$.

cogenide interlayers. Generally these can be written as $Bi_{2-x}Sb_xTe_{3-y}Se_y$, whereof Bi_2Se_3, Bi_2Te_3 and Sb_2Te_3 are 3D TIs, but Sb_2Se_3 is not. The crystal structure is made of sheets of quintuple layers in a alternating chalcogenide/transition metal stacking. An example is given for Bi_2Se_3 in Figure 1.13a. The difference in band structures made Bi_2Se_3 the prototypical TI, since it exhibits a clear band gap with a centred Dirac cone in the surface states. Nevertheless, these compounds exhibit heavy electron doping due to natural formed Se or Te vacancies shifting the Fermi level into the conduction band and making the bulk material conducting, which hinders the electrical detection of the surface states. Very recently, complex mixtures, such as $Bi_{1.5}Sb_{0.5}Te_{1.7}Se_{1.3}$ [130, 131] and $BiSbTeSe_2$ [132], were demonstrated to show no intrinsic doping.

Initial studies on 3D TIs used photo-electron spectroscopic techniques to study their extraordinary band structure. Such measurements have the advantage to be able to probe only the surface states, independent of the Fermi energy and hence the intrinsic doping. Using *angular resolved photoemission spectroscopy* (ARPES) the closed band gap and the Dirac cone at the boundary could be demonstrated up to room temperature [133]. The helical spin states could be detected using a spin-resolved ARPES [134], which clearly demonstrated the perpendicular locking of the spin to its momentum (Figure 1.13b).

However, accessing the spin polarizations in 3D TIs is a crucial step towards spintronic applications. This remains challenging since undesired

doping and low bulk band gaps in 3D TIs usually create a parallel unpolarized conduction channel. So far, dynamical methods were employed to couple the TSS to FM contacts creating a spin transfer torque [135] or for spin injection [136, 137]. Only recently, potentiometric measurements have been used to detect spin-polarized surface currents in 3D TIs probed by a FM contact [31, 138–140], which acts as an efficient detector even in presence of unpolarized bulk charge currents [50]. However, so far the direct electrical detection of a current-induced spin polarization in 3D TIs has been restricted to temperatures below 125 K [31, 138–140], which limits further progress in this research field and its application potentials. The room temperature electrical detection of such highly correlated spin systems is not only interesting for fundamental research but also for applications in dissipationless quantum spintronic devices [54, 141].

1.6.6 Hexagonal Boron nitride

Hexagonal boron nitride is a layered insulator with a large band gap of almost 6 eV [142]. It is the most stable and softest polymorph of boron nitride, which makes it industrial relevant as lubricant and in ceramics for high temperature and chemically aggressive applications [143]. Hexagonal boron nitride is an isoelectronic structure to graphene and exhibits similar inter-layer distances and a lattice mismatch of 1.7% between h-BN and graphene [86, 142, 144].

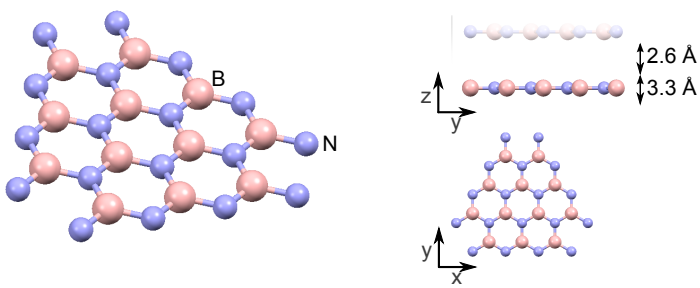

Figure 1.14: Crystal structure of hexagonal boron nitride. Boron and nitrogen atoms form a flat and homogeneous hexagonal structure with similar lattice constants as graphene [142].

Recently, h-BN has been discovered for its potential in nano devices. Its layered structure allows a simple fabrication of mono- or few-layers by exfoliation technique, but it can also be controllably grown by bottom-up

techniques, such as CVD. Its large band gap and topologically flat surface with a low density of scattering centres for charge carriers makes it an ideal candidate as insulator in heterostructures with other 2D materials [25, 86, 145]. In particular, h-BN has been proposed and employed as an inert substrate for graphene, which demonstrated record carrier mobilities [86]. It has also been used to encapsulate graphene and other 2D materials to provide a dangling bond free and insulating environment devoid of adatoms [25, 146–148].

The demonstration of improved electrical properties of graphene [86], combined with the insulating properties, make h-BN also an interesting candidate for spintronic applications. It has been demonstrated that graphene on a h-BN substrate exhibits highly improved spin parameters. Spin lifetimes of several nanoseconds and spin diffusion length of up to $10\,\mu$m were demonstrated in graphene channels up to $16\,\mu$m long [23, 149, 150]. Furthermore, its atomically thin and inert nature makes it an ideal candidate as a 2D TB. Recent studies showed the good tunnelling properties of h-BN [77, 151]. Additionally, it has been theoretically proposed that h-BN exhibits a large tunnel spin polarization up to 100% [29]. This is highly motivating for further research, in particular since both graphene and h-BN are electrically complimentary and can be fabricated on a large scale by CVD growth, either individual or combined [152, 153]. Improved fabrication processes could allow for even higher spin parameters in graphene and to approach the true spin tunnelling potential of h-BN.

2

Spin injection into silicon

Developing methods for efficient injection, controlled manipulation, and sensitive detection of electron spins in the industrial relevant *semiconductor* (SC) silicon has the potential to profoundly affecting information technology. So far, optical measurement techniques revealed a spin polarization in the Si bulk of 30% [11], whereas electrical methods only achieved 5% [18]. Such low values of the spin polarization stems from the lack of high-quality *tunnel barriers* (TB) on Si, which limits the spin injection and detection. It is crucial to understand the spin injection and detection mechanisms and to achieve a spin polarization in Si close to the *tunnel spin polarization* (TSP) values of the *ferromagnetic* (FM) contact. Commonly used metal oxide TBs, such as Al_2O_3 and MgO, grow non-uniformly and react with the Si substrate, which leads to pinholes and localized states in the junction [18, 28, 154]. Pinholes yield a reduction of the efficiency of the spin injection and detection. Localized states can result in an enhancement of the spin accumulation or a sign reversal, which is not completely understood yet. Additionally, the Schottky barrier formed at the interface between Si and the FM tunnel contact can highly affect the injection mechanism by promoting different transport processes.

Here we demonstrate the creation of large spin polarizations in n-type and p-type Si, using an ozone oxidized SiO_2 TB. Furthermore we address the role of the Schottky barrier profile in Si due to the change in transport

processes across the interface from direct to indirect tunnelling (Paper I). Subsequently, we explore *hexagonal boron nitride* (h-BN) TBs for spin polarized tunnelling, which is promising due to atomically thin, crystalline and flat structures without dangling bonds and interface states (Paper II).

2.1 Large spin accumulations in silicon

For efficient spin injection into Si, the growth of high quality TBs with better interfaces is desirable. Thin metal oxide TBs exhibit an increased interface state density [155], whereas SiO_2 exhibits a defect density up to several orders of magnitude smaller [156]. It has been proposed that the spin polarized carriers can be trapped in these states and are responsible for observed enhancement in spin signals and its large temperature dependence. [18, 28]. The high concentration of interface states and the ensuing enhancement in spin signal can be reduced for Si by using SiO_2 barriers, since it can be grown more uniform and pinhole free on Si compared to metal oxide barriers.

In this section we focus on SiO_2/Co contacts fabricated on highly doped Si, which results in a very thin Schottky barrier at the FM/Si interface and hence a dominating transport through the introduced TB (Figure 2.2a). The SiO_2 TB was fabricated by UV ozone oxidation as described in Section A.2.1 resulting in about $1-2\,\mathrm{nm}$ of SiO_2 layer. Subsequent *current-voltage characteristic* (IV) measurements reveal a non-linear and symmetric characteristic confirming a tunnelling behaviour (Figure A.1a). Furthermore, we obtained a resistance area product $R_cA \approx 2\,\Omega\mathrm{mm}^2$ of the junction at room temperature. This value changes only by a factor of two when cooling down to $5\,\mathrm{K}$, which indicates a uniform and pinhole free TB.

Next, we evaluated the spin injection performance by studying the Hanle signal in a *three-terminal* (3T) contact configuration (Section 1.4.3) on highly degenerate electron doped Si (n++ Si) with a ozone oxidized SiO_2 TB. Figure 2.1 shows the large Hanle signal of $3\,\mathrm{mV}$ and its bias dependence in the voltage range from $-0.5\,\mathrm{V}$ to $1\,\mathrm{V}$. For spin injection ($V_{Si} - V_{FM} > 0$) the signal increase with bias voltage is larger than for spin extraction ($V_{Si} - V_{FM} < 0$). Such a behaviour has been observed in several studies on Si, Ge and GaAs [18, 157, 158]. Considering a TB spin polarization (TSP) of 35% and employing Equations (1.24) and (1.34) we can derive the spin potential splitting $\Delta\mu$ and the spin polarization P at the interface. For n++ Si the bias dependence shows a maximum spin signal at $1\,\mathrm{V}$ with $\Delta V = 3\,\mathrm{mV}$, which equals a polarization of 34% in the

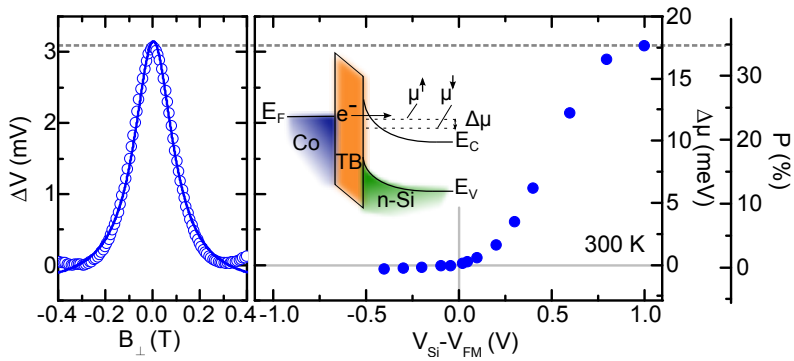

Figure 2.1: Large spin signal measured at room temperature in a sample with UV ozone oxidized SiO_2 on highly doped n-type Si. The left panel shows a Hanle signal with an applied bias voltage of 1 V. The right panel shows the bias voltage dependence in a range of −0.5 V to 1 V. The axis on the far right show the according spin potential splitting $\Delta\mu$ and the resulting spin polarization in the material.

Si conduction band at room temperature. This is a significant improvement compared to previous electrical studies, which only measured a spin polarization up to 5% at room temperature [18, 66, 67].

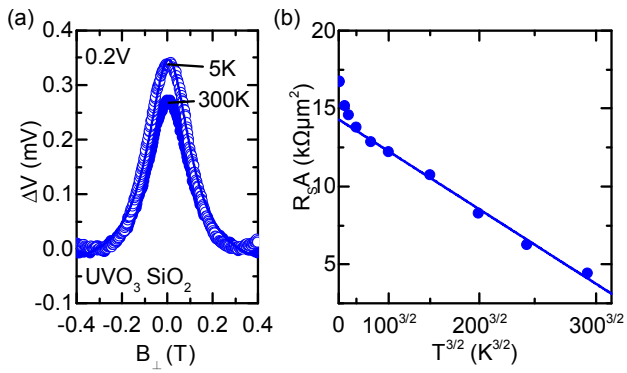

Figure 2.2: Temperature dependence of spin signal in highly doped n-type Si. (a) Hanle signals obtained for spin injection through a Co/SiO_2/n-Si at a bias voltage of 200 mV and temperatures of 5 K and 300 K. (b) Temperature dependence of the spin signal amplitude at a bias voltage of 200 mV in a temperature range of $5 - 300$ K.

Additionally, the spin signal show a very weak temperature dependence, increasing only by 30% when cooling down from room temperature. The obtained Hanle curves measured in a n-Si/SiO_2/Co contact at temperatures of 5 K and 300 K and a bias voltage of 200 mV are shown in Figure 2.2a. The spin resistance area product R_SA exhibits a weak tem-

perature dependence (Figure 2.2b), which can be fitted by the theoretical model $R_S A \propto 1 - \alpha T^{\frac{3}{2}}$ for FM tunnel junctions in the direct tunnelling regime [159]. This confirms that the spin accumulation is actually created and detected in the bulk Si band over the full temperature range. In contrast, Al_2O_3 and MgO TBs exhibit a pronounced enhancement of the $R_S A$ at low temperatures [18, 67]. Additionally, spin lifetimes are found to be independent of both temperature and bias voltage (see Figure 2c and 3c in Paper I), which also indicates a spin accumulation in the Si band. Even though the obtained spin signal with a SiO_2 barrier is orders of magnitude larger than expected [28], they are comparable to results on other TBs at room temperature. Furthermore, the weak temperature dependence indicates no additional enhancement of the spin signal at low temperatures and shows that SiO_2 is generally better suited as a TB than metal oxide barriers for spin injection into Si. It has to be mentioned that the lower limit for the spin lifetime is found to be $\tau = 50\,\text{ps}$ yielding a spin diffusion length of $\lambda = 80\,\text{nm}$. Even though these values are similar to those from previous reports on degenerate Si [18, 67], the limitations of the spin lifetime are not yet fully understood [160].

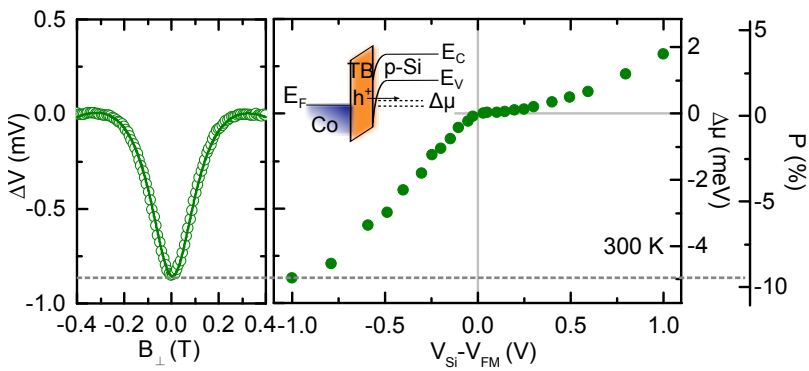

Figure 2.3: Large spin signal measured at room temperature in a sample with UV ozone oxidized SiO_2 on highly doped p-type Si. The left panel shows a Hanle signal with an applied bias voltage of $-1\,\text{V}$. The right panel shows the bias voltage dependence in a range of $-1\,\text{V}$ to $1\,\text{V}$. The axis on the far right show the according spin potential splitting $\Delta\mu$ and the resulting spin polarization in the material.

Similar results could be obtained using a highly degenerate hole doped Si (p++ Si) substrate (Figure 2.3). Since the charge is carried by holes, the spin accumulation occurs in the valence band. That means, in contrast to the bias dependence for n-type Si, a positive bias voltage ($V_{Si} - V_{FM} > 0$)

extracts hole spins creating a minority (hole) spin accumulation. Accordingly, a negative bias voltage ($V_{Si} - V_{FM} < 0$) injects hole spins creating a majority (hole) accumulation. This results in a non-symmetrical bias dependence, where the efficiency for spin injection is higher than for extraction; identical to n-type Si. At a bias voltage of $-1\,\mathrm{V}$ a spin signal of $\Delta V = -0.8\,\mathrm{V}$ was extracted yielding a spin polarization of 9%. Even though the polarization is about one third of the one observed in n-type Si, it is still twice as high as previous reported results.

These results demonstrate that SiO_2 oxidized by ozone is an excellent spin polarizing, low resistive TB perfectly suited for spin injection and detection into highly doped n- and p-type Si. On one hand, these experiments with highly doped Si exhibit a greatly reduced Schottky barrier width. In contrast, by using low doped Si the Schottky barrier width increases and introduces a non-negligible additional resistance. This can affect the spin tunnelling process and is therefore of great interest to study (see Section 2.2). On the other hand, novel TB materials with active spin filtering properties are highly interesting, since they could yield an even higher spin polarization in the bulk SC (see Section 2.3).

2.2 Role of the Schottky barrier

A Schottky barrier emerges for electrical contacts through heterojunctions, such as metal/SC junctions. Due to different work functions in the involved materials, a bending of the conduction and valence band occurs [161], which yields the formation of a barrier at the interface. Such a Schottky barrier results in a carrier depletion at the SC surface, which allows different spin-transport processes, depending on the profile of the Schottky barrier [162, 163]. It has been proposed that for degenerate SC a very narrow Schottky barrier would allow direct spin-polarized tunnelling, whereas in non-degenerate SC the presence of a wider Schottky barrier would be expected to change the transport mechanism [162].

In Si the Schottky barrier width can be increased by decreasing the dopant concentration (Figure 2.4a and 2.4b). The highly doped Si, presented in the previous section, exhibits a thin Schottky barrier yielding a higher TB resistance dominating the spin tunnel processes. By decreasing the doping concentration, this contribution can be reversed, that means the Schottky barrier resistance can become much larger than the tunnel resistance. So far, no systematic study on the role of the Schottky barrier on the spin injection and extraction has been presented.

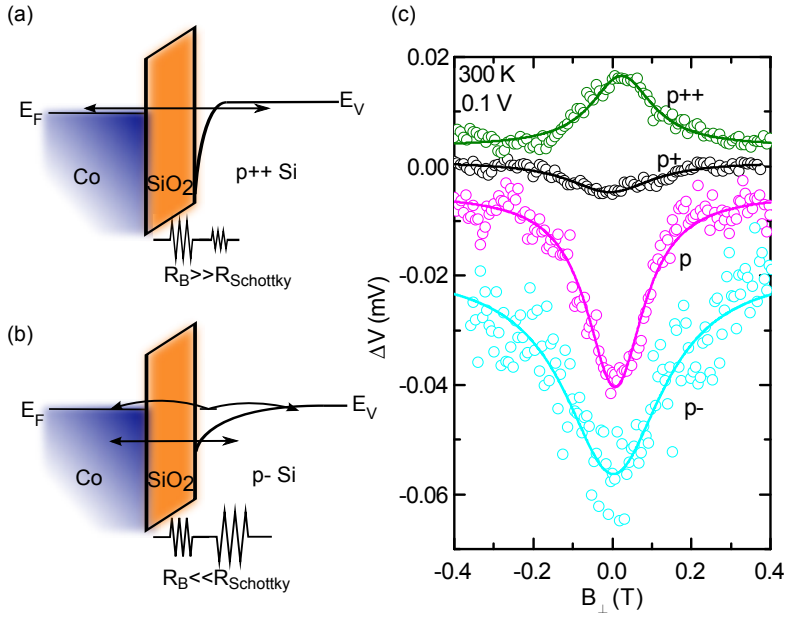

Figure 2.4: Spin injection mechanisms with Schottky barrier profile and resulting Hanle signals. (a) Band structure for highly doped p-type Si. The Schottky barrier width and therefore resistance is low. That means the TB resistance is significant larger and direct tunnelling dominates. (b) Band structure for low doped p-type Si. The Schottky barrier is large and dominates the tunnel resistance. Two-step and direct tunnelling occur. (c) Hanle signals measured at a temperature of 300 K and 100 mV of bias voltage for all four doping concentrations plotted with a shift along the y-axis. A change in the sign of the spin signal can be observed, increasing with decreasing doping concentration.

Here we present a systematic study on p-type Si in four different doping concentrations: p++ ($1.8 \cdot 10^{19}\,\mathrm{cm}^{-3}$), p+ ($1.5 \cdot 10^{19}\,\mathrm{cm}^{-3}$), p ($5.4 \cdot 10^{18}\,\mathrm{cm}^{-3}$) and p- Si ($1.3 \cdot 10^{15}\,\mathrm{cm}^{-3}$)[1]. The FM contacts were prepared as explained in section A.3.1. Initial IV measurements were performed to characterize the tunnel junctions (see Figure 4b in *Paper I*). They show that the junction resistance increases drastically with decreased doping concentration. Furthermore, the transition of the IV characteristic from a tunnelling behaviour towards a diode behaviour can be observed with a decrease in the doping concentration. This shows, that for a decreasing doping concentration the Schottky barrier resistance becomes more dominating over the TB resistance.

Subsequently, the Hanle effect was employed to study the spin injection

[1]Further parameters of the Si can be found in Table 1 in Paper I.

and detection into the Si. Figure 2.4c shows a comparison of Hanle signals measured in all four differently doped p-type Si samples at a temperature of 300 K and a bias voltage of 100 mV. Even though the applied bias voltage should result in a spin extraction signal (positive sign), a significant sign change can be observed for substrates with a lower doping. Moreover, the sign magnitude increases with decreasing doping concentration. The full bias dependence of the spin signals, including both injection and extraction regime, for all four samples is shown in Figure 2.5.

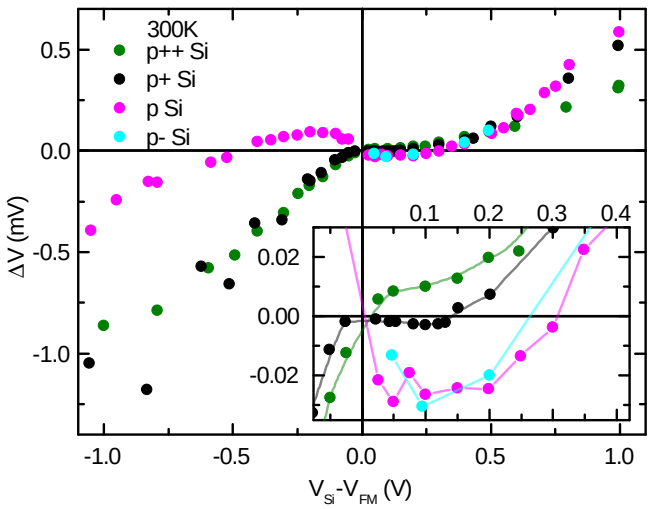

Figure 2.5: Bias dependence of spin signal with tailored Schottky barrier. Four different boron doping concentrations in p-type Si are studied. The degenerate p++ Si device shows normal Hanle signal behaviour, whereas the non-degenerate devices (p+, p and p- Si) show anomalous sign reversal. The inset shows the low bias regime, in order to emphasize the sign reversal of the spin signals.

The bias dependence of the degenerate p++ Si sample is the same as shown in Figure 2.1b. Analysing the bias dependence of the lower doped, non-degenerated Si samples, a sign change can be observed in the low bias regime. For the p+ Si sample this sign change is small and only observable for spin extraction with bias voltages up to 150 mV (see inset in Figure 2.5). The lower doped p Si exhibits a sign reversal in both the injection and extraction regime up to −500 mV and 400 mV, respectively. Finally, the lowest doping (p- Si) shows a similar sign reversal behaviour in the spin extraction regime, whereas a significantly increase of the resistance in reverse bias decreases the signal-to-noise ratio and prevents the observation

of the spin signal in the spin injection regime.

A sign reversal within the injection or extraction regime is unusual, but has also been reported in other studies on GaAs, Ge and Si [107, 164, 165]. The sign inversion indicates the accumulation of the opposite spin polarization in the Si. Our experiments systematically show that larger Schottky barrier resistances induce and enhance the sign inversion of the spin signal. This means the anomalous spin-signal signs in different bias regimes are due to competing transport processes across the Schottky barrier [166]. There are three main transport processes contributing to the different regimes: 1. At low Schottky barrier resistance (degenerate Si), or at high bias voltages, direct tunnelling dominates, yielding a normal sign for the Hanle signal (Figure 2.4a). 2. Resonant tunnelling via localized states at the interface occurs for higher Schottky barrier resistances and competes with direct tunnelling. At lower bias voltages, the escape times for spin-up and spin-down electrons from the localized states increases with Schottky barrier width. Different escape times for both spins can give rise to an inversion of the spin signal (Figure 2.4b) [163]. 3. The tunnelling between the FM and the localized states is dominant when the Schottky barrier resistance is very high, or when the applied bias voltage is low. Acceptor and donor states of paramagnetic centres on the interfaces may be responsible for the spin-reversal behaviour.

This indicates that Schottky barrier resistances above a critical limit result in an anomalous sign reversal in the spin signal in the lower bias voltage regime, due to the domination of two-step tunnelling and thermionic spin transport across the interface. Additionally, the paramagnetic centres near the interface may play a major role in creating this anomalous spin-reversal behaviour. These results encourage further investigation to understand the effects of localized interface states and trivalent Si defects on the spin signal.

2.3 Hexagonal boron nitride tunnel barrier for spin polarized tunnelling

Spin injection experiments on Si focused primarily on FM contacts with insulating oxide layers of Al_2O_3, MgO or polycrystalline SiO_2, which can introduce inter-diffusion, roughness, defects and trapped charges on Si. This results in additional spin relaxation due to interface traps and surface/impurity scattering , as well as spin precession in stray magnetic fields near a rough FM interface [158]. Therefore, it is crucial to fabricate atom-

ically smooth, insulating and crystalline spin TBs, a prime building block in determining the future course of silicon spintronics [28].

The discovery of *two-dimensional* (2D) atomic crystals has opened up the possibility of employing their fascinating multifunctional properties. Hexagonal boron nitride is a layered insulator with a large band gap of almost 6 eV and an topologically flat surface without dangling bonds, which makes it highly interesting as an alternative TB material. Recent studies demonstrated the excellent tunnelling properties of h-BN [77, 151], which encourages the investigation of its spin dependent tunnelling properties. Theoretical calculations predict a TSP of up to 100% using h-BN tunnel junctions [29]. This would allow to create spin polarizations in the NM far above the intrinsic FM polarization without any interface related side effects. In order to establish the potential of atomically thin h-BN TBs, it is crucial to first demonstrate its tunnel spin transport and spin injection into Si, which has not been realized so far.

Initially, we investigated h-BN in *magnetic tunnel junctions* (MTJ), which are technologically highly interesting and an ideal tool to study the spin tunnel properties of the junction and hence the barrier material. Therefore, we investigate MTJs made of a h-BN layer in between two FM electrodes. The principle of a MTJ is described in Section 1.1, in which different switching fields of the FM electrodes can be achieved by varying their width (Co/h-BN/Co) or employing different materials with individual coercive fields (NiFe/h-BN/Co). The fabrication of such MTJs using h-BN grown by *chemical vapour deposition* (CVD) is described in Section A.3.2.

A typical resistance switching at room temperature when sweeping an in-plane magnetic field is shown in Figure 2.6a. A fixed current is applied through the MTJ, whilst the voltage drop across the junction is detected non-locally (see inset of Figure 2.6a). Calculating the resistance for the parallel and anti-parallel magnetization orientation allows to extract a *tunnel magnetoresistance* (TMR) with Equation (1.4) of about 0.15%. This equals a spin polarization of 2.7% assuming a similar polarization in the Co/h-BN and NiFe/h-BN junction. For the Co/h-BN/Co MTJ we can extract a TMR of 0.35% and a respective spin polarization at the Co/h-BN junction of 5%. The low polarization could stem from oxidation or impurities at the interface of the first FM, since it had to be exposed to atmosphere before the transfer process of the h-BN. Nevertheless, the clear switching of the TMR indicates a decoupling of the two FM electrodes by the h-BN TB. Furthermore, the TMR decreases with increasing bias voltage (Figure 2.6b), which distincts the TMR from the anisotropic MR caused by

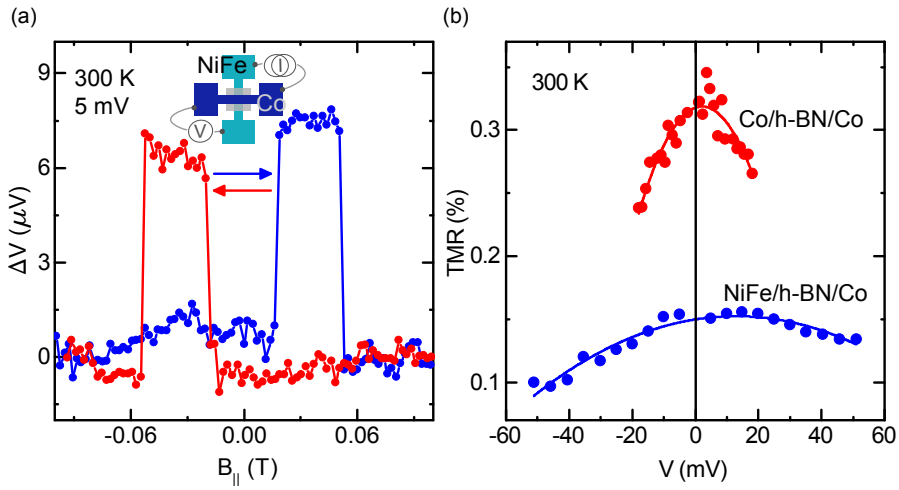

Figure 2.6: Tunnel magnetoresistance measurement using a h-BN barrier. (a) Potential switching during in-plane magnetic field sweep at room temperature with a bias voltage of 5 mV for a NiFe/h-BN/Co magnetic tunnel junction (inset). (b) Bias voltage dependence of the TMR for NiFe/h-BN/Co and Co/h-BN/Co devices.

FM coupling [7, 167, 168]. This clearly demonstrates that atomically thin large area CVD grown h-BN TBs are generic for spin tunnelling in a large class of devices. Hexagonal boron nitride TBs are particularly interesting for efficient spin injection into graphene (see Section 3.3) and silicon.

Replacing the bottom electrode with a NM material, such as silicon or graphene, can also avoid the unwanted oxidation of the FM before the h-BN transfer and provide correct spin polarization values of FM/h-BN contacts. For spin injection into Si we fabricated Co/h-BN/Si tunnel contacts on highly degenerate doped Si (n++ Si and p++ Si), similar as described in Section A.3.1, whereas the exposed Si surface was covered by a layer of CVD h-BN instead of ozone oxidized. Subsequent IV measurements at room temperature reveal a contact resistance of $R_cA \approx 2\,\Omega\text{mm}^2$ and a non-linear IV characteristic.

Next, we performed Hanle measurements in a 3T contact configuration (see Section 1.4.3) on the Co/h-BN/Si devices. Figure 2.7a shows Hanle signals obtained at ±300 mV at a temperature of 100 K. We observe a spin lifetime of around 38 ps, which is comparable to the one in our $Co/SiO_2/Si$ devices. Furthermore, the spin signal amplitude exhibits a strong temperature dependence and could be observed up to 250 K (Figure 2.7b). The extracted spin polarization created in the Si bulk band varies from 1-5%,

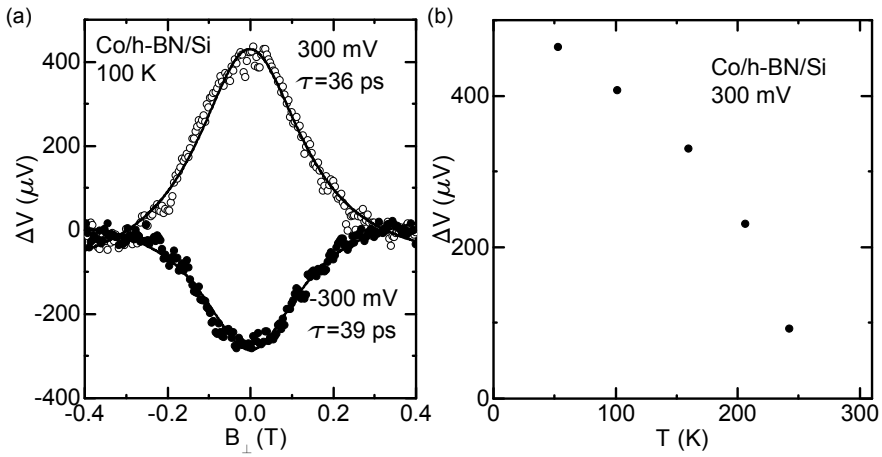

Figure 2.7: Hanle signal and temperature dependence for Co/h-BN/n-Si device. (a) Hanle signal measured at 100 K with a bias voltage of ±300 mV. The extracted spin lifetime is about 40 ps. (b) Temperature dependence of the spin signal amplitude measured at a bias voltage of 300 mV.

which matches well with metal oxide TB devices on Si [18, 67].

This study shows that h-BN can be used as spin TB on Si. Nevertheless, the employed CVD h-BN exhibits grains of a few micrometers, which is very likely to create pinholes in the h-BN/Si interface, in particular on junctions with a contact area above $100 \times 100\,\mu m^2$, as used in our study. Additionally, the bottom contact of the MTJ structure and the contact mesa of the Si devices represent large aspect ratios, which have to be covered by the h-BN and could also induce strain or pinholes affecting the spin transport. These problems stem mainly from the process design and could be avoided by decreasing the contact size and aspect ratio of the devices. In order to exploit the full spintronic potential of h-BN it can be combined with other atomically flat and thin 2D crystals, such as graphene presented in Section 3.3.

3

Spin injection and transport in graphene

Graphene exhibits extraordinary electrical, optical and mechanical properties, which made it an extensively studied material in many scientific fields [78, 80, 169]. Its tunable charge carrier concentration, high mobility and low *spin-orbit* (SO) and *hyperfine* (HF) interaction also make it an ideal candidate for long distance spin transport. Since the first observation of spin transport at room temperature [36] many studies reported significantly lower spin lifetimes and diffusion length than theoretically predicted [21]. These spin transport studies indicate contact and channel induced spin scattering as possible origins of the low spin parameters.

In this chapter we address these problems by investigating the influence of *ferromagnetic* (FM) contacts, the graphene channel length and *hexagonal boron nitride* (h-BN) tunnel barrier on the spin parameters. We employ both *three-terminal* (3T) and *non-local* (NL) techniques to distinguish the spin parameters under the contacts and in the channels, respectively. Measurements with various FM tunnel contacts and graphene channel lengths clearly demonstrate the effect of the contacts on the spin parameters (Paper III). These studies improve the understanding of the spin transport and relaxation in graphene and demonstrate a very long distance spin transport with long spin lifetime and spin diffusion length in *chemical vapour deposited* (CVD) graphene on a SiO_2 substrate (Paper IV). Furthermore, we replace the conventionally used metal oxide tunnel barrier by atomically

thin *two-dimensional* (2D) h-BN and investigate its spin tunnelling properties, which demonstrates spin filtering effects with a large negative spin polarization (Paper V and Paper VI).

3.1 Ferromagnetic contacts on graphene

Ferromagnetic contacts are generally used for the electrical injection and detection of spin polarizations in graphene. Even though, graphene exhibits a gap-free band structure, its intrinsic resistance is still higher than for most metals, especially FM. This yields a conductivity mismatch, which can be resolved by introducing a tunnel barrier (see Chapter 1). Here we study the effects of the tunnel barrier on the spin parameters in graphene by studying various FM tunnel contacts in the 3T and NL measurement geometry.

3.1.1 Ferromagnet/graphene direct contact

Measurements without a tunnel barrier are still possible and such direct contacts are an excellent reference for devices with a tunnel barrier. Therefore, we initially studied contacts without a tunnel barrier (transparent barrier) on graphene, which were fabricated on exfoliated few-layer graphene as described in Section A.3.3.

Measuring the *current-voltage characteristic* (IV) in a 3T configuration enables to extract the resistance of the Co/graphene junction. The IV characteristic shows an ohmic characteristic with a resistance area product of $R_cA = 65\,\Omega\mu\text{m}^2$. Such low resistance was expected for a barrier free contact of a FM to graphene.

The NL spin valve technique enables to detect the electrochemical potential for up- or down-spins under the detector electrode. This was theoretically described in Section 1.4.2, where the measured voltage difference V_{NL} is given by Equation (1.26). Experimentally, the spin accumulation can be estimated by measuring the potential difference between up- and down-spins. This can be done by detecting the voltage for parallel and anti-parallel injector and detector magnetization configuration, which yields $2V_{NL} = V_{\uparrow\uparrow} - V_{\uparrow\downarrow}$[1]. This can be achieved, by altering the FM magnetization independently by an external in-plane magnetic field.

A FM with a high aspect ratio aligns its magnetization along the easy axis. A finite magnetic field anti-parallel to this direction is necessary to inverse the magnetization. This switching field (coercive field) depends also

[1] $V_{\uparrow\uparrow}$ is the positive sign in Equation (1.26), whereas $V_{\uparrow\downarrow}$ is negative.

on the aspect ratio and decreases with increasing FM width. Therefore, FMs in a NL geometry usually require different widths for injector and detector contact which enables them to have distinct switching fields (see Figure 1.6a).

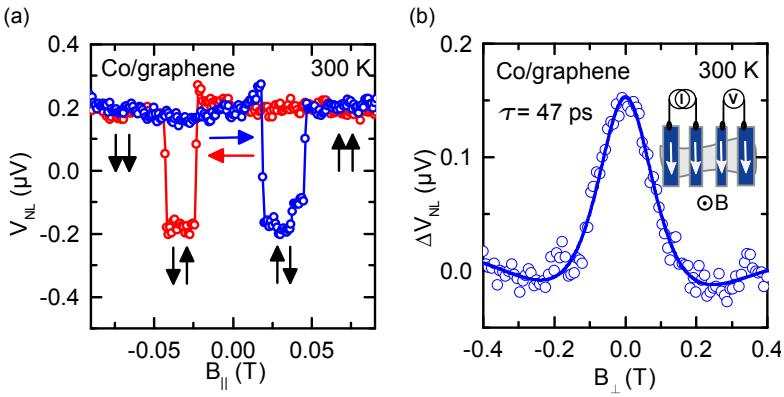

Figure 3.1: Non-local (NL) measurements of spin transport and precession in graphene using a direct Co contact at room temperature with an applied bias current of 10 μA. (a) NL spin valve measurement with in-plane magnetic field. The width of the Co electrodes are 400 nm for the injector and 130 nm for the detector with a graphene channel distance of 2 μm. The signal equals a magnetoresistance of 40 mΩ. (b) NL Hanle measurement in the same contact configuration, but with applied perpendicular magnetic field (measurement setup shown in the inset). The extracted spin lifetime is about 47 ps.

A typical NL spin valve measurement, obtained in a direct Co contact on graphene at 300 K and 10 μA of bias current, is presented in Figure 3.1a. The obtained signal amplitude of $2\Delta V_{NL} = 0.4\,\mu$V corresponding to a NL magnetoresistance $MR_{NL} = \frac{\Delta V}{I} = 40\,\text{m}\Omega$ with a weak temperature dependence. These NL spin-valve measurements confirm the spin injection, transport and detection in the graphene with a direct Co contact up to room temperature. Equation (1.26) describes the spin valve signal theoretically, but requires either the spin polarization at the interface (γ) or the spin diffusion length in the graphene (λ_{NM}) for further analysis.

For extracting the spin diffusion constant, spin diffusion length, spin lifetime and polarization the Hanle precessional dephasing described in Section 1.4.2 was used. The spin precession induced by a perpendicular magnetic field yields a field dependent voltage signal. Such measured data are presented in Figure 3.1b, where the line represents a fitting to Equation (1.31). For the transparent tunnel contact, measured at a temperature of 300 K and 10 μA of bias current, a spin lifetime of $\tau = 47$ ps, a polariz-

ation $P = 5\%$ and a diffusion constant $D = 0.008\,{}^{m^2}/_{\mathrm{s}}$ has been extracted. The obtained spin lifetime is much lower than the theoretical expectation of almost one microsecond [21]. A possible explanation can be given considering the direct FM contact on graphene. The complete absence of the tunnel barrier allows the injected spins to diffuse back into the FM resulting in a faster dephasing and the observation of a Hanle linewidth broadening and hence a lower spin lifetime. This confirms other studies on graphene and is the reason for the introduction of a tunnel barrier at the FM/graphene interface.

3.1.2 Ferromagnetic tunnel barrier contact to graphene

We can minimize the contact induced spin relaxations by using FM contacts with metal oxide tunnel barriers of TiO_2. The exfoliation and contact patterning by electron beam lithography was done as described in Section A.3.3. The tunnel barrier was fabricated by electron beam evaporation of 8 Å of Ti and subsequent oxidation in air. Spin transport measurements were performed in the same configuration as the sample with a transparent tunnel barrier.

The contacts characteristics reveal a quasi-linear IV curve with a contact resistance area product of $R_cA = 585\,\Omega\mu\mathrm{m}^2$, which is significantly higher compared to the measurements without a barrier and hence can improve the efficiency of the spin detection. NL spin valve signals obtained in this structure at room temperature and a bias current of $10\,\mu$A are shown in Figure 3.2a. The difference in signal for parallel and anti-parallel contact configuration reveals a magnetoresistance of $60\,\mathrm{m}\Omega\mu\mathrm{m}^2$, which is 50% higher than without a tunnel barrier.

Furthermore, we measured the spin lifetime and diffusion constant by employing the Hanle effect in the same NL configuration. Figure 3.2b shows a Hanle curve measured with Co/TiO_2 tunnel contacts on graphene at a temperature of 300 K and a bias current of $10\,\mu$A. The line represents a fitting with Equation (1.31). The extracted spin lifetime $\tau = 80\,\mathrm{ps}$ is almost twice as large as for the tunnel barrier free device, whereas the diffusion constants are identical. Even though, there is an improvement in spin lifetime compared to the transparent barrier and matches perfectly previous studies with metal oxide barriers on SiO_2 substrate [23, 36, 84, 85], the lifetime is still orders of magnitude less than theoretical expected [21].

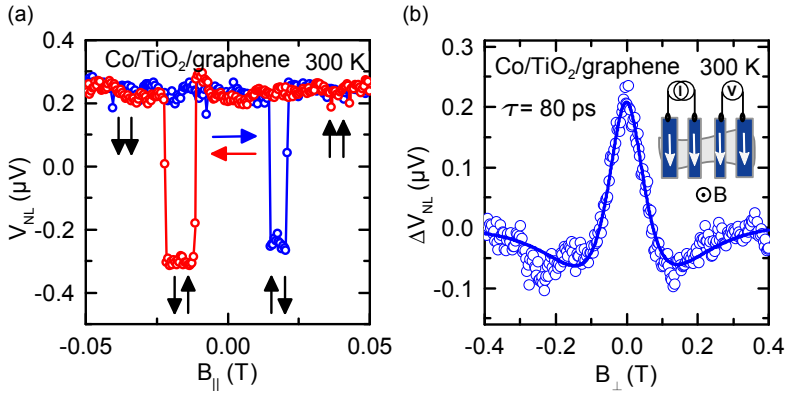

Figure 3.2: NL measurements of spin transport and precession in graphene using a Co/TiO_2 contact at room temperature with 10 μA of bias current applied. (a) NL spin valve measurement with in-plane magnetic field. The width of the electrodes are 400 nm for the injector and 150 nm for the detector with a distance of 2 μm. The signal equals a spin magnetoresistance of 60 mΩ. (b) NL Hanle measurement in the same contact configuration, but with applied perpendicular magnetic field (measurement setup shown in the inset). The extracted spin lifetime is about 80 ps.

Comparison of non-local and three-terminal Hanle measurements

To investigate if the measured spin lifetime is controlled by the FM contact, we perform measurements in the NL and 3T geometry. A 3T Hanle measurement detects the spin accumulation directly under the contact and could clarify if the origin of the reduced lifetime stems from the graphene channel or the area under the FM contacts (Figure 1.8). We investigated the same Co/TiO_2/graphene device as in the previous section. Therefore, the previous injector contact is now used for both injection and detection (compare insets in Figure 3.3a and 3.3b).

The NL measurement under the same conditions is presented in Figure 3.3a. The data were fitted with Equation (1.31) and a spin lifetime of 147 ± 20 ps and spin diffusion length of 900 ± 170 nm could be extracted. The obtained 3T Hanle measurement is shown in Figure 3.3b, measured at a temperature of 150 K and bias current of 10 μA. The data were fitted with Equation (1.34) and a spin lifetime of 172 ± 10 ps could be extracted. That means the spin lifetime observed in 3T configuration is in agreement to and confirms the results of the NL measurements. Furthermore, since the spin signal of the 3T and the NL measurement defines the accumulation underneath the injector and detector, respectively, Equation (1.20) can be used to calculate the spin diffusion length independently. The obtained

spin diffusion length is 710 ± 90 nm and therefore identical to the value extracted from the NL measurement. Similar spin parameters have been obtained for both 3T and NL measurements in the temperature range of 50 K to 300 K.

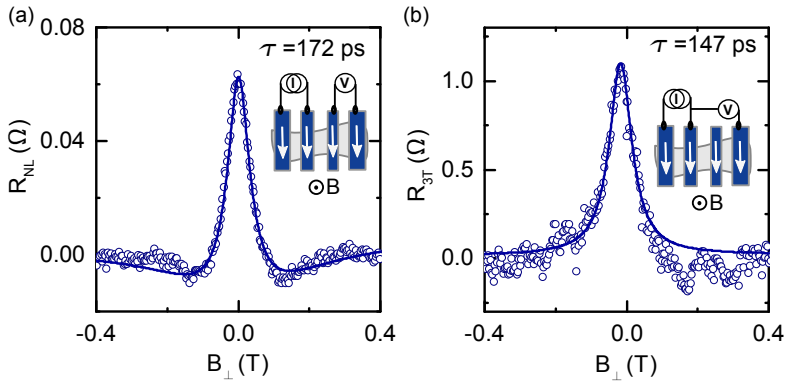

Figure 3.3: Comparison of NL Hanle measurement with 3T Hanle measurements on Co/TiO_2/graphene junction at a temperature of 150 K and a bias current of 10 μA. (a) NL Hanle signal showing a spin lifetime of 172 ± 10 ps. (b) 3T Hanle measurement results in a spin lifetime of 147 ± 20 ps.

These are important results contributing to the current understanding of the spin transport within graphene and other non-magnetic materials. Several previous studies raised concerns about 3T measurements, since the detected spin signal could stem from interface effects and not from the actual channel material [69, 70, 170]. The spin parameters extracted from NL and 3T measurements are identical, which validates the usage of both techniques. Despite the improved spin parameters detected by our NL and 3T techniques using a TiO_2 tunnel barrier, they are still orders of magnitude below expectations [21]. The similar spin parameters obtained from our 3T and NL measurements also raises the question about the influence of the contacts themselves. For a graphene channel of about 2 μm used in our previous devices, the contact induced effects could dominate the spin relaxation. Therefore, it is required to investigate the effect of longer channel lengths on the spin parameters systematically.

3.2 Long distance spin transport in CVD graphene

For practical applications and to employ a long distance spin transport over a chip scale, it is crucial to move from exfoliation flakes to commer-

cially grown single-layer graphene. One approach to produce a large area graphene is by CVD, which is by far the most viable and industrial compatible technique [171]. Such wafer scale graphene can be transferred to the Si/SiO_2 or other substrate and patterned into desired devices. Commonly, the electronic quality of CVD graphene is lower compared to exfoliated flakes because of polycrystalline domains, grain boundaries and growth related effects [78, 172]. Nevertheless, transfer related wrinkles, ripples, foreign contaminations, inter-grain connectivity and strain due to graphene-substrate interactions can be reduced by optimizing the processes (see Section A.2.2). This technique allowed us to fabricate long and uniform graphene channels with FM tunnel contacts at different distances of $2 - 16\,\mu$m for channel lengths dependent spin transport studies.

The FM tunnel contacts were fabricated identical to our experiments on exfoliated graphene using Co/TiO_2 with a contact resistance of $4 - 5\,\mathrm{k\Omega}\mu\mathrm{m}^2$ having a weak temperature dependence. The channel resistance at the Dirac point increases linearly with increasing channel length, which indicates a global uniformity of the CVD graphene and diffusive transport. The CVD graphene channel properties are characterized by resistance and gate dependence measurements. The *charge neutrality point* (CNP) of the Dirac curve was found to be at a back gate voltage of about 5 V, which indicates a very low doping concentration of the graphene. The carrier mobility was around $2000\,\mathrm{cm}^2\,(\mathrm{Vs})^{-1}$ with a sheet resistance $5\,\mathrm{k\Omega}/\square$ for all channels at room temperature.

The spin parameters were extracted by performing measurements in the NL spin valve and Hanle configurations. Figure 3.4a shows a Hanle signal measured in a CVD graphene device with a channel length of $16\,\mu$m. Besides the extraordinary long channel, the pronounced NL line shape, long spin lifetime of 1.2 ns and diffusion length of $6\,\mu$m are remarkable. Since the channel is significantly longer than the diffusion length, the spins are able to perform a full $2\pi-$precession before dephasing, which results in an anti-parallel state of spins and magnetization yielding a negative NL resistance around ± 0.01 T. Figure 3.4b shows the graphene channel length dependence of the spin lifetime and the diffusion length. A higher graphene channel length reduces the contact contribution and results in an increase of the spin parameters significantly.

These results underline the excellent properties of CVD graphene for long distance spin communication with an achieved spin transport over distances of up to $16\,\mu$m. This value is six times higher than previous reports on CVD graphene [41, 76, 173] and is the highest observed in any pristine

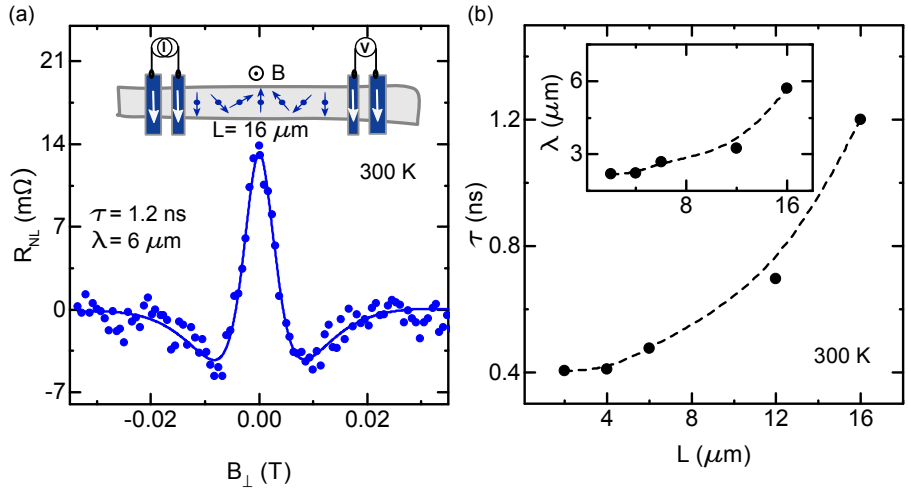

Figure 3.4: Long distance spin transport in CVD graphene and channel length dependence of spin parameters. (a) NL Hanle signal measured at a channel length of 16 μm yielding a spin lifetime of 1.2 ns. (b) Channel length dependence of the spin lifetime. Inset: Channel length dependence of the spin diffusion length. The dashed lines are guides to the eye.

form of graphene on conventional Si/SiO_2 substrate [36, 85, 174]. Even though the obtained spin lifetime of 1.2 ns is higher than in previous experimental reports, it is still lower than theoretically predicted [21]. Recent studies point towards magnetic impurities as primary source for spin scattering, which limits the spin lifetime to several nanoseconds [82, 89]. Such magnetic impurities can be reduced by improving the graphene growth and fabrication process and encapsulation it with insulating 2D materials like h-BN.

3.3 Spin injection into graphene using hexagonal boron nitride barriers

The convention of using metal oxide barriers for spin injection in graphene stems from early spintronic experiments on metallic magnetoresistive devices. Unfortunately, conventional metal oxide barriers grown on graphene, such as Al_2O_3, TiO_2 and MgO, suffer from pinholes, interface roughness and defects related to oxygen vacancies and doping in graphene [36, 85, 174]. Even though studies involving TiO_2 seeded MgO barriers showed a tunnelling behaviour [108, 175], such hybrid metal-oxide

barriers still suffer from roughness, non-crystallinity and reproducibility issues [29]. These factors greatly influence the spin polarization and spin lifetimes in graphene. Therefore, a uniform and pinhole free tunnel barrier is desired to obtain high spin lifetimes even in shorter channels. One possibility for such a material is h-BN, a 2D isomorph of graphene with a close lattice matching.

Hexagonal boron nitride is an insulating 2D layered material with a band gap of almost 6 eV, is atomically thin, topologically flat and dangling bond free [176]. Previously, h-BN has been used as a substrate yielding improved spin parameters in graphene [23, 177]. Yet, its 2D nature makes it also an attractive candidate to use as a tunnel barrier. Recent studies showed the good tunnelling properties of h-BN [77, 151], which encourages the investigation of its spin dependent tunnelling properties.

We used large area CVD grown h-BN, which is transferred onto graphene by carefully optimized transfer processes. A detailed description of the graphene exfoliation, h-BN transfer and contact patterning is given in Section A.3.3.1.

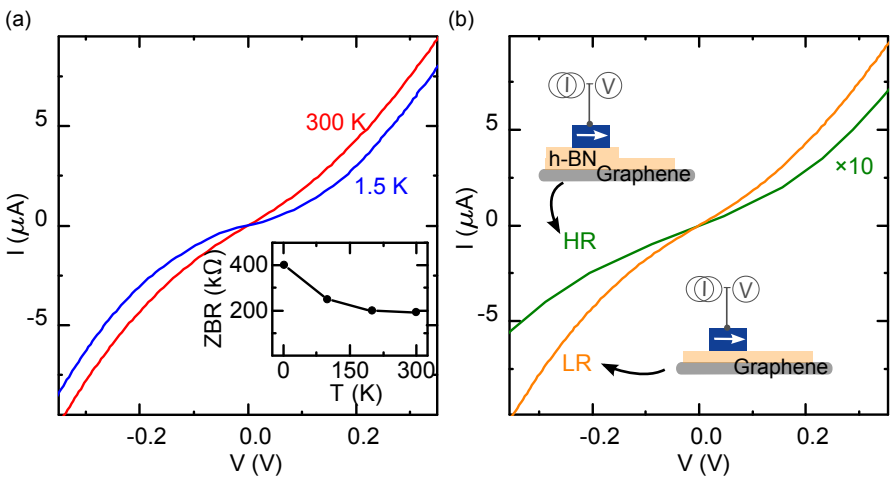

Figure 3.5: Temperature and thickness dependence of the current-voltage characteristics (IV) of Co/h-BN tunnel contacts on graphene. (a) Temperature dependence of a tunnel contact using Co and low resistive (LR) h-BN device. Inset: Temperature dependence of the resistance at *zero bias* (ZBR). (b) Room temperature IV of LR compared to a high resistive (HR) h-BN device.

The quality of the h-BN tunnel barrier was characterized by 3T IV measurements (Figure 3.5). The IV curve shows a non-linear, symmetric characteristic with a weak temperature dependence (inset in Figure 3.5a)

indicating a tunnel barrier of very good quality without pinholes and interface states. The resistance area product $R_cA \approx 15\,\mathrm{k\Omega\mu m^2}$ is more than one orders of magnitude higher than obtained for our previous devices with TiO_2 tunnel barrier. This can be advantageous for spin injection and detection. Interestingly, measurements in several contacts reveal a large range of contact resistances, which stems from the fact that CVD h-BN growth not self-limiting and results in islands of 2, 3 or even 4 layers on top of the monolayer. This can be exploited to study the h-BN thickness dependence of the spin tunnel process.

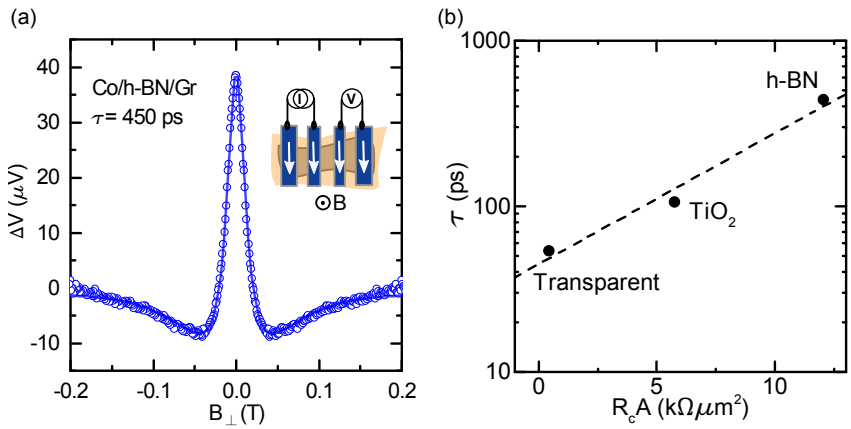

Figure 3.6: Spin transport measurements in a Co/h-BN tunnel contact on graphene with an applied bias current of $5\,\mu$A. (a) NL Hanle measurement with parallel magnetization orientation. The extracted spin lifetime is 450 ps (b) Dependence of the spin lifetime on the contact resistance of devices with a transparent, TiO_2 or h-BN tunnel barrier. The dashed line is a guide to the eye.

We studied the spin transport in a NL configuration. Figure 3.6a shows a Hanle measurement of a device with h-BN tunnel barrier on graphene, where the injector and detector contact have the similar resistance of about $15\,\mathrm{k\Omega\mu m^2}$ and hence number of h-BN layers. Fitted with Equation (1.31) a spin polarization of 15% and a spin lifetime of 450 ps can be extracted. The spin lifetime in our sample with a h-BN tunnel barrier is about 10 times higher than our devices with a direct FM contact. Figure 3.6b shows the extracted spin lifetimes for different devices demonstrating an exponential increase with increased contact resistance. This clearly demonstrates the excellent tunnelling properties of the CVD h-BN barrier providing an efficient spin polarized tunnel injection and detection process in graphene.

Furthermore, we investigated the spin polarized tunnelling with dif-

ferent numbers of layers of the h-BN tunnel barrier on several graphene spin transport devices. We divide the measured resistance into three categories, whereof a direct contact exhibits a *transparent resistance* (TR), single-layer h-BN possess a *low resistance* (LR), and more layers demonstrate a *high resistance* (HR). The measured injector/detector combinations can be classified by its resistance $R_{id} = \sqrt{R_i R_d}$. Previously, we already discussed the symmetric cases of injector/detector, such as TR/TR (Section 3.1.1) and LR/LR (see upper panel in Figure 3.7a). In those devices the contacts are identical, that means $R_{id} = R_i = R_d$ and the extracted polarizations are $P_{id} = \sqrt{\gamma_i \gamma_d} = \gamma_i = \gamma_d$. This allows us to calculate the required parameters to investigate the properties of the mixed configurations of LR/TR and HR/LR devices. We also observe an increase of the

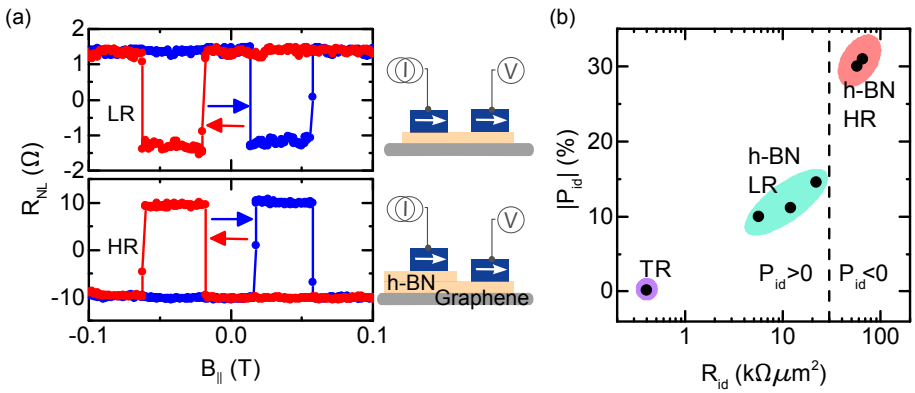

Figure 3.7: Layer thickness dependence of the h-BN tunnel barrier. (a) Spin valve measurement in different FM tunnel contact combinations at room temperature and a bias current of 5 μA. Top panel: Injector and detector exhibit a LR yielding a positive spin polarization. Bottom panel: The injector is high resistive, whereas the detector is LR resulting in a negative spin polarization. (b) Scaling of the extracted spin polarization $P_{id} = \sqrt{\gamma_i \gamma_d}$ with resistance $R_{id} = \sqrt{R_i R_d}$ of the contacts. An increase in contact resistance goes along with an increase in spin polarization, whereas injector/detector combinations of HR/LR ($R_{id} > 25\,\mathrm{k\Omega\mu m^2}$) result in a large but negative spin polarization.

spin signal and therefore spin polarization with increased contact resistance R_{id} (Figure 3.7b), which agrees with previous theoretical [35, 178] and experimental studies [179]. Interestingly, for the injector/detector HR/LR h-BN devices an inversion of the spin signal can be observed (lower panel in Figure 3.7a). This has been theoretically proposed to be the general expectation for h-BN tunnel junctions [180, 181]. That means single and few-layers of h-BN should act as a spin filter with dominating minority spin

conduction yielding a polarization of up to 100% in three-layer h-BN tunnel junctions [29]. Nevertheless, if both injector and detector in the HR/LR structure would have the same spin polarization, no sign reversal could be observed. This indicates that the observable spin polarization properties of these contacts are opposite. Hanle measurements provide a negative polarization $|P_{id}| = \gamma_{LR}\gamma_{HR} \approx 30\%$ in the HR/LR device, whereof the γ_{LR} could be extracted in a symmetric LR/LR structure as about 15%, which yields $|\gamma_{HR}| = 65\%$. Such a high polarization is significantly larger than the intrinsic FM polarization and is, combined with the negative sign, a clear evidence for active spin filtering in the h-BN barrier. The missing sign inversion for LR devices can be attributed to several factors: A thicker h-BN barrier ensures a better coverage without pinholes which can be present in thinner LR h-BN induced during CVD growth or transfer processes. Also, HR h-BN barriers posses a tunnel resistance much larger than the graphene channel resistance resulting in an electric field perpendicular to the graphene sheet. This can favour the conservation of the crystal momentum and a dominance by the minority spin channel, whereas a in-plane electric field in LR h-BN barrier can break the translational invariance and destroy the spin filtering effect. However, a detailed and quantitative understanding of such a mechanism needs to be confirmed by more theoretical and experimental studies.

We demonstrate that h-BN acts as an excellent tunnel barrier for spin injection and detection in graphene. As expected [29, 180, 181], the spin polarization increases with the number of h-BN layers and we achieve a large negative tunnel spin polarization of 65% in HR h-BN devices at room temperature. This is well beyond its use as a tunnel barrier for addressing the conductivity mismatch problem or as an insulating substrate and gate dielectric. Furthermore, the employed CVD h-BN allows for the development of large scale fabrication of spin tunnel barriers for novel applications. The spin transport properties could be further improved by an optimization of the growth process of h-BN and its heterostructure with graphene.

4

Two-dimensional semiconductor for spintronic applications

Two-dimensional (2D) *semiconductors* (SC) are a rapidly growing research field closely following the development of graphene. Despite the excellent transport properties of pristine graphene, it has neither a band gap nor spin-orbit coupling, which are indispensable requirements for a switching action in charge or spin based transistor applications. Engineering a band gap or inducing spin-orbit coupling in graphene has so far proved detrimental to its intrinsic properties [90]. Semiconducting *transition metal dichalcogenides* (TMDC) have emerged as a potential alternative 2D crystal demonstrating solutions for several novel nano-electronic and optoelectronic applications [93, 96, 97, 182]. These electron doped materials are recently complemented by SC *black phosphorous* (BP), which exhibits preferential hole doping with ambipolar tendencies [110, 114–116].

For the practical realization of spin based devices, the electrical injection, transport, manipulation, and detection of spin polarized carriers in the 2D SC/*ferromagnet* (FM) heterostructures are primary requirements. However, in such contacts a high Schottky barrier of $100 - 200\,\mathrm{meV}$ is associated with the charge depletion region at the interfaces [59, 60]. The introduction of a tunnel barrier to create FM tunnel contacts on 2D SC could reduce this Schottky barrier and resolve the conductivity mismatch problem promoting an efficient spin injection and detection (see Chapter 1).

Furthermore, achieving high channel mobilities and better transistor properties in such 2D SC FETs could allow for long distance spin transport and enable active spin manipulation in the MoS_2 channel by using a gate voltage (Figure 4.1a).

In this chapter, we present an approach to engineer the contact resistance of Co on the 2D SC MoS_2 and BP by introducing a thin TiO_2 tunnel barrier. This reduces the Schottky barrier and hence the contact resistance and improves the transistor performance. Subsequently, we correlate the contact resistances of our devices with MR calculations on the basis of the spin transport model (Paper VII and Paper VIII). Finally, we study a vertical MoS_2/graphene heterostructure with a short channel length and a gate tunable Schottky barrier at the 2D material junction.

4.1 Transistor performance with ferromagnetic contacts

The 2D SC flakes were mechanically exfoliated onto a SiO_2/Si substrate. The FM Co electrodes with and without a TiO_2 tunnel barrier were prepared by nanofabrication techniques (see Section A.2.2.1). We used multilayer 2D SC with a thickness of about 10 nm, which promotes a larger density of states, multi-channel conduction and improved substrate screening yielding high drive currents [59, 103, 104].

Initially, we studied the MoS_2 devices by measuring the source-drain characteristic with applied back gate voltages in different configurations to determine the output and transfer characteristics (Figure 4.1a). Output characteristics were measured by sweeping the drain-source voltage (V_{ds}) while measuring the drain-source current (I_{ds}) at several gate voltages (V_{gs}). The transfer characteristics were recorded by sweeping the V_{gs} while measuring the I_{ds} at different V_{ds}. At zero gate bias ($V_{gs} = 0\,\mathrm{V}$) and room temperature we observed a quasi-symmetric non-linearity of the $I_{ds} - V_{ds}$ due to the back-to-back Schottky diode structures of the devices (Figure 4.1b). The direct MoS_2/Co contact demonstrates a large contact resistance area product of $R_cA = 3 \cdot 10^{-7}\,\Omega\mathrm{m}^2$ and a channel resistivity of $\rho = 3 \cdot 10^{-3}\,\Omega\mathrm{m}$. A large contact resistance indicates a high Schottky barrier, which can yield problems for the spin injection and detection [106, 162]. In contrast, the MoS_2/TiO_2/Co device exhibits a dramatically reduced contact resistance of $R_cA = 2.4 \cdot 10^{-9}\,\Omega\mathrm{m}^2$. A similar reduction in contact resistance has previously been observed using MgO as a tunnel barrier on single layer MoS_2 [60] and in germanium [183], and attributed to a reduction of the *Schottky bar-*

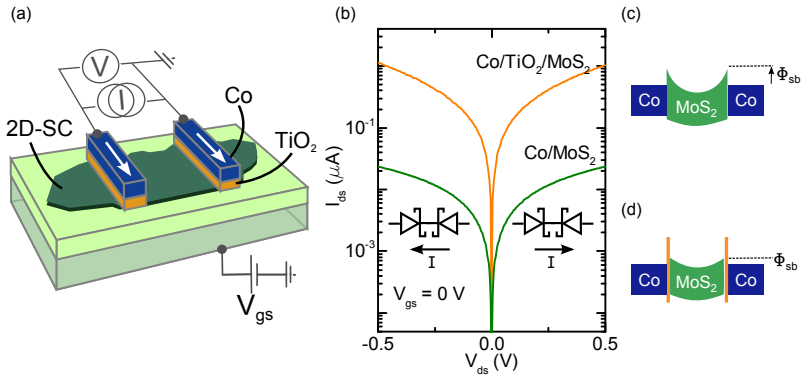

Figure 4.1: Lateral 2D SC *field effect transistor* (FET). (a) Schematic of a 2D SC FET with FM Co/TiO_2 tunnel contacts fabricated on a highly doped Si/SiO_2 substrate used for back-gating. (b) Output characteristic of the MoS_2 FET with and without a TiO_2 tunnel barrier. (c) Band schematic of a $Co/MoS_2/Co$ structure. A Schottky barrier is formed at the interfaces. (d) Band schematic of a $Co/TiO_2/MoS_2/TiO_2/Co$ structure. A reduced Schottky barrier is observed at the interface due to pinning effects.

rier height (SBH) (Figure 4.1c and 4.1d). It has to be mentioned that the output characteristics of both devices show a linear $I_{ds} - V_{ds}$ behaviour at small bias voltages, which does not necessarily indicate an ohmic contact. Two-dimensional materials can exhibit a Schottky barrier width exceeding the flake thickness resulting in a full depletion of charge carriers in the flake under the contacts [93]. Thermally assisted tunnelling in few-layers of MoS_2 at finite temperatures can cause a linear dependence despite the presence of a sizeable Schottky barrier at the interface. The Schottky barrier and the carrier depletion at the interfaces give rise to higher contact resistances and non-linear $I_{ds} - V_{ds}$ characteristics at high voltages with a strong gate dependence, as expected for a SC transistor.

The transistor ON-OFF ratio $^{I_{on}}/_{I_{off}}$ and the effective field effect mobility μ_{eff} can be extracted from the transfer characteristics (Figure 4.2a). For the MoS_2/Co device μ_{eff} is found to be $12\,\mathrm{cm^2V^{-1}s^{-1}}$, which is comparable with previously reported mobilities for few-layer MoS_2 on SiO_2 substrates [59, 99]. In contrast, the devices with TiO_2 exhibits a much higher mobility of $\mu_{eff} = 76\,\mathrm{cm^2V^{-1}s^{-1}}$. Furthermore, the MoS_2 devices with direct Co contact show a current ON-OFF ratio of $^{I_{on}}/_{I_{off}} > 10^5$, whereas a device with TiO_2/Co contact exhibits $^{I_{on}}/_{I_{off}} > 10^6$. This demonstrates that the introduction of a TiO_2 tunnel barrier lowers the SBH and hence reduces the contact resistance by $2-3$ orders of magnitude and increases

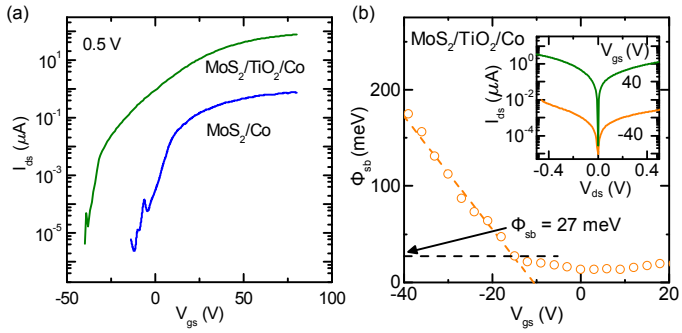

Figure 4.2: Transfer characteristic and Schottky barrier dependence of the lateral MoS_2 FET. (a) Transfer characteristics of MoS_2 FET with direct Co and Co/TiO_2 contacts at a drain-source voltage of 500 mV. (b) Dependence of the Schottky barrier on the applied back gate voltage. The linear dependence for $V_{gs} < -12$ V is due to dominating thermionic transport over the Schottky barrier. Inset: Output characteristics of the Co/TiO_2/MoS_2 FET at $V_{gs} = \pm 40$ V.

the effective field effect mobility by a factor of six.

The SBH was extracted performing temperature dependent $I_{ds} - V_{ds}$ measurements (see Section 1.5.3). As expected, we obtained a drastic reduction of the SBH Φ_{sb} at the flat band voltage from 121 meV for the direct Co contact to 27 meV in the MoS_2/TiO_2/Co device (Figure 4.2b). This can be understood, since the SBH is determined by various parameters, such as the work function of Co (Φ_m), the electron affinity of MoS_2, the thickness and dielectric constant of TiO_2, the charge neutrality level, and the surface density of gap states at the MoS_2 interface [161, 183–185]. The critical parameters which can influence the SBH are the charge neutrality level, and the surface density of gap states at the MoS_2 interface with the preparation of the TiO_2 barrier. The interface gap states can alleviate the Fermi level pinning and result in a lowering of the SBH [59, 60, 183, 185, 186].

We observed a similar low Schottky barrier for our BP FETs. In contrast to MoS_2, BP is dominantly hole doped, which means the barrier is pinned close to the valence band. It has been demonstrated before that the energy level of interface state and defect pinning depends strongly on the substrate material [187]. Furthermore, the smaller band gap of few-layer BP allows both electron and hole conduction at different gate voltages. The ambipolar behaviour has a dominant p-type character with an effective field effect channel mobility of $\mu_{eff} = 155\,\mathrm{cm^2V^{-1}s^{-1}}$ and an ON-OFF ratio of $I_{on}/I_{off} > 10^4$ in the hole conduction regime at room temperature (see Paper VIII). The SBH could be reduced from 206 meV to about 50 meV by

adding the TiO_2 tunnel barrier. These results are extremely promising for the development of spin transistors and logic applications based on 2D SCs and their heterostructures.

4.2 Magnetoresistance calculations

In order to understand the viability of FM tunnel contacts on the 2D SC for the observation of two-terminal *magnetoresistance* (MR), we put the contact resistances in our devices into perspective with the spin transport theory as discussed in Section 1.4.1. Considering a FM/I/2D-SC/I/FM structure we can estimate the optimal contact resistance to observe the maximal MR using Equation (1.18). This theory requires next to the resistances also the spin polarizations of the contact, the channel length and the spin lifetime. Even though there are predictions for the spin lifetime in MoS_2 [97] and BP [188], experimental values are still unavailable. Therefore, we calculated the contact resistance dependence of the MR for different expected spin lifetimes. Furthermore, we considered the device parameters obtained in the ON-state, where the 2D SC transistors have a lower channel resistance and hence a reduced conductivity mismatch. Equation (1.18) gives a bell shaped curve having a peak at an optimal contact resistance with low back diffusion and a high spin potential splitting (see Section 1.4.1 and Figure 4.3a).

For our MoS_2/Co device the contact resistance is high (in FET ON-state with $V_{gs} = 60\,\mathrm{V}$ and $R_cA = 4 \cdot 10^{-9}\,\Omega\mathrm{m}^2$) and falls into the upper regime of a low MR. This is very similar to the result for the BP/TiO_2/Co device, which lies still above the optimal range despite the lowered contact resistance compared to a direct BP/Co contact (see Paper VIII). In contrast, the thin TiO_2 tunnel barrier dramatically reduces the contact resistance ($R_cA = 4 \cdot 10^{-10}\,\Omega\mathrm{m}^2$) towards the optimum range for the observation of a large MR (Figure 4.3a). Further gate dependent measurements and respective simulations of the MR demonstrate the tunability of the channel, contact and hence MR by the gate voltage (Figure 4.3b). This offers a multitude of possibilities to combine spintronic effects with regular electronics.

These calculations depend strongly on the actual spin lifetime and device channel length. A shorter lifetime or a longer channel result in a reduction of the spin potential splitting at the detector contact yielding a reduction of the MR. Especially for low spin lifetimes an additional shift towards lower resistances can be observed, due to the reduced spin diffu-

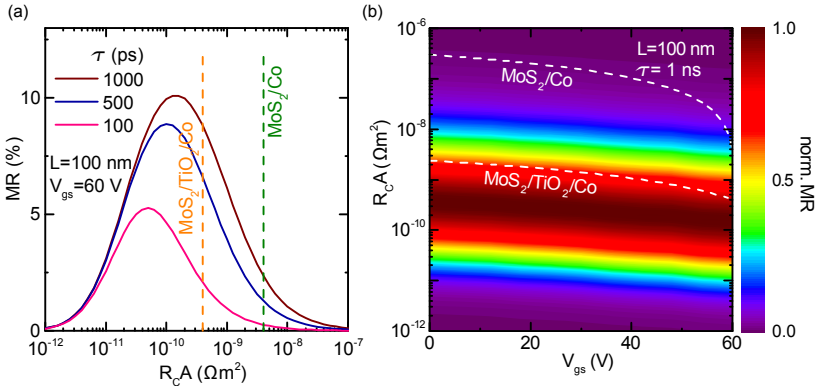

Figure 4.3: Calculated magnetoresistance of FM/I/MoS_2/I/FM spin-FET structure as a function of the contact resistance area product (R_cA) for a channel length of 100 nm at room temperature. (a) Calculation for different spin lifetimes τ_{sf} at a gate voltage $V_{gs} = 60$ V (on-state). The vertical lines represent the R_cA value for the TiO_2/Co tunnel and the direct Co contact on MoS_2 in our experiments. (b) MR as a function of gate voltage and contact resistance. The dashed lines represent the variation of contact R_cA of our devices with gate voltage.

sion length in the NM (Figure 4.3a). This can dramatically influence MR measurements, since the effective spin lifetimes in MoS_2 and BP are unknown so far. In contrast, decreasing the channel length can significantly enhance the MR. This has to be considered for practical applications and future devices to achieve a detectable MR signal.

4.3 Molybdenum disulphide / graphene heterostructures

The excellent spin transport in graphene (as discussed in Chapter 3) and the promise of tuning the charge and spin current in MoS_2 motivated the idea of creating a hybrid device, which combines these properties. A stack of the 2D materials would enable the spin and current direction to be vertical, hence limiting the channel length to the flake thickness. This could significantly improve the MR measurements, as discussed in the previous section.

Our device consists of a heterostructure of CVD graphene and exfoliated MoS_2 with FM tunnel contacts (see fabrication in Section A.3.3.2). We designed the contacts so that the predominant transport occurs across the vertical interface of MoS2/graphene heterostructure (Figure 4.4a). In

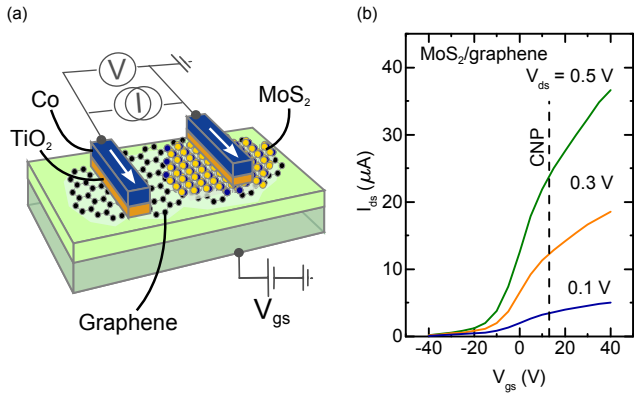

Figure 4.4: Vertical MoS_2/graphene FET. (a) Schematic of a vertical FET based on a MoS_2/graphene heterostructure. The transistor channel is perpendicular to the MoS_2 and graphene flake under the source contact, whereas a second FM contact on graphene leads to the drain. (b) Transfer characteristics for different V_{ds}. The charge neutrality point (CNP) of the graphene has no significant effect on the I_{ds} for short graphene channel lengths.

contrast to metal electrodes, the graphene exhibits a low screening and hence allows a gate tuning of the charge carrier concentration in MoS_2 and graphene, which makes it ideal as electrode in vertical FET structures. The transfer characteristics of such vertical MoS_2/graphene FETs is shown in Figure 4.4b.

The lateral MoS_2 FET demonstrates a symmetric $I_{ds} - V_{ds}$ with a strong gate dependence (see Figure 4.1b) affecting the channel charge carrier concentration. In contrast, the vertical MoS_2/graphene heterostructure demonstrates a highly asymmetric $I_{ds} - V_{ds}$ characteristic, which becomes symmetric only for high gate voltages (Figure 4.5a). This can be explained by a gate tuning of the Fermi level in the graphene, which directly affects the SBH. Recent studies observed the similar behaviour using non-magnetic metallic contacts [189, 190]. Figure 4.5b shows the gate dependence of the SBH, where a negative gate voltage shifts the Fermi level in the valence band of graphene and hence a high SBH (see left inset in Figure 4.5b), which yields a Schottky diode behaviour in the output characteristic ($V_{gs} = -40$ V in Figure 4.5a). For positive gate voltages the Fermi level in graphene shifts to the conduction band giving rise to a reduced Schottky barrier (see right inset in Figure 4.5b).

This demonstrates that FM contacts with a TiO_2 tunnel barrier are promising spin injectors for vertical MoS_2/graphene FET heterostructures.

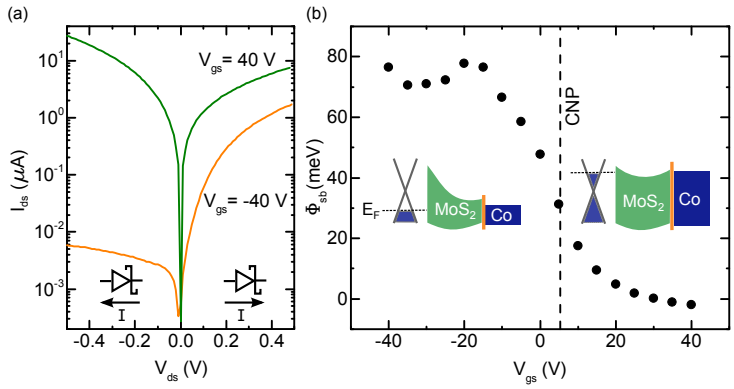

Figure 4.5: Gate dependence of the vertical MoS_2/graphene FET. (a) Gate dependence of the output characteristic. The asymmetry in the OFF-state ($V_{gs} = -40\,\mathrm{V}$) indicates an enhanced Schottky barrier at the MoS_2/graphene interface. (b) Gate dependence of the Schottky barrier height (SBH). The gate-tunable Fermi level in graphene allows a control of the SBH at the MoS_2/graphene interface. The dashed line defines the CNP of the graphene.

The vertical structure allows to create channel length of only a few nanometres, which is practically difficult to achieve in a lateral structure with state-of-the-art fabrication techniques. Nevertheless, the generation and detection of local or non-local spin accumulations in these heterostructures requires an optimization of the MoS_2/graphene interface [190] and better control over the charge carrier concentration in the MoS_2 [191]. These experiments also demonstrate that 2D materials exhibit unique electrical properties when forming a heterostructures, which, combined with their individual spin properties, could yield novel spintronic devices and applications.

5

Electrical detection of spin currents in topological insulators

Three-dimensional (3D) *topological insulators* (TI) are a new class of materials with an interesting band structure. Unlike conventional materials TIs exhibit topologically protected metallic surface states with massless Dirac fermions, whereas the bulk of the material is usually semiconducting (SC) [120, 141]. In contrast to graphene, a strong spin-orbit coupling constrains the spin in those surface states to be perpendicular to the momentum [54, 141]. This *spin-momentum locking* (SML) causes a spin polarized charge current when the carriers have a finite momentum by applying an electric field. This makes TIs an alternative to create highly polarized spin currents, similar to FM contacts.

We chose the TI Bi_2Se_3 for our experiments since it possesses a single Dirac cone and the largest known bulk band gap in a TI of 300 meV [192, 193]. This makes it an ideal prototype to study topological effects. Furthermore, its weak electron-phonon coupling allows the persistence of topological surface states at least up to 300 K [133, 194], which is a key requirement when considering to employ surface state related effects for room temperature applications.

Here we demonstrate the electrical detection of spin polarized currents on the surface of exfoliated Bi_2Se_3 flakes by ferromagnetic tunnel contacts at room temperature, as presented in Paper IX. Initially, Hall and *weak*

anti-localization (WAL) measurements are used to characterize the transport properties of the Bi_2Se_3 crystal. Subsequently, we measure the surface spin polarization by employing a similar technique to the spin valve measurement.

5.1 Charge and magneto transport

Flakes of Bi_2Se_3 were mechanically exfoliated onto a SiO_2/Si substrate. Contact electrodes (Ti/Au or Co) with or without a TiO_2 tunnel barrier were prepared by nanofabrication techniques (see Section A.3.3). We characterized our Bi_2Se_3 flakes via electrical transport measurements using direct Ti/Au contacts in a multi-terminal configuration. The channel resistance shows a metallic temperature dependence with a sheet resistance $R_\square = 36\,\Omega$ at room temperature. Such a low resistance (for a SC 2D bulk material) can be understood, since a large temperature independent charge carrier concentration of $5 \cdot 10^{19}\,\mathrm{cm}^{-3}$ was extracted from the Hall measurements and implies a large bulk conductance channel. Furthermore, we observe a high mobility of $2000\,\mathrm{cm}^2(\mathrm{Vs})^{-1}$ already at room temperature, which increases by a factor of 2.5 when cooling down to 2 K. The charge carrier concentration and mobility lie in the upper range of the parameters observed in previous studies [195].

Further information about characteristic lengths and dimensionality in the system can be gained through the WAL effect. A perpendicular magnetic field varies the interference of back-scattered electron pairs, which allows to extract the scattering class and the phase coherence length [55] (see Section 1.5.2). Its characteristic reduction in conductivity when applying an external magnetic field is shown in Figure 5.1a. Three-dimensional TIs with 2D surface states usually exhibit a very strong SO coupling and belong to the so-called symplectic class, where the prefactor in Equation 1.36 becomes $\alpha = -1/2$. It has been demonstrated that $\alpha = -1$ if the bottom and top surface of the TI are coupled [196]. We observe such a coupling up to 4 K ($|\alpha| \approx 1.2$), whereas for higher temperatures an $|\alpha| \approx 1/2$ could be extracted (Figure 5.1b). This transition coincides with a constant $l_\varphi \approx 400\,\mathrm{nm}$ at low temperatures, changing in a $l_\varphi \propto T^{-0.54}$ dependency at higher temperatures (Figure 5.1c). Both observations indicate a coupling, or additional transport channels, at temperatures up to 4 K, whereas $|\alpha| \approx 1/2$ and $l_\varphi \propto T^{-\frac{1}{2}}$ demonstrate, as expected, a 2D system [196, 197]. It has to be noted that both the phase coherence length and the maximum temperature, where we observe WAL, are large compared to other studies

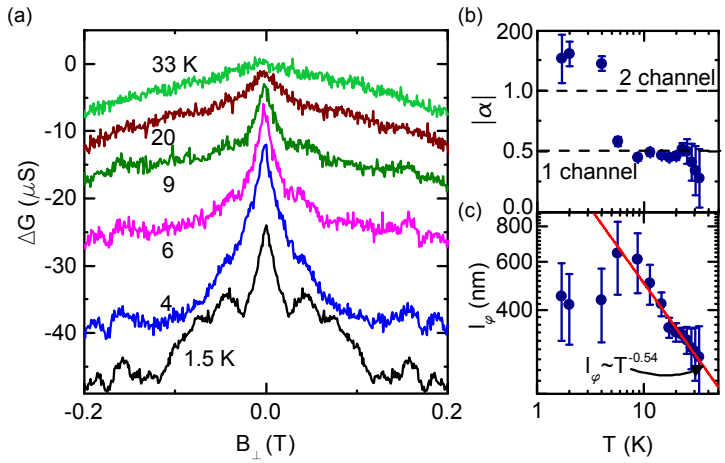

Figure 5.1: Weak anti-localization (WAL) measurement in Bi_2Se_3. (a) Magnetic field dependence of the conductance at temperatures from 1.5−33 K. The decrease at high fields is characteristic for WAL. (b) Temperature dependence of channel number α and (c) phase coherence length l_φ.

on Bi_2Se_3 [57]. Such a large signature for WAL has been predicted to allow the direct detection of surface-edge states by transport measurements up to high temperatures [133].

5.2 Electrical detection of spin-momentum locking

Spin states in other *non-magnetic materials* (NM) were reproducibly detected by FMs probing the chemical potential of the spins aligned to its magnetization. It has been established to use tunnel contacts to avoid reactions or doping between the FM and the NM [18, 28, 36]. Therefore, to detect spin polarized surface currents due to SML in the Bi_2Se_3 flakes we used FM Co contacts with a TiO_2 tunnel barrier in a multi-terminal configuration (Figure 5.2a). Such contacts are very sensitive to spin accumulations even in presence of a large unpolarized background contribution, as shown in Chapter 2 and 3. Our Co/TiO_2 tunnel contacts on Bi_2Se_3 demonstrate a non-linear current-voltage characteristic with a *zero bias resistance* (ZBR) of 4 kΩ at room temperature, which increases by a factor of 2.5 when cooling down to 70 K (Figure 5.2b). For TIs, it has previously been demonstrated that the SML in the surface states of epitaxially grown Bi_2Se_3 can still be probed at low temperatures in spite of the large bulk

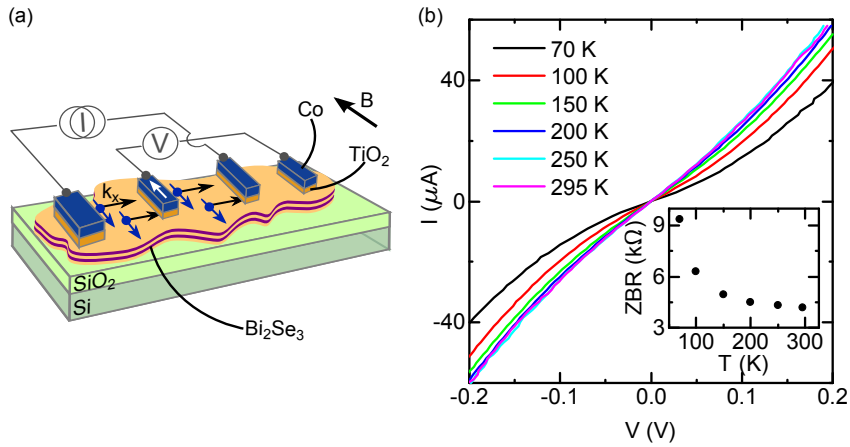

Figure 5.2: Device and transport characteristic of a Co/TiO_2 tunnel contact on Bi_2Se_3. (a) Schematic of a Bi_2Se_3 flake on SiO_2/Si substrate with FM tunnel contacts for spin sensitive measurements. (b) The current-voltage characteristic measured between $70 - 300\,K$ demonstrating a strong non-linear behaviour and a weak temperature dependence of the zero bias resistance (ZBR) (inset).

contribution [31]. Additionally, our exfoliated flakes show an improved mobility compared to commonly grown materials [57], which can further improve the detectability of surface currents [195].

The measurement schematic to detect spin-momentum locked spin polarized currents on the surface of the Bi_2Se_3 flake is shown in Figure 5.2a. Applying a current between two contacts yields a charge carrier flow between the electrodes. This finite momentum leads to a locking of the spin orientation for carriers in the surface state. A FM electrode on the charge transport channel can probe the spin potentials against a reference contact outside of the applied electric potential. Keeping the applied bias current fixed and sweeping an in plane magnetic field allows to switch the magnetization of the detector electrode. If spin and magnetization are parallel, a reduced potential drop can be detected compared to the anti-parallel configuration. The lower panels in Figure 5.3 show the magnetic field dependence of the detected voltage signal measured at room temperature, sweeping $\vec{B}$ up (blue curve) and down (red curve) symmetrical around zero. The resulting hysteresis stems from the finite coercive field of the FM detector contact. Reversing the current direction ($-50\,\mu A$, Figure 5.3b) locks the spins in the opposite direction resulting in an inverted switching hysteresis. This behaviour is analogue to a spin-valve measurement between

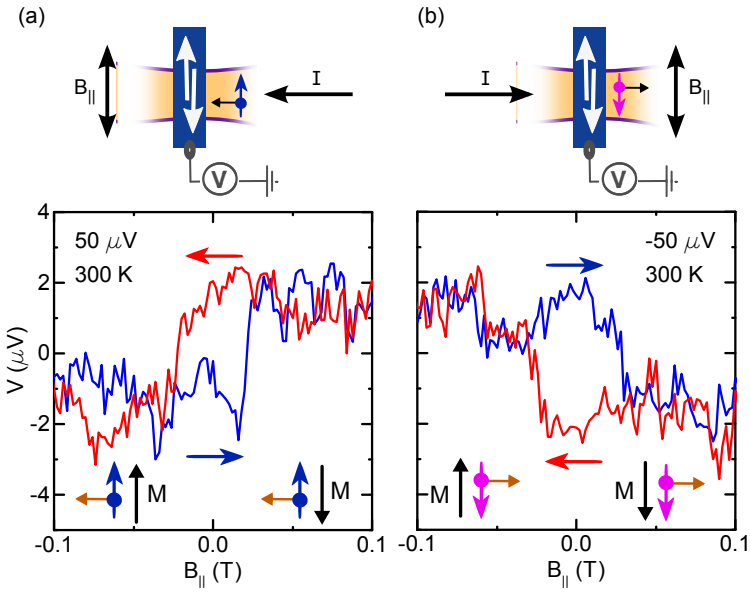

Figure 5.3: Electrical detection of SML in Bi_2Se_3 at room temperature and schematics for spin-valve measurements between spins (S) on the Bi_2Se_3 surface due to SML and magnetization (M) of the detector FM contact. (a) A positive charge current in the TI channel creates a spin polarization $S_\uparrow$. A FM contact on this transport channel can detect a voltage signal in reference to a contact outside the electric field. Sweeping an in-plane magnetic field yields a spin-valve measurement with a hysteretic switching due to the magnetization flip of the FM. Lower panel: Measured at 300 K for a bias current of $+50\,\mu$A. (b) Reversing the current direction yields a change in spin orientation $S_\downarrow$. This results in the inversion of the detected spin signal. Lower panel: Measured at 300 K for a bias current of $-50\,\mu$A.

the spin polarized surface current, controlled by the current direction, and the magnetization of the FM, controlled by the external in-plane magnetic field.

For different bias currents at room temperature a linear dependence of the spin signal ΔV was observed (see Paper IX). This is expected, since the spin current density should scale linearly with the charge current density [54, 141]. The switching direction rules out a dominant contribution by Rashba spin-splitting, which should exhibit the opposite sign [198, 199]. The linear bias dependence rules out any current-related spin caloric and fringe field induced localized Hall effects, which would be magnetization and current direction independent [31]. Further control experiments with

NM and Co/Ti contacts allow us to unequivocally rule out any similar contribution from the anomalous Hall effect and other anisotropic effects in the FMs (see Supplementary information of Paper IX). Further temperature dependent measurements reveal a high stability showing only a weak increase of the detected spin signal when cooling down. Such a behaviour has been expected, since the surface states were shown to be thermally stable at least up to room temperature [133, 141].

The measured voltage drop under the FM contact due to a current-induced spin polarization on the Bi_2Se_3 surface is theoretically described in Equation (1.35). Some of the required parameters are not electrically accessible at high temperature and therefore we relied on data obtained from *angular resolved photo-emission spectroscopic* (ARPES) measurements up to room temperature. For Bi_2Se_3 the *surface contribution* η has been experimentally estimated to range between $2-9\%$ [53, 200–202] and the *mean free path* l_{mf} of the carriers has been measured to be between $20-50\,\mathrm{nm}$ at room temperature [194, 203]. Using these parameter ranges we can extract a surface spin polarization of 5-38%. The median of this range lies within the lower limit of previously reported surface polarizations, which are usually between 20-40% [31, 133, 198]. Inter-state scattering at high temperatures [53] or a reduction of the spin signal by the Rashba effect [31, 198, 199, 204] could cause such a lowering of the observed signal. These effects could be investigated using TIs with a lower bulk carrier concentration, which can be achieve by hole doping of Bi_2Se_3 [192, 195] or novel compounds, such as $Bi_{1.5}Sb_{0.5}Te_{1.7}Se_{1.3}$ [130, 205]. Gate dependence studies could allow a better estimation of the electrically detected spin polarization, the contribution by other effects and the limiting scattering mechanisms.

Summary and Outlook

The spin degree of freedom of electrons is considered as an alternative state variable to overcome the limitations of charge based technology. The spintronic device performance depends strongly on the spin relaxation mechanisms in the host material. So far, silicon and graphene gained the main interest due to their low *spin-orbit* (SO) and hyperfine interaction, which yields a long spin coherence lengths, but hinders the intrinsic spin manipulation. Therefore, the importance of newly discovered *two-dimensional semiconductors* (2D SC), *topological insulators* (TI) and *hexagonal boron nitride* (h-BN) increases rapidly due to their strong SO coupling, the existence of spin polarized surface states and insulating band structure, respectively. Despite the recent advances in spintronics, most of these new materials are not explored yet. Additionally, even though Si and graphene are extensively investigated, their spin parameters are far below the theoretical expectations and the spin relaxation mechanisms involved are not fully understood. This thesis studies the basic spin parameters and their performance in Si and 2D materials, as well as their heterostructures, to investigate their potential for the integration in future technologies.

We demonstrated the creation of a large spin polarization up to 34% in degenerate Si at room temperature, using an ozone oxidized SiO_2 tunnel barrier. Furthermore, we investigated the role of the *Schottky barrier* (SB) on the spin transport. Interestingly, for non-degenerate hole doped Si, we observed a sign reversal of the spin signal in the low bias regime. This change in the spin transport can be due to a transition from a direct to a localized state assisted tunnelling, which provides a deeper insight into the spin transport phenomenon. Although large spin accumulation could be created in Si at room temperature, the spin diffusion length and lifetime under the contacts were found to be limited to 250 nm and 100 ps, respectively.

An ideal candidate for long distance spin communication with predicted long spin diffusion length and lifetime is graphene. We studied the influence of the tunnel contacts in different measurement geometries, which demon-

strated the necessity of a tunnel barrier, but also indicated the presence of contact induced effects on the spin lifetime in devices with a short graphene channel length. This was further supported by studying the channel length dependence of the spin diffusion in *chemical vapour deposited* (CVD) graphene on a SiO_2 substrate. We observed a significant increase of the spin parameters achieving a spin transport over a distance of 16 μm, a spin lifetime of 1.2 ns and a spin diffusion length of 6 μm at room temperature. This is the first observation of such high values in pristine graphene on SiO_2, which is particularly interesting, since the size of CVD graphene can be arbitrarily scaled up and implemented in industrial fabrication processes.

Next, we investigated h-BN as a 2D insulating tunnel barrier to overcome the metal oxide contact related effects and increase the spin polarization and lifetime. Our initial experiments on Si and in a magnetic tunnel junction revealed a low effective polarization of 5%, comparable to the one obtained using common metal oxide barriers. This could stem from the larger area of the contacts, the growth quality of the CVD h-BN and the process design. In contrast, smaller contacts on h-BN/graphene demonstrate an excellent spin polarized tunnelling behaviour of h-BN. With increasing thickness of the h-BN we also observed an enhancement of the spin lifetime and polarization up to 65% at room temperature. For thick h-BN barriers the tunnel spin polarization was found to be exclusively negative. This allows for the development of large scale fabrication of CVD h-BN spin tunnel barriers.

Even though graphene is an excellent material for long distance spin transport, its low *spin-orbit* (SO) coupling inhibits a spin manipulation required for spintronic devices. Two-dimensional SC and *topological insulators* (TI) possess a strong SO coupling, which promises new properties and allows for studying novel spintronic effects. First, we investigated the electrical transport in the 2D SC MoS_2 with *ferromagnets* (FM) as source and drain contacts. We demonstrate that the presence of a large SB resistance at the 2D SC/ferromagnet interface is a major obstacle for the electrical spin injection and detection. Introducing a TiO_2 tunnel barrier significantly decreases the SB at the interface. This results in an enhancement of the transistor ON-state current by two orders of magnitude and an increment in the field effect mobility by a factor of six. Comparing our results with spin transport theory reveals that the contact resistance of the $MoS_2/TiO_2/Co$ contacts lies in the optimal range for spintronic devices based on MoS_2. Similar results are also observed for *black phosphorous* (BP) *field effect transistors* (FET). Subsequent experiments of a

vertical graphene/MoS_2 FET reveal a tunable SB at the 2D material interface. Such a device geometry provides a short 2D SC channel combined with the excellent spin transport in graphene, which could enable novel spintronic heterostructures.

In TIs the strong SO coupling yields a band crossing creating metallic surface states with a *spin-momentum locking* (SML) of the charge carriers. In such crystals we demonstrated the electrical detection of the spin polarization due to SML on the surface of Bi_2Se_3 by employing spin sensitive FM tunnel contacts at room temperature. This demonstration of the electrical detection of current-induced spins on the surface could enable the usage of TIs as polarized spin-current sources.

The investigation of these novel electronic materials provided a deeper insight, better device performance and also an outlook into the future of 2D spintronics. Our studies at room temperature demonstrated the creation of a large spin polarization in Si; that graphene is an excellent materials for long distance spin communication; h-BN exhibits good spin tunnel properties; MoS_2 can allow spin manipulation and transistor action; and Bi_2Se_3 possesses an electrically accessible current-induced spin polarization. Despite the novelty of most of these individual materials, we went even further by creating heterostructures, which elucidate the potential for future spintronic properties. Such heterostructures can employ the individual properties of their base materials or even reveal new properties at the interface, for example due to proximity effects. The ideal spin transport channel of graphene could be locally modified by bringing it into proximity with 2D SCs or TIs. The former could induce a strong SO coupling in graphene allowing for spin manipulation through an electric field, whereas the latter could exhibit a novel spin texture in graphene allowing for an intrinsic spin current generation without ferromagnets. Understanding, improving and combining 2D materials in novel spintronic devices could result in great advances for the whole field yielding new possibilities for the future of energy efficient spin-based memory and logic applications.

A

Microfabrication of spintronic devices

Micro- and nanofabrication is essential for studying spintronic phenomena, in particular on *two-dimensional* (2D) materials. *Non-magnetic materials* (NM) exhibit a short spin lifetime of up to several nanoseconds and an upper limit of the spin transport over only a few micrometer, which requires the fabrication of extremely short transport channels. Furthermore, many 2D materials are only grown in as bulk crystals and have to be mechanically cleaved to study the unique properties of their mono- or few-layer form. This results in microscopic and random positioned flakes, which have to be treated individually. Only micro- and nanofabrication techniques are precise and flexible enough to create devices, which can be used to investigate their spin properties.

This chapter collects the processes and recipes used to prepare the devices studied in this thesis. First, the lithography processes are introduced, which had to be adjusted and tested for 2D materials. Subsequently, we present important processes, which were adopted and calibrated for our fabrication. Finally, the process flow of each device presented in this thesis is described.

A.1 Lithography

The lithography recipes described in this section were adopted for our processes. The steps described here are specific for the Nanofabrication Laboratory in the Department of Microtechnology and Nanoscience at the Chalmers University of Technology. The tool numbers and names, specifications and parameters can vary and recipes may need to be adopted for other institutions.

The lithography recipes presented here are specifically adjusted and tested for 2D materials. Graphene and h-BN have been demonstrated to be thermally and chemically very robust. In contrast, several studies on 2D crystals, such as topological insulators and MoS_2, demonstrated a degradation of their intrinsic properties due to depletion or changes in the crystal structure at temperatures as low as 160 °C [206, 207]. This means, high temperature annealing processes should be avoided, but also limits the applicable resists and maximum temperature in the necessary steps significantly.

A.1.1 Photolithography

This *photolithography* (PL) recipe has been developed for the positive *photoresist* (PR) S1813. It can be used for a wide range of applications, such as wet etching with BHF, dry etching with Ar ion beam and for lift-off technique, which is useful for contacts and contact pads. The stability of the resist depends mainly on the backing time and structures above 1 μm can be exposed.

- Spin-coat HMDS at 3000 rpm for 1 min.
- Spin-coat S1813 at 3000 rpm for 1 min, bake at 90 °C for 2 min.
- Expose for 8.5 s at 6 mW/cm^2, "LowVac" mode in an MA6 mask aligner.
- Bake at 90 °C for 1 min.
- Develop for 1 min in MF319, rinse in *deionized* (DI) water and blow dry with N_2.
- Bake at 120 °C for 5 min if wet etching follows.

- Cleaning or lift-off can be done in warm acetone. Finally, rinse first with *isopropyl alcohol* (IPA) followed by DI water (optional) and blow dry with N_2.

A.1.2 Electron beam lithography for two-dimensional materials

This *electron beam lithography* (EBL) recipe has been adjusted for a low temperature baking of ZEP:Anisol 1:2[1] with an MMA "EL8" (8% solid in ethyl lactate) undercut resist. It can be used for lift-off of evaporated layers up to a thickness of 100 nm and for oxygen and argon plasma etching up to 1 min. For the lift-off of thicker layers, the undercut resist or spinning speed can be adjusted, so that the resulting thickness is about 50% greater than the intended deposition. Further, wet etching for up to 30 s in 2% HF and BHF is possible. Ozone and oxygen plasma have significantly higher etching rates for this resist combination compared to PR, which made the oxidation of a patterned substrate for several minutes impossible.

- Spin-coat MMA EL8 copolymer at 6000 rpm for 1 min, bake at 135 °C for 10 min. This results in an undercut layer thickness of 130 nm.

- Spin-coat ZEP:Anisol 1:2 or SX ARP 6200/2 1:1 at 6000 rpm for 1 min, bake at 135 °C for 10 min.

- Expose with electron beam at 100 kV in JEOL9300FS or with deep-UV light ($200 - 260$ nm wavelength, $3.6\,W/cm^2$) for 240 s

- Develop top-layer with hexyl acetat 99% for 33 s.

- Transfer directly to MIBK:IPA 1:1 for 135 s to develop undercut resist[2], blow dry with N_2 without rinsing.

- Cleaning or lift-off can be done in warm acetone. Finally, rinse first with IPA followed by DI water (optional) and blow dry with N_2.

[1] The resist SX ARP 6200/2 1:1 was recently introduced, but the recipe did not need any major adjustments.

[2] The development time of the undercut resist is reduced to 85 s when using SX ARP 6200/2 1:1 as top resist.

A.2 Processes

This section describes the main processes developed and used for the devices studied in this thesis. First, the preparation of an ozone oxidized SiO_2 tunnel barrier is described, as employed in Chapter 2. Subsequently, the exfoliation of flakes from bulk crystals and the transfer technique of CVD materials from a copper foil onto a substrate are introduced, which is crucial for the fabrication in Sections 2.3, 3.2, 3.3 and 4.3.

A.2.1 Silicon dioxide tunnel barrier by ozone oxidation

The oxidation of Si in a oxygen plasma or reactive ozone environment can create thin, homogeneous SiO_2 layers. They are relatively easy to control, require less time and do not affect the doping profile, in contrast to thermal oxidation [208]. However, plasma oxidation is usually performed at high energies, which can result in defects in the underlying Si and introduces scattering centres. Furthermore, ozone oxidation has been demonstrated to create a uniform, defect free SiO_2 layer [75].

We used a *ultraviolet* (UV) ozone chamber (FHR UVOH 150) to form the SiO_2, where ozone is created directly above the samples. A constant oxygen flow of 1000 sccm is ionized by an UV lamp to form ozone. The O_3 is highly reactive and oxidises the Si surface. The advantage in this particular machine is the close proximity of 4 mm between the O_3 creating UV lamp and the substrates, which ensures a uniform ozone concentration over the whole chip area (Figure A.3). This kind of Si oxidation was already studied by Niwano et al. in 1992 [75]. They found that within the first 5 s a about 5 Å thick oxide layer is formed. This oxide layer protects the Si surface against the environment, which decreases further oxidation drastically. The thickness continues to grow logarithmic resulting in about 7 Å after 40 s. A wider range of barrier thickness is desirable to study the tunnel barrier quality and its effect on the spin injection and detection process. To determine the oxide thickness, additional Si chips were oxidized along with the chips for the FM tunnel devices. The latter are used to study the spin accumulation and the junction resistance can be determined (Figure A.1a). The thermal SiO_2 on the chips for calibration was completely removed by BHF just before the ozone oxidation. Afterwards, the thickness of the oxide layer was measured with an ellipsometer (J.A. Woollam M2000). The resulting oxide thickness depending on the oxidation time is shown in Figure A.1b. The obtained data follow the trend of the measurement done by Niwano [75] and exhibit a logarithmic growth of the thickness of the

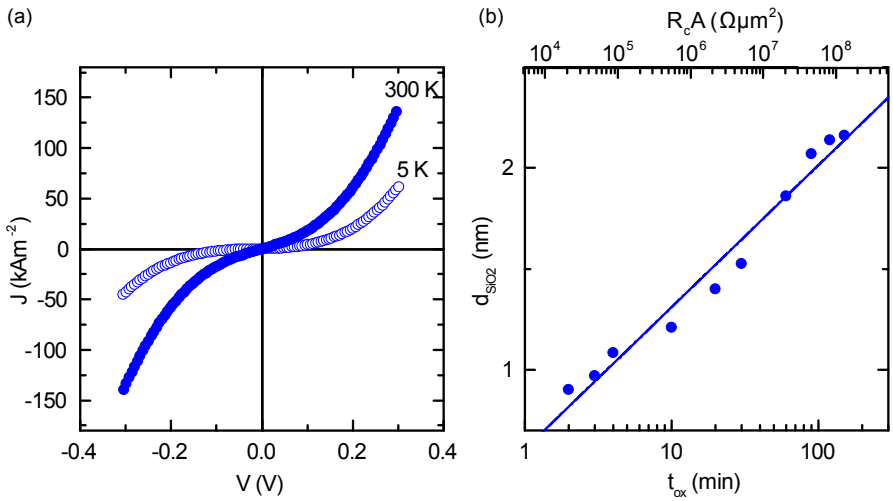

Figure A.1: Electrical properties of the ozone oxidised SiO_2 barrier. (a) IV characteristic for Co/SiO_2 tunnel contacts on highly doped Si at temperatures of 5 K and 300 K. (b) Oxidation time (t_{ox}) correlated with resulting SiO_2 barrier thickness (d_{SiO2}) and measured tunnel junction resistance (R_c). The thickness increases logarithmic with time and resistance, that means $R_c \propto t_{ox}$ and $R_c \propto \exp(d_{SiO2})$.

tunnel barrier up to an oxidation time of 3 h. Furthermore, the junction resistance of our devices correlates linearly with the oxidation time, which means that the resistance increases exponential with the oxide thickness; a clear indication of the good quality of the tunnel barrier.

This shows that our oxidation process with UV created ozone is able to create a uniform, pinhole free oxide layer up to 2 nm thickness, ranging the junction resistance area product from $10^4 - 10^8\,\Omega\mu\mathrm{m}^2$, which is excellent to study spin injection and detection in Si.

A.2.2 2D layered materials

Mono- or few-layers of 2D materials exhibit highly interesting and unique properties and can be fabricated by several techniques. Exfoliation from bulk crystals is by far the simplest technique and has been demonstrated for the first time with the discovery of graphene [80]. Even though this technique is versatile and produces high quality 2D material layers, it is only appropriate for research and not scalable for industrial applications.

The most promising scalable technique is the growth of thin layers of a 2D material on a metal catalyst by *chemical vapour deposition* (CVD). A

high temperatures furnace with a partial pressure controlled gas mixture can grow graphene or *hexagonal boron nitride* (h-BN) on a copper foil. The growth of graphene by CVD is limited to one layer, whereas for h-BN the number of layers depends on the growth conditions and time resulting in variations within the same sample. Once deposited on the copper foil the layers can be transferred to a desired substrate, where they can be further studied.

This section presents the transfer steps for both techniques, exfoliated and CVD grown material, as well as the possibilities to pattern 2D layers, which is in particular interesting for large scale fabrication.

A.2.2.1 Exfoliating 2D crystals

Mono- and few-layer flakes of 2D materials can be cleaved from bulk crystals by using a sticky tape (for example scotch tape). We obtained those bulk crystals commercially for several materials, such as Bi_2Se_3 from *Cradley Crystals*, MoS_2 from *SPI Supplies*, *black phosphorous* (BP) from *Smart Elements* and highly oriented pyrolytic graphite from *Advanced Ceramics*. Even though exfoliation is only interesting for research due to the limited scalability, this technique produces generally a higher quality of the flakes of wider range of 2D materials. Scalable techniques, such as CVD growth, are only available for a few materials, whereas exfoliation can be used for any layered material that exists as bulk crystal.

The crystal is cleaved once to transfer thick flakes of the material onto the tape. This is followed by multiple exfoliations from the tape, which increases the scattering and decreases the thickness of the flakes. Finally, the flakes are located optically and transferred by pressing onto the desired substrate, followed by carefully removing the tape. This technique results in a multitude of small, several micrometer sized flakes of various shapes. To identify appropriate flakes for further processing, an optical inspection is necessary.

We used commonly a Si substrate with 285 nm of SiO_2 top layer, which provides an optimal contrast to identify graphene and other 2D material flakes. The average thickness of the flakes depends strongly on the exfoliated material: Graphene flakes are generally several nanometres thick, whereby the thickness can easily be derived from the contrast of the flakes against the substrate and monolayers are commonly found on a single chip. MoS_2 and BP also exhibit a strong thickness dependent contrast, but monolayers are rare and the flake thickness ranges from $3 - 30$ nm. Bi_2Se_3 demonstrate almost no thickness dependence when studying optic-

ally, which makes an additional verification by atomic force microscopy necessary. Only Bi_2Se_3 flakes of less than 20 nm thickness exhibit a very low contrast compared to thicker flakes. Nevertheless, most of the materials demonstrate better electrical properties when using few-layer flakes, since the transport channel is better screened against the substrate. Furthermore, it has been shown that topological insulators even require a minimum thickness to form the topological surface state [209].

Finally, prefabricated location markers on the chip allow to determine the position of these flakes for further processing. Even though exfoliation is an excellent approach to investigate 2D materials, CVD growth progresses rapidly and has to be considered to make devices more accessible for actual applications.

A.2.2.2 Transfer of CVD grown materials

We obtained our CVD grown graphene and h-BN from *Graphenea* and *Graphene Supermarket*, respectively. Two-dimensional materials require a supporting substrate, which is the copper foil in the case of CVD grown materials. Performing electrical measurements on CVD grown materials requires usually a transfer from the conducting copper foil onto an insulating substrate. Usually, a supporting polymer is applied to stabilize the 2D layer while etching out the copper followed by the deposition on the target substrate before cleaning off the support polymer.

Initially, the h-BN is covered by MMA "EL8" (8% solid in Ethyl lactate) and PMMA copolymer, both followed by a baking at 135 °C for 10 min. We used such a double polymer layer to prevent contaminations of the 2D material layer by the PMMA copolymer. This is followed by 1 min argon or oxygen plasma etching at 50 W to remove any 2D material grown on the backside of the copper foil. Next, the copper is etched out in a H_2O_2:HCL:H_2O (1:1:8) solution for about 1 h. Afterwards, the etchant can be carefully drained and replaced by DI water. Finally, the layer can be transferred onto a substrate, by placing a chip inside the water bath under the 2D-material/polymer layer and draining the water carefully. It has to be mentioned that this process requires a substrate, which is resistant to water and oxidation. The chip with the polymer layer is dry baked at 135 °C for 10 min. The support polymer is removed in warm acetone for 15 min. Optionally, this can be followed by an annealing in an Ar/H_2 furnace at $200 - 500$ °C (for graphene and h-BN on SiO_2), which decreases the polymer residues even further.

Alternatively, we adopted a frame technique, which simplifies the hand-

ling of the 2D-material/polymer layer and allows a fast and dry transfer on any substrate material. Therefore, the initial Cu/2D-marerial/polymer stack is attached to a precut frame made of thermal tape (Figure A.2a). This increases the mechanical strength of the layer and enables for faster rinsing by DI water after the Cu etching. Before transferring the material

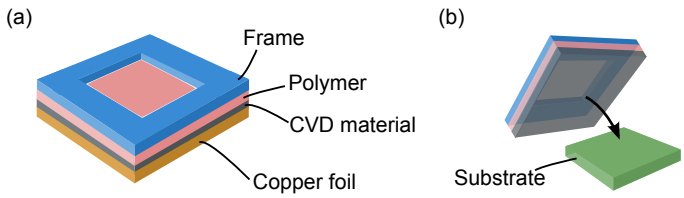

Figure A.2: Transfer of CVD grown materials using the frame technique. (a) Schematic of the final frame stacked with support polymer of the 2D material on a copper foil. (b) After etching out of the copper, the exposed 2D material can be transferred on the substrate.

onto the substrate, the water can be removed in IPA, which reduces the drying time and hence oxidation of the underlying substrate. The transfer can be executed in air. The frame can be carefully separated from the chip with a scalpel, before dry baking and cleaning of the chip as described above.

A.2.2.3 Patterning 2D materials

Both exfoliated flakes and layers of CVD grown 2D materials can or require to be patterned to create uniform transport channels, required device geometries or even nanowires. The desired device structure is protected by resist, which can be patterned by either PL (see Section A.1.1) or EBL (see Section A.1.2). Subsequently, an argon ion plasma can be used to mechanically dry etch any superfluous material. We used an argon plasma with an AC power of 50 W for 40 s to pattern h-BN, for example to confine it around graphene flakes (see Section A.3.3.1). Graphene has been patterned by oxidation in an oxygen plasma with an AC power of 50 W for 30 s.

A.3 Device fabrication

This section describes the process steps of all devices studied in this thesis. The large FM contacts and *magnetic tunnel junctions* (MTJ) in Chapter 2 were prepared by PL (see Section A.1.1), whereas EBL (see Section A.1.2)

allowed the flexibility and resolution required for the devices discussed in Chapter 3, 4 and 5.

A.3.1 Ferromagnetic tunnel contacts on Si

Silicon has an oxide, which is simple to produce and resistant against most chemicals, including water, and therefore used in processes compatible to the CMOS standard. Silicon directly exposed to air forms a natural oxide with a thickness of a few nanometres. This oxide is of a low quality and undesirable for most devices. Si wafers are prepared with a dry thermal oxide layer of 300 nm thickness. Furthermore, this thick thermal oxide allows to create well positioned electrical contacts to the Si with defined interfaces.

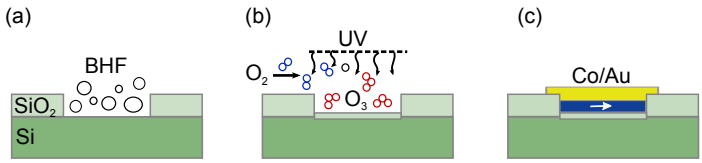

Figure A.3: Fabrication of a FM tunnel contacts with a ozone oxidized SiO_2 tunnel barrier. (a) Contact hole etching in buffered hydrofluoric acid (BHF). (b) Ozone oxidation: an oxygen flow of 1 $^{l}/_{min}$ is ionized by ultraviolet light and forms highly reactive ozone, which oxidises the Si surface. (c) Deposition of Co/Au contacts by photolithography (PL) and lift-off technique.

On such SiO_2/Si chips we define contact holes by PL, followed by etching of the SiO_2 with *buffered hydrofluoric acid* (BHF) with an etching rate for thermal SiO_2 of 95 nm/min (Figure A.3a). After cleaning the resist and the Si surface, the tunnel barrier is fabricated by oxidizing the Si (see Section A.2.1 and Figure A.3b). To provide a clean tunnel interface we covered the oxide barrier immediately by depositing the FM by electron beam evaporation of 15 nm Co with a 10 nm Au capping layer. A subsequent PL step defines the FM contacts around the contact holes, subsequently patterned by Ar ion beam etching (etching rate for Au is 7 nm/min and for Co is 2.3 nm/min at a DC power of 1.5 kW and an Ar flow of 3.5 sccm). Finally, large contact pads for wire bonding are defined by PL, followed by an electron beam evaporation of 10 nm Cr and 100 nm Au as well as lift-off (Figure A.3c).

A.3.2 Magnetic tunnel junctions

Magnetic tunnel junctions consist of a tunnel barrier material between two FM electrodes. They are an ideal tool to study the interface, which allowed us to study the spin tunnelling properties of h-BN. Initially the bottom

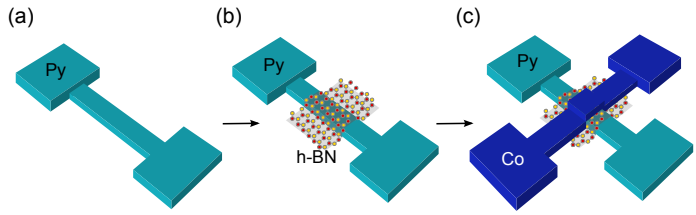

Figure A.4: NiFe/h-BN/Co magnetic tunnel junction fabrication. (a) Initially the 10 nm bottom FM electrode is patterned by PL and deposited by electron beam evaporation. (b) CVD grown h-BN is transferred and patterned to the centre of the device structure. (c) The 45 nm top FM electrode is patterned and deposited.

FM electrode of 10 nm Co or NiFe was patterned by PL on a SiO_2/Si substrate and deposited by electron beam evaporation, followed by a lift-off (Figure A.4a). Immediately after the lift off a layer of CVD grown h-BN is transferred onto the chip (see Section A.2.2.2). Since the h-BN reduces the adhesion of the top electrodes, it was patterned to the centre of the device structure (see Section A.2.2.3 and Figure A.4b). A top FM electrode of 45 nm Co was patterned by PL and deposited by electron beam evaporation, followed by a lift-off (Figure A.4c). Finally, contact pads of 10 nm Cr and 70 nm Au were patterned by PL and deposited by electron beam evaporation, followed by a lift-off.

A.3.3 Ferromagnetic contacts on 2D materials

2D materials are initially prepared on a SiO_2/Si substrate either by exfoliation (see Section A.2.2.1) or by patterning of transferred CVD grown materials (see Section A.2.2.2 and A.2.2.3). Generally, for studying the charge and spin transport, FM tunnel contacts can be patterned and deposited directly on the flakes (see Section A.3.3.3). This has been done for the devices fabricated directly on graphene (Section 3.1.1), CVD graphene (Section 3.2), Bi_2Se_3 (Chapter 5) and the lateral MoS_2 and BP FETs (Section 4.1). However, more complex heterostructures, such as graphene/h-BN (Section 3.3) and graphene/MoS_2 (Section 4.3), required several process steps.

A.3.3.1 Graphene/h-BN heterostructure

The graphene/h-BN heterostructure utilizes the insulating property of h-BN as tunnel barrier between graphene and the FM contact. First, graphene is exfoliated onto a SiO_2/Si substrate and appropriate flakes for the device fabrication were identified by optical microscopy (Figure A.5a). Subsequently, CVD grown h-BN was transferred on top of the graphene flakes. Since the h-BN reduced the adhesion of the deposited metal contacts, we patterned it to be confined around the graphene flakes (Figure A.5b). Finally, FM contacts were prepared on top of the graphene/h-BN structure (Figure A.5c).

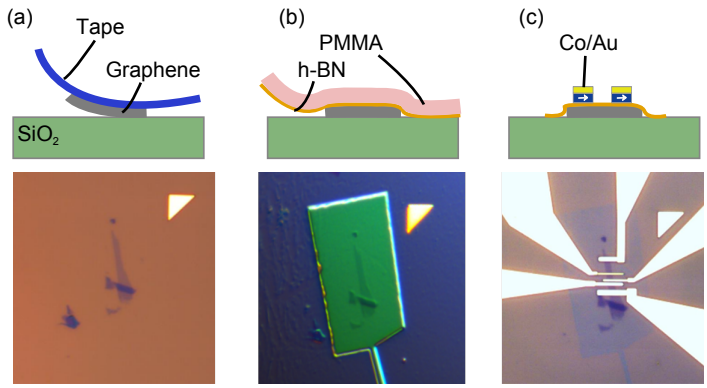

Figure A.5: Graphene/h-BN/FM device fabrication. (a) Schematic (top) and micrograph (bottom) of graphene transferred on SiO_2 substrate by cleavage technique. (b) Schematic of transferring h-BN with PMMA copolymer onto the graphene and substrate (top); Micrograph of the h-BN on top of the graphene after patterning with Ar ion etching (bottom). (c) Schematic (top) and micrograph (bottom) of FM/Au contacts prepared by EBL, electron beam evaporation and lift-off.

A.3.3.2 Graphene/MoS_2 heterostructure

The graphene/MoS_2 heterostructure is used to study a MoS_2 FET with a short channel length between a FM electrode and the graphene channel, defined by the thickness of the MoS_2 flake. First, CVD graphene was transferred onto a SiO_2/Si substrate. Next, it was patterned by PL into an array of stripes with lengths of $50\,\mu$m and widths of $1-3\,\mu$m in a distance of $10\,\mu$m on the whole chip (Figure A.3.3.2a). This ensures, that the subsequent exfoliation results randomly in a MoS_2 flake on top of a graphene stripe. Such appropriate flakes for the device fabrication were identified by optical microscopy (Figure A.3.3.2b). Finally, FM tunnel

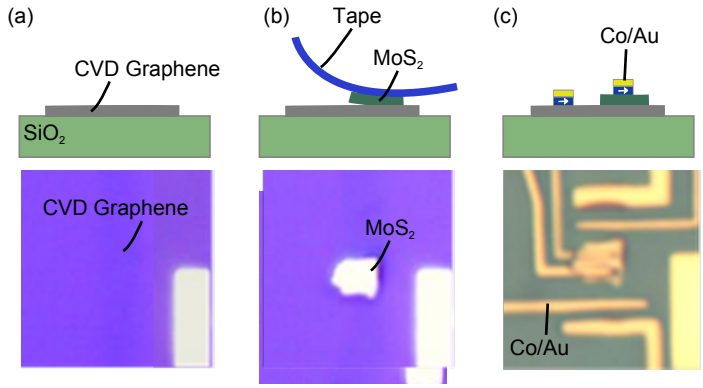

Figure A.6: Graphene/MoS_2 device fabrication. (a) Schematic (top) and micrograph (bottom) of a patterned CVD graphene channel on SiO_2 substrate. (b) Schematic of the exfoliation of MoS_2 onto the graphene stripe (top); Micrograph of the MoS_2 flake on top of the graphene (bottom). (c) Schematic (top) and micrograph (bottom) of FM/Au contacts prepared by EBL, electron beam evaporation and lift-off.

contacts were prepared so that some only connect to the MoS_2 flake, and others only contact the graphene stripe (Figure A.5c).

A.3.3.3 Preparation of ferromagnetic tunnel contacts

A metal oxide tunnel barrier can be deposited either before or after the EBL. Therefore, we deposited a thin metal layer (8 Å Ti) and oxidise it in air for 30 s resulting in an about 1 nm thick oxide layer. Alternatively, 1 nm of TiO_2 could be produced by sputtering Ti for 3 s in a FHR MS150 sputtering machine in presence of a flow of 40 sccm of Ar and 4 sccm of oxygen. Subsequently, EBL is used to expose a computer aided design of the desired contact configuration, which enables for contact sizes below 100 nm and a flexible mask design for each chip. The latter is in particular required for exfoliated flakes, which are randomly scattered on the substrate. The FM contacts are designed with an introduced discontinuity along the lead yielding a domain wall formation and allows the contact magnetization to be independent of their bonding pad magnetization. This enabled us to fabricate FM contacts on the 2D materials and their contact pads in a single lithography and deposition step. After the EBL 65 nm Co and 20 nm Au are deposited by electron beam evaporation, followed by a lift off in warm acetone.

Bibliography

[1] I. Žutić *et al.* Spintronics: Fundamentals and applications. *Rev. Mod. Phys.* **76**, 323 (2004).

[2] D. Awschalom & M. Flatté. Challenges for semiconductor spintronics. *Nat. Phys.* **3**, 40 (2007).

[3] H. Dery & H. Wu. Reconfigurable nanoelectronics using graphene based spintronic logic gates. *SPIE* **8100** (2011).

[4] N. Mott. The resistance and thermoelectric properties of the transition metals. *Proc. R. Soc. London* **147**, 368 (1936).

[5] N. Mott. The electrical conductivity of transition metals. *Proc. R. Soc. London* **153**, 699 (1936).

[6] M. Baibich *et al.* Giant magnetoresistance of (001) Fe/(001) Cr magnetic superlattices. *Phys. Rev. Lett.* **61**, 2472 (1988).

[7] J. S. Moodera *et al.* Large magnetoresistance at room temperature in ferromagnetic thin film tunnel junctions. *Phys. Rev. Lett.* **74**, 3273 (1995).

[8] A. Aronov. Spin injection in metals and polarization of nuclei. *JETP Lett.* **24**, 37 (1976).

[9] M. Johnson & R. Silsbee. Thermodynamic analysis of interfacial transport and of the thermomagnetoelectric system. *Phys. Rev. B.* **35**, 4959 (1987).

[10] G. Lampel. Nuclear dynamic polarization by optical electronic saturation and optical pumping in semiconductors. *Phys. Rev. Lett.* **20**, 6 (1968).

[11] B. T. Jonker *et al.* Electrical spin-injection into silicon from a ferromagnetic metal/tunnel barrier contact. *Nat. Phys.* **3**, 542 (2007).

[12] B. Behin-Aein *et al.* Proposal for an all-spin logic device with built-in memory. *Nat. Nanotechnol.* **5**, 266 (2010).

[13] S. Datta & B. Das. Electronic analog of the electro-optic modulator. *Appl. Phys. Lett.* **56**, 665 (1990).

[14] F. Jedema *et al.* Electrical spin injection in metallic mesoscopic spin valves. *Lett. Nat.* **410**, 345 (2002).

[15] S. O. Valenzuela & M. Tinkham. Direct electronic measurement of the spin Hall effect. *Nature* **442**, 176 (2006).

[16] O. M. J. van 't Erve *et al.* Comparison of Fe/Schottky and Fe/Al_2O_3 tunnel barrier contacts for electrical spin injection into GaAs. *Appl. Phys. Lett.* **84**, 4334 (2004).

[17] K. Yoh *et al.* Spin injection from a ferromagnetic electrode into InAs surface inversion layer. *J. Cryst. Growth* **251**, 337 (2003).

[18] S. P. Dash *et al.* Electrical Creation of Spin Polarization in Silicon at Room Temperature. *Nature* **462**, 491 (2009).

[19] P. Bruski *et al.* All-electrical spin injection and detection in the Co_2FeSi/GaAs hybrid system in the local and non-local configuration. *Appl. Phys. Lett.* **103**, 052406 (2013).

[20] K. Hamaya *et al.* Room-temperature electrical creation of spin accumulation in n-Ge using highly resistive Fe_3Si/n+Ge Schottky-tunnel contacts. *Thin Solid Films* **557**, 382 (2014).

[21] C. Ertler *et al.* Electron spin relaxation in graphene: The role of the substrate. *Phys. Rev. B* **80**, 041405 (2009).

[22] A. K. Geim & I. V. Grigorieva. Van der Waals Heterostructures. *Nature* **499**, 419 (2013).

[23] P. Zomer *et al.* Long-Distance Spin Transport in High-Mobility Graphene on Hexagonal Boron Nitride. *Phys. Rev. B* **86**, 161416 (2012).

[24] L. Hu & G. Gruner. Touch screen devices employing nanostructure networks. *US Pat. App.* **11/552,834** (2013).

[25] S. Das *et al.* All Two-Dimensional, Flexible, Transparent, and Thinnest Thin Film Transistor. *Nano Lett.* (2014).

[26] O. Txoperena & M. Gobbi. How reliable are Hanle measurements in metals in a three-terminal geometry? *arXiv* 17–21 (2012).

[27] W. Han *et al.* Graphene spintronics. *Nat. Nanotechnol.* **9**, 794 (2014).

[28] R. Jansen *et al.* Silicon spintronics with ferromagnetic tunnel devices. *Semicond. Sci. Technol.* **27**, 083001 (2012).

[29] Q. Wu *et al.* Efficient Spin Injection into Graphene through a Tunnel Barrier: Overcoming the Spin-Conductance Mismatch. *Phys. Rev. Appl.* **2**, 044008 (2014).

[30] B. W. H. Baugher *et al.* Intrinsic electronic transport properties of high-quality monolayer and bilayer MoS_2. *Nano Lett.* **13**, 4212 (2013).

[31] C. Li *et al.* Electrical detection of charge-current-induced spin polarization due to spin-momentum locking in Bi_2Se_3. *Nat. Nanotechnol.* **9**, 218 (2014).

[32] D. Wei *et al.* The spin Hall effect as a probe of nonlinear spin fluctuations. *Nat. Commun.* **3**, 1058 (2012).

[33] H. Tetlow & M. Gradhand. Semiconductor spintronics: Tuning the spin Hall effect in Si. *Phys. Rev. B* **87**, 075206 (2013).

[34] J.-Y. Chen *et al.* Self-polarized spin-nanolasers. *Nat. Nanotechnol.* **9**, 845 (2014).

[35] A. Fert & H. Jaffrès. Conditions for Efficient Spin Injection from a Ferromagnetic Metal into a Semiconductor. *Phys. Rev. B* **64**, 184420 (2001).

[36] N. Tombros *et al.* Electronic Spin Transport and Spin Precession in Single Graphene Layers at Room Temperature. *Nature* **448**, 571 (2007).

[37] A. Fert & I. Campbell. Two-current conduction in nickel. *Phys. Rev. Lett.* (1968).

[38] T. Valet & A. Fert. Theory of the perpendicular magnetoresistance in magnetic multilayers. *Phys. Rev. B* **48**, 7099 (1993).

[39] R. J. Soulen Jr. Measuring the Spin Polarization of a Metal with a Superconducting Point Contact. *Science* **282**, 85 (1998).

[40] M. Julliere. Tunneling between ferromagnetic films. *Phys. Lett. A* **54**, 225 (1975).

[41] M. Wojtaszek *et al.* Absence of hyperfine effects in $^{1}3$C-graphene spin-valve devices. *Phys. Rev. B* **89**, 035417 (2014).

[42] P. V. Son *et al.* Boundary resistance of the ferromagnetic-nonferromagnetic metal interface. *Phys. Rev. Lett.* **58**, 2271 (1987).

[43] I. Appelbaum *et al.* Electronic measurement and control of spin transport in silicon. *Nature* **447**, 295 (2007).

[44] H. Man & A. F. Morpurgo. Sample-Specific and Ensemble-Averaged Magnetoconductance of Individual Single-Wall Carbon Nanotubes. *Phys. Rev. Lett.* **95**, 026801 (2005).

[45] K. Ono *et al.* Spin polarization and magneto-Coulomb oscillations in ferromagnetic single electron devices. *J. Phys. Soc. Japan* **67**, 2852 (1998).

[46] W. Hanle. Über magnetische Beeinflussung der Polarisation der Resonanzfluoreszenz. *Zeitschrift für Phys.* **30**, 93 (1924).

[47] X. Lou *et al.* Electrical Detection of Spin Accumulation at a Ferromagnet-Semiconductor Interface. *Phys. Rev. Lett.* **96**, 176603 (2006).

[48] M. Tran *et al.* Enhancement of the Spin Accumulation at the Interface between a Spin-Polarized Tunnel Junction and a Semiconductor. *Phys. Rev. Lett.* **102**, 036601 (2009).

[49] R. Jansen. Silicon spintronics. *Nat. Mater.* **11**, 400 (2012).

[50] A. A. Burkov & D. G. Hawthorn. Spin and Charge Transport on the Surface of a Topological Insulator. *Phys. Rev. Lett.* **105**, 066802 (2010).

[51] L. Liu *et al.* Spin-Polarized Tunneling Study on Spin-Momentum Locking in the Topological Insulator Bismuth Selenide. *arXiv:1410.7494* (2014).

[52] D. Qu *et al.* Quantum oscillations and Hall anomaly of surface states in the topological insulator Bi_2Te_3. *Science* **329**, 821 (2010).

[53] F. Qu *et al.* Coexistence of Bulk and Surface Shubnikov-de Haas Oscillations in Bi_2Se_3. *J. Low Temp. Phys.* **170**, 397 (2012).

[54] D. Pesin & A. H. MacDonald. Spintronics and pseudospintronics in graphene and topological insulators. *Nat. Mater.* **11**, 409 (2012).

[55] S. Hikami *et al.* Spin-orbit interaction and magnetoresistance in the two dimensional random system. *Prog. Theor. Phys.* **63**, 707 (1980).

[56] A. M. R. Baker *et al.* Weak localization scattering lengths in epitaxial, and CVD graphene. *Phys. Rev. B* **86**, 235441 (2012).

[57] S. Matsuo *et al.* Weak antilocalization and conductance fluctuation in a submicrometer-sized wire of epitaxial Bi_2Se_3. *Phys. Rev. B* **85**, 075440 (2012).

[58] S. Sze & K. Ng. *Physics of semiconductor devices.* John Wiley & Sons, Inc. ISBN 0471143235 (2006).

[59] S. Das *et al.* High Performance Multilayer MoS_2 Transistors with Scandium Contacts. *Nano Lett.* **13**, 100 (2013).

[60] J.-R. Chen *et al.* Control of Schottky Barriers in Single Layer MoS_2 Transistors with Ferromagnetic Contacts. *Nano Lett.* **13**, 3106 (2013).

[61] K. Kasahara *et al.* Spin accumulation created electrically in an n-type germanium channel using Schottky tunnel contacts. *J. Appl. Phys.* **111**, 07C503 (2012).

[62] Y. Cui *et al.* Doping and Electrical Transport in Silicon Nanowires. *J. Phys. Chem. B* **104**, 5213 (2000).

[63] J. Tarun *et al.* Demonstration of spin valve effects in silicon nanowires. *J. Appl. Phys.* **109**, 07C508 (2011).

[64] J. Gao & J. Zhao. Initial geometries, interaction mechanism and high stability of silicene on Ag(111) surface. *Sci. Rep.* **2**, 861 (2012).

[65] O. M. J. van 't Erve *et al.* Electrical injection and detection of spin-polarized carriers in silicon in a lateral transport geometry. *Appl. Phys. Lett.* **91**, 212109 (2007).

[66] C. H. Li *et al.* Electrical injection and detection of spin accumulation in silicon at 500 K with magnetic metal/silicon dioxide contacts. *Nat. Commun.* **2**, 245 (2011).

[67] K. Jeon *et al.* Electrical spin accumulation with improved bias voltage dependence in a crystalline CoFe/MgO/Si system. *Appl. Phys. Lett.* **98**, 262102 (2011).

[68] O. M. J. van 't Erve *et al.* A graphene solution to conductivity mismatch: Spin injection from ferromagnetic metal/graphene tunnel contacts into silicon. *J. Appl. Phys.* **113**, 17C502 (2013).

[69] O. Txoperena *et al.* How reliable are Hanle measurements in metals in a three-terminal geometry? *Appl. Phys. Lett.* **102**, 192406 (2013).

[70] O. Txoperena *et al.* Impurity-Assisted Tunneling Magnetoresistance under a Weak Magnetic Field. *Phys. Rev. Lett.* **113**, 146601 (2014).

[71] S. Sharma *et al.* Anomalous scaling of spin accumulation in ferromagnetic tunnel devices with silicon and germanium. *Phys. Rev. B* **89**, 075301 (2014).

[72] T. Sasaki *et al.* Comparison of spin signals in silicon between nonlocal four-terminal and three-terminal methods. *Appl. Phys. Lett.* **98**, 012508 (2011).

[73] M. Shiraishi *et al.* Spin transport properties in silicon in a nonlocal geometry. *Phys. Rev. B* **83**, 241204 (2011).

[74] T. Sasaki *et al.* Local magnetoresistance in Fe/MgO/Si lateral spin valve at room temperature. *arXiv:1401.1279* (2014).

[75] M. Niwano & M. Suemitsu. Ultraviolet ozone oxidation of Si surface studied by photoemission and surface infrared spectroscopy. *J. Vac. Sci. Technol. A* **10**, 3171 (1992).

[76] A. L. Friedman *et al.* Homoepitaxial tunnel barriers with functionalized graphene-on-graphene for charge and spin transport. *Nat. Commun.* **5**, 1 (2014).

[77] L. Britnell *et al.* Electron tunneling through ultrathin boron nitride crystalline barriers. *Nano Lett.* **12**, 1707 (2012).

[78] M. J. Allen *et al.* Honeycomb Carbon : A Review of Graphene. *Rev. Lit. Arts Am.* **110**, 132 (2010).

[79] T. Ando. Exotic electronic and transport properties of graphene. *Phys. E* **40**, 213 (2007).

[80] K. S. Novoselov *et al.* Electric field effect in atomically thin carbon films. *Science* **306**, 666 (2004).

[81] N. Tombros. *Electron spin transport in graphene and carbon nanotubes.* Ph.D. thesis, Rijksuniversiteit Gröningen (2008).

[82] M. B. Lundeberg *et al.* Defect-Mediated Spin Relaxation and Dephasing in Graphene. *Phys. Rev. Lett.* **110**, 156601 (2013).

[83] B. J. van Wees. *Overview on Carbon Spintronics.* Taylor Francis Group, LLC (2012).

[84] M. H. D. Guimarães *et al.* Spin transport in high-quality suspended graphene devices. *Nano Lett.* **12**, 3512 (2012).

[85] I. Neumann *et al.* Electrical detection of spin precession in freely suspended graphene spin valves on cross-linked poly(methyl methacrylate). *Small* **9**, 156 (2013).

[86] C. R. Dean *et al.* Boron nitride substrates for high-quality graphene electronics. *Nat. Nanotechnol.* **5**, 722 (2010).

[87] H. Idzuchi *et al.* Effect of anisotropic spin absorption on the Hanle effect in lateral spin valves. *Phys. Rev. B* **89**, 081308 (2014).

[88] H. Idzuchi *et al.* Revisiting the measurement of the spin relaxation time in graphene-based devices. *arXiv:1411.2949* (2014).

[89] D. Kochan *et al.* Spin Relaxation Mechanism in Graphene: Resonant Scattering by Magnetic Impurities. *Phys. Rev. Lett.* **112**, 116602 (2014).

[90] X. Li *et al.* Chemically Derived, Ultrasmooth Graphene Nanoribbon Semiconductors. *Science* **319**, 1229 (2008).

[91] K. Liu *et al.* Evolution of interlayer coupling in twisted molybdenum disulfide bilayers. *Nat. Commun.* **5**, 4966 (2014).

[92] A. Piñeiro *et al.* Fermiology and magnetism in weak itinerant ferromagnet CoS2: an ab initio study. *J. Phys. Condens. Matter* **22**, 505602 (2010).

[93] B. Radisavljevic *et al.* Single-Layer MoS_2 Transistors. *Nat. Nanotechnol.* **6**, 147 (2011).

[94] J. T. Ye *et al.* Superconducting dome in a gate-tuned band insulator. *Science* **338**, 1193 (2012).

[95] A. Kuc *et al.* Influence of quantum confinement on the electronic structure of the transition metal sulfide TS_2. *Phys. Rev. B* **83**, 245213 (2011).

[96] D. Xiao *et al.* Coupled Spin and Valley Physics in Monolayers of MoS_2 and Other Group-VI Dichalcogenides. *Phys. Rev. Lett.* **108**, 196802 (2012).

[97] K. F. Mak *et al.* Control of Valley Polarization in Monolayer MoS_2 by Optical Helicity. *Nat. Nanotechnol.* **7**, 494 (2012).

[98] H. Ochoa & R. Roldán. Spin-orbit-mediated spin relaxation in monolayer MoS_2. *Phys. Rev. B* **87**, 245421 (2013).

[99] B. Radisavljevic & A. Kis. Mobility Engineering and Metal-Insulator Transition in Monolayer MoS_2. *Nat. Mater.* **12**, 815 (2013).

[100] W. Liu *et al.* Role of metal contacts in designing high-performance monolayer n-type WSe_2 field effect transistors. *Nano Lett.* **13**, 1983 (2013).

[101] W. Bao *et al.* High mobility ambipolar MoS_2 field-effect transistors: Substrate and dielectric effects. *Appl. Phys. Lett.* **102**, 042104 (2013).

[102] A. Allain & A. Kis. Electron and Hole Mobilities in Single-Layer WSe_2. *ACS Nano* (2014).

[103] S. Das & J. Appenzeller. Where Does the Current Flow in Two-Dimensional Layered Systems? *Nano Lett.* (2013).

[104] S. Kim *et al.* High-mobility and low-power thin-film transistors based on multilayer MoS2 crystals. *Nat. Commun.* **3**, 1011 (2012).

[105] Z.-Y. Ong & M. V. Fischetti. Mobility enhancement and temperature dependence in top-gated single-layer MoS_2. *Phys. Rev. B* **88**, 165316 (2013).

[106] G. Schmidt *et al.* Fundamental Obstacle for Electrical Spin Injection from a Ferromagnetic Metal into a Diffusive Semiconductor. *Phys. Rev. B* **62**, R4790 (2000).

[107] X. Lou *et al.* Electrical Detection of Spin Transport in Lateral Ferromagnet-Semiconductor Devices. *Nat. Phys.* **3**, 197 (2007).

[108] W. Han *et al.* Electron-Hole Asymmetry of Spin Injection and Transport in Single-Layer Graphene. *Phys. Rev. Lett.* **102**, 137205 (2009).

[109] V. Tran *et al.* Layer-Controlled Band Gap and Anisotropic Excitons in Phosphorene. *arXiv:1402.4192* (2014).

[110] H. Liu *et al.* Phosphorene: An Unexplored 2D Semiconductor with a High Hole Mobility. *ACS Nano* **8**, 4033 (2014).

[111] J. Dai & X. Zeng. Bilayer Phosphorene: Effect of Stacking Order on Bandgap and Its Potential Applications in Thin-Film Solar Cells. *J. Phys. Chem. Lett.* **5**, 1289 (2014).

[112] P. Bridgman. Two new modifications of phosphorus. *J. Am. Chem. Soc.* **36**, 1344 (1914).

[113] R. Keyes. The electrical properties of black phosphorus. *Phys. Rev.* **92** (1953).

[114] L. Li *et al.* Black phosphorus field-effect transistors. *Nat. Nanotechnol.* **9**, 372 (2014).

[115] F. Xia *et al.* Rediscovering Black Phosphorus: A Unique Anisotropic 2D Material for Optoelectronics and Electronics. *arXiv:1402.0270* (2014).

[116] S. P. Koenig *et al.* Electric field effect in ultrathin black phosphorus. *Appl. Phys. Lett.* **104**, 103106 (2014).

[117] S. Das *et al.* Ambipolar Phosphorene Field Effect Transistor. *ACS Nano* **8**, 11730 (2014).

[118] R. J. Warburton. Single spins in self-assembled quantum dots. *Nat. Mater.* **12**, 483 (2013).

[119] A. Abragam & M. Goldman. Principles of dynamic nuclear polarisation. *Reports Prog. Phys.* **41**, 395 (1978).

[120] Y. Ando. Topological Insulator Materials. *J. Phys. Soc. Japan* **82**, 102001 (2013).

[121] K. Klitzing *et al.* New method for high-accuracy determination of the fine-structure constant based on quantized Hall resistance. *Phys. Rev. Lett.* **45**, 494 (1980).

[122] B. Halperin. Quantized Hall conductance, current-carrying edge states, and the existence of extended states in a two-dimensional disordered potential. *Phys. Rev. B* **25**, 2185 (1982).

[123] S. Wolf *et al.* Spintronics: a spin-based electronics vision for the future. *Science* **294**, 1488 (2001).

[124] S. Murakami *et al.* Spin-Hall Insulator. *Phys. Rev. Lett.* **93**, 156804 (2004).

[125] M. Onoda & N. Nagaosa. Spin Current and Accumulation Generated by the Spin Hall Insulator. *Phys. Rev. Lett.* **95**, 106601 (2005).

[126] C. L. Kane & E. J. Mele. Quantum Spin Hall Effect in Graphene. *Phys. Rev. Lett.* **95**, 226801 (2005).

[127] B. Bernevig *et al.* Quantum spin Hall effect and topological phase transition in HgTe quantum wells. *Science* **314**, 1757 (2006).

[128] M. König *et al.* Quantum spin hall insulator state in HgTe quantum wells. *Science* **318**, 766 (2007).

[129] L. Fu *et al.* Topological Insulators in Three Dimensions. *Phys. Rev. Lett.* **98**, 106803 (2007).

[130] Z. Ren *et al.* Optimizing $Bi_{2-x}Sb_xTe_{3-y}Se_y$ solid solutions to approach the intrinsic topological insulator regime. *Phys. Rev. B* **84**, 165311 (2011).

[131] Y. Ando *et al.* Electrical detection of the spin polarization due to charge flow in the surface state of the topological insulator $Bi_{1.5}Sb_{0.5}Te_{1.7}Se_{1.3}$. *Nano Lett.* **14**, 6226 (2014).

[132] Y. Xu *et al.* Observation of topological surface state quantum Hall effect in an intrinsic three-dimensional topological insulator. *Nat. Phys.* **10**, 956 (2014).

[133] D. Hsieh *et al.* A tunable topological insulator in the spin helical Dirac transport regime. *Nature* **460**, 1101 (2009).

[134] Z.-H. Pan *et al.* Electronic Structure of the Topological Insulator Bi_2Se_3 Using Angle-Resolved Photoemission Spectroscopy: Evidence for a Nearly Full Surface Spin Polarization. *Phys. Rev. Lett.* **106**, 257004 (2011).

[135] A. R. Mellnik *et al.* Spin-transfer torque generated by a topological insulator. *Nature* **511**, 449 (2014).

[136] Y. Shiomi *et al.* Bulk topological insulators as inborn spintronics detectors. *arXiv:1312.7091* (2013).

[137] P. Deorani *et al.* Observation of inverse spin Hall effect in bismuth selenide. *Phys. Rev. B* **90**, 094403 (2014).

[138] J. Tian *et al.* Topological insulator based spin valve devices: Evidence for spin polarized transport of spin-momentum-locked topological surface states. *Solid State Commun.* **191**, 1 (2014).

[139] J. Tang *et al.* Electrical Detection of Spin-Polarized Surface States Conduction in $(Bi_0.53Sb_0.47)_2Te_3$ Topological Insulator. *Nano Lett.* **14**, 5423 (2014).

[140] C. Brüne *et al.* Evidence for the ballistic intrinsic spin Hall effect in HgTe nanostructures. *Nat. Phys.* **6**, 448 (2010).

[141] M. Z. Hasan & C. Kane. Colloquium: topological insulators. *Rev. Mod. Phys.* **82**, 3045 (2010).

[142] P. Sutter & E. Sutter. Thickness determination of few-layer hexagonal boron nitride films by scanning electron microscopy and Auger electron spectroscopy. *APL Mater.* **2**, 092502 (2014).

[143] M. Engler *et al.* Hexagonal Boron Nitride (hBN): Applications from Metallurgy to Cosmetics. *Ceram. forum Int.* 49–53 (2007).

[144] O. Hod. Graphite and hexagonal boron-nitride have the same interlayer distance. Why? *J. Chem. Theory Comput.* **8**, 1630 (2012).

[145] G. Lee *et al.* Flexible and Transparent MoS_2 Field-Effect Transistors on Hexagonal Boron Nitride-Graphene Heterostructures. *ACS Nano* **7**, 7931 (2013).

[146] L. Wang *et al.* One-dimensional electrical contact to a two-dimensional material. *Science* **342**, 614 (2013).

[147] M. W. Iqbal *et al.* Superior characteristics of graphene field effect transistor enclosed by chemical-vapor-deposition-grown hexagonal boron nitride. *J. Mater. Chem. C* **2**, 7776 (2014).

[148] A. S. Mayorov *et al.* Micrometer-scale ballistic transport in encapsulated graphene at room temperature. *Nano Lett.* **11**, 2396 (2011).

[149] M. Drögeler *et al.* Nanosecond spin lifetimes in single-and few-layer graphene-hBN heterostructures at room temperature. *Nano Lett.* **14**, 6050 (2014).

[150] M. H. D. Guimarães *et al.* Controlling Spin Relaxation in Hexagonal BN-Encapsulated Graphene with a Transverse Electric Field. *Phys. Rev. Lett.* **113**, 086602 (2014).

[151] G. Lee *et al.* Electron tunneling through atomically flat and ultrathin hexagonal boron nitride. *Appl. Phys. Lett.* **99**, 243114 (2011).

[152] W. Yang *et al.* Epitaxial growth of single-domain graphene on hexagonal boron nitride. *Nat. Mater.* **12**, 792 (2013).

[153] S. Tang *et al.* Precisely aligned graphene grown on hexagonal boron nitride by catalyst free chemical vapor deposition. *Sci. Rep.* **3**, 2666 (2013).

[154] T. Sasaki *et al.* Evidence of electrical spin injection into silicon using MgO tunnel barrier. *IEEE Trans. Magn.* **46**, 1436 (2010).

[155] F. Werner *et al.* Electronic and chemical properties of the c-Si/Al_2O_3 interface. *J. Appl. Phys.* **109**, 113701 (2011).

[156] P. Gray & D. Brown. Density of SiO_2/Si interface states. *Appl. Phys. Lett.* **8**, 31 (1966).

[157] C. Guite & V. Venkataraman. Temperature dependence of spin lifetime of conduction electrons in bulk germanium. *Appl. Phys. Lett.* **101**, 252404 (2012).

[158] S. P. Dash *et al.* Spin precession and inverted Hanle effect in a semiconductor near a finite-roughness ferromagnetic interface. *Phys. Rev. B* **84**, 054410 (2011).

[159] C. Shang *et al.* Temperature dependence of magnetoresistance and surface magnetization in ferromagnetic tunnel junctions. *Phys. Rev. B* **58**, R2917 (1998).

[160] R. Jansen. Viewpoint: Holes in Silicon Hold On to Their Spin. *Physics (College. Park. Md).* **6**, 33 (2013).

[161] J. Bardeen. Surface States and Rectification at a Metal Semi-Conductor Contact. *Phys. Rev.* **71**, 717 (1947).

[162] R. Jansen & B.-C. Min. Detection of a Spin Accumulation in Nondegenerate Semiconductors. *Phys. Rev. Lett.* **99**, 246604 (2007).

[163] H. Dery & L. Sham. Spin Extraction Theory and Its Relevance to Spintronics. *Phys. Rev. Lett.* **98**, 046602 (2007).

[164] G. Salis *et al.* Spin-injection spectra of CoFe/GaAs contacts: Dependence on Fe concentration, interface, and annealing conditions. *Phys. Rev. B* **84**, 041307 (2011).

[165] K.-R. Jeon *et al.* Unconventional Hanle effect in a highly ordered CoFe/MgO/ n -Si contactt: non-monotonic bias and temperature dependence and sign inversion of the spin signal. *New J. Phys.* **14**, 023014 (2012).

[166] R. Jansen *et al.* Injection and detection of spin in a semiconductor by tunneling via interface states. *Phys. Rev. B* **85**, 134420 (2012).

[167] S. Parkin *et al.* Giant tunnelling magnetoresistance at room temperature with MgO (100) tunnel barriers. *Nat. Mater.* **3**, 862 (2004).

[168] S. Yuasa *et al.* Giant room-temperature magnetoresistance in single-crystal Fe/MgO/Fe magnetic tunnel junctions. *Nat. Mater.* **3**, 868 (2004).

[169] K. S. Novoselov *et al.* A Roadmap for Graphene. *Nature* **490**, 192 (2012).

[170] I. Appelbaum *et al.* Self-consistent model of spin accumulation magnetoresistance in ferromagnet/insulator/semiconductor tunnel junctions. *Phys. Rev. B* **90**, 220402 (2014).

[171] X. Li *et al.* Transfer of large-area graphene films for high-performance transparent conductive electrodes. *Nano Lett.* **9**, 4359 (2009).

[172] S. Roche & S. O. Valenzuela. Graphene spintronics: puzzling controversies and challenges for spin manipulation. *J. Phys. D. Appl. Phys.* **47**, 094011 (2014).

[173] W. Fu *et al.* Large-scale fabrication of BN tunnel barriers for graphene spintronics. *J. Appl. Phys.* **116**, 074306 (2014).

[174] W. Han *et al.* Tunneling Spin Injection into Single Layer Graphene. *Phys. Rev. Lett.* **105**, 167202 (2010).

[175] W. Han & R. K. Kawakami. Spin Relaxation in Single-Layer and Bilayer Graphene. *Phys. Rev. Lett.* **107**, 047207 (2011).

[176] L. Song *et al.* Large scale growth and characterization of atomic hexagonal boron nitride layers. *Nano Lett.* **10**, 3209 (2010).

[177] J. Xue *et al.* Scanning tunnelling microscopy and spectroscopy of ultra-flat graphene on hexagonal boron nitride. *Nat. Mater.* **13**, 4 (2011).

[178] S. Takahashi & S. Maekawa. Spin injection and detection in magnetic nanostructures. *Phys. Rev. B* **67**, 052409 (2003).

[179] W. Han *et al.* Spin transport and relaxation in graphene. *J. Magn. Magn. Mater.* **324**, 369 (2012).

[180] V. Karpan *et al.* Graphite and Graphene as Perfect Spin Filters. *Phys. Rev. Lett.* **99**, 176602 (2007).

[181] V. M. Karpan *et al.* Ni (111)/graphene/h-BN junctions as ideal spin injectors. *Phys. Rev. B* **84**, 153406 (2011).

[182] K. F. Mak *et al.* Atomically Thin MoS_2: A New Direct-Gap Semiconductor. *Phys. Rev. Lett.* **105**, 136805 (2010).

[183] J.-Y. J. Lin *et al.* Increase in Current Density for Metal Contacts to N-Germanium by Inserting TiO_2 Interfacial Layer to Reduce Schottky Barrier Height. *Appl. Phys. Lett.* **98**, 092113 (2011).

[184] R. T. Tung. Chemical Bonding and Fermi Level Pinning at Metal-Semiconductor Interfaces. *Phys. Rev. Lett.* **84**, 6078 (2000).

[185] Y. Zhou *et al.* Investigating the Origin of Fermi Level Pinning in Ge Schottky Junctions using Epitaxially Grown Ultrathin MgO Films. *Appl. Phys. Lett.* **96**, 102103 (2010).

[186] R. Jansen *et al.* Electrical Spin Injection into Moderately Doped Silicon Enabled by Tailored Interfaces. *Phys. Rev. B* **82**, 241305 (2010).

[187] W. E. Spicer. New and unified model for Schottky barrier and III-V insulator interface states formation. *J. Vac. Sci. Technol.* **16**, 1422 (1979).

[188] P. Li & I. Appelbaum. Electrons and holes in phosphorene. *Phys. Rev. B* **90**, 115439 (2014).

[189] W. J. Yu *et al.* Vertically stacked multi-heterostructures of layered materials for logic transistors and complementary inverters. *Nat. Mater.* **12**, 246 (2013).

[190] R. Moriya *et al.* Large current modulation in exfoliated-graphene/MoS_2/metal vertical heterostructures. *Appl. Phys. Lett.* **105**, 083119 (2014).

[191] S. Bertolazzi *et al.* Nonvolatile Memory Cells Based on MoS_2/Graphene Heterostructures. *ACS Nano* **7**, 3246 (2013).

[192] Y. Xia *et al.* Observation of a large-gap topological-insulator class with a single Dirac cone on the surface. *Nat. Phys.* **5**, 398 (2009).

[193] H. Zhang *et al.* Topological insulators in Bi_2Se_3, Bi_2Te_3 and Sb_2Te_3 with a single Dirac cone on the surface. *Nat. Phys.* **5**, 438 (2009).

[194] Z.-H. Pan *et al.* Measurement of an Exceptionally Weak Electron-Phonon Coupling on the Surface of the Topological Insulator Bi_2Se_3 Using Angle-Resolved Photoemission Spectroscopy. *Phys. Rev. Lett.* **108**, 187001 (2012).

[195] N. P. Butch *et al.* Strong surface scattering in ultrahigh-mobility Bi_2Se_3 topological insulator crystals. *Phys. Rev. B* **81**, 241301 (2010).

[196] H.-T. He *et al.* Impurity Effect on Weak Antilocalization in the Topological Insulator Bi_2Te_3. *Phys. Rev. Lett.* **106**, 166805 (2011).

[197] B. L. Altshuler *et al.* Effects of electron-electron collisions with small energy transfers on quantum localisation. *J. Phys. C Solid State Phys.* **15**, 7367 (1982).

[198] O. V. Yazyev *et al.* Spin Polarization and Transport of Surface States in the Topological Insulators Bi_2Se_3 and Bi_2Te_3 from First Principles. *Phys. Rev. Lett.* **105**, 266806 (2010).

[199] S. Hong *et al.* Modeling potentiometric measurements in topological insulators including parallel channels. *Phys. Rev. B* **86**, 085131 (2012).

[200] H. Cao *et al.* Quantized Hall Effect and Shubnikov-de Haas Oscillations in Highly Doped Bi_2Te_3: Evidence for Layered Transport of Bulk Carriers. *Phys. Rev. Lett.* **108**, 216803 (2012).

[201] M. Petrushevsky *et al.* Probing the surface states in Bi_2Se_3 using the Shubnikov-de Haas effect. *Phys. Rev. B* **86**, 045131 (2012).

[202] A. A. Taskin *et al.* Manifestation of Topological Protection in Transport Properties of Epitaxial Bi_2Te_3 Thin Films. *Phys. Rev. Lett* **109**, 066803 (2012).

[203] S. R. Park *et al.* Quasiparticle scattering and the protected nature of the topological states in a parent topological insulator Bi_2Se_3. *Phys. Rev. B* **81**, 041405 (2010).

[204] L. Liu *et al.* Spin Hall effect tunneling spectroscopy. *Nat. Phys.* **10**, 561 (2014).

[205] T. Arakane *et al.* Tunable Dirac cone in the topological insulator $Bi_{2-x}Sb_xTe_{3-y}Se_y$. *Nat. Commun.* **3**, 636 (2012).

[206] J. Wu *et al.* Layer thinning and etching of mechanically exfoliated MoS_2 nanosheets by thermal annealing in air. *Small* **9**, 3314 (2013).

[207] M. Donarelli *et al.* Tunable sulfur desorption in exfoliated MoS_2 by means of thermal annealing in ultra-high vacuum. *Chem. Phys. Lett.* **588**, 198 (2013).

[208] J. Moruzzi *et al.* Plasma oxidation of silicon. *Plasma Phys.* **24**, 605 (1982).

[209] K. He *et al.* Crossover of the three-dimensional topological insulator Bi_2Se_3 to the two-dimensional limit. *Nat. Phys.* **6**, 584 (2010).